ABSTRACT

Title of Thesis:	THE METAMORPHIC HISTORY OF A SUBDUCTED SLAB: NEW INSIGHTS FROM THE CATALINA SCHIST
	Alexander Theodore Taylor, Master of Geology, 2023
Thesis directed by:	Professor Sarah Penniston-Dorland Department of Geology

Rocks exhumed from ancient subduction zone interfaces often contain both coherent terranes and block-in-matrix mélanges, but the relationship between these two endmembers and its implications for underplating have not been closely examined. The Catalina Schist is a Cretaceous paleosubduction complex on Santa Catalina Island (California) that contains an amphibolite facies mélange with an underlying unit of coherent amphibolite. In this thesis, I present a metamorphic history of the coherent amphibolite that is based on field and petrographic evidence and pressure-temperature estimates from Raman elastic barometry and trace element thermometry. Rocks from the coherent amphibolite record peak metamorphic conditions of 1.20 to 1.29 GPa and 665 to 691 °C. This is consistent with several amphibolite mélange blocks, but the range of block conditions suggests that some upwards movement of the coherent amphibolite may have occurred at the subduction interface prior to the current juxtaposition of the two units.

THE METAMORPHIC HISTORY OF A SUBDUCTED SLAB: NEW INSIGHTS FROM THE CATALINA SCHIST

by

Alexander Theodore Taylor

Thesis submitted to the Faculty of the Graduate School of the
University of Maryland, College Park, in partial fulfillment
of the requirements for the degree of
Master of Geology
2023

Advisory Committee:
Professor Sarah C. Penniston-Dorland, Chair
Professor Mong-Han Huang
Dr. Philip M. Piccoli

© Copyright by

Alexander Theodore Taylor

2023

Acknowledgements

Innumerable thanks are due to the many people who have supported this project. First and foremost is my advisor, Sarah Penniston-Dorland, who guided me through the work and went above and beyond in supporting my growth as a geologist. Many thanks also go to Phil Piccoli and Mong-Han Huang for serving on my committee and being additional sources of support and scientific expertise. Kayleigh Harvey assisted in the field and provided important ideas about the project. I would also like to thank the other members of my research group for their feedback and encouragement.

The Catalina Island Conservancy was instrumental in organizing the field work. Karen Gaskell of the University of Maryland (UMD) Surface Analysis Center was helpful with the Raman spectroscope. The Raman work was funded by a Geological Society of America (GSA) Graduate Student Research Grant. Conference travel support was provided by a GSA Mineralogy, Geochemistry, Petrology & Volcanology Division travel grant as well as an award from the UMD Earth System Science Interdisciplinary Committee (ESSIC).

Lastly, I would like to thank my friends and loved ones for believing in me and for politely listening while I enthusiastically explain subduction over and over again.

Table of Contents

Acknowledgements ii
List of Tables v
List of Figures vi
Introduction 1
Geologic Background 4
Methods 12
Field Work and Sample Collection 12
Petrography 13
Quartz-in-garnet Barometry 14
Zirconium-in-rutile Thermometry 22
Titanium-in-amphibole Thermometry 26
Scanning Electron Microscope 27
Results 28
Field Observations 28
Coherent Amphibolite (CA) Traverse 33
Rattlesnake Traverse 36
Dawn Valley 38
Cottonwood Canyon 42
Buffalo Springs 44
Sheep Chute 45
Structural Measurements 45
Petrography 46
Mafic Amphibolites 46
Paragneiss 50
Quartzite 51
Schists 52
Textures 52
Quartz-in-garnet Barometry 63
Garnet Chemistry 63
Quartz-in-garnet Calculations 67
Zirconium-in-rutile Thermometry 71
Ti-in-Amphibole Thermometry 75
Discussion 79

A Snapshot of the Downgoing Slab 79
Primary Lithologies 79
Structural History 83
Proto-mélanges 87
A Thermal Gradient Across the Coherent Amphibolite 91
Application of the trace element thermometers 93
Comparison with the mélange 95
Implications for Movement at the Subduction Interface 99
Conclusion 104
Appendix A: QuiG Results 106
A.1: Garnet Chemistry 106
Table A.1. Garnet WDS Major Element Analyses 113
A.2: Raman Peaks 119
Table A.3. QuiG peak shifts and calculated strains, stresses, and inclusion pressures 123
Appendix B: Rutile Geochemistry 128
Appendix C: Amphibole Geochemistry 135
References 147

List of Tables

Table 1. Average residual pressures of quartz inclusions in garnet from the coherent amphibolite and amphibolite mélange, with the number of analyzed inclusions. 68
Table 2. Mean-max Zr concentrations, broken down by location of rutile in sample. 74
Table 3. Ti-in-amphibole compositions and resulting metamorphic temperatures, calculated using the Liao et al. (2021) calibration. 78

List of Figures

Figure 1. Geologic map of Santa Catalina Island 6
Figure 2. Pressure-temperature diagram of the conditions of metamorphism for the units of the Catalina Schist. 10
Figure 3. Schematic stratigraphic column of the Dawn Valley traverse.. 29
Figure 4. Schematic stratigraphic column of the CA traverse.. 30
Figure 5. Correlated stratigraphic columns 31
Figure 6. Map of sample locations and traverse pathways 32
Figure 7. Mafic amphibolite field photographs 35
Figure 8. Paragneiss field photographs 36
Figure 9. Garnet-hornblende block DV20-04 in the Dawn Valley side gully 42
Figure 10. The contact between coherent amphibolite and amphibolite mélange in Cottonwood Canyon. 44
Figure 11. A stereonet plot of poles to foliation 46
Figure 12. Photomicrographs of representative Ca-amphiboles from the mafic amphibolite. 53
Figure 13. Photomicrographs of epidote group minerals in a mafic amphibolite (WB22-6). 54
Figure 14. Photomicrographs of representative plagioclase feldspar in mafic amphibolite 55
Figure 15. Photomicrographs of calcic clinopyroxene in a mafic amphibolite (WB22-3). 56
Figure 16. Photomicrographs of features in the mafic amphibolite WB22-1. 57
Figure 17. Atoll garnets in DV20-04 58
Figure 18. Photomicrographs of rutile exsolution needles in garnet 59
Figure 19. Photomicrographs of paragneiss samples (a-d) and a quartzite sample (e)..... 60
Figure 20. Photomicrographs of a boudin in a shear zone in a mafic amphibolite (WB22-6) 61
Figure 21. SEM back scatter electron (BSE) images of WB22-6 shear zone 62
Figure 22. WDS traverses of paragneiss sample DV22-4B and the quartzite samples CA22-2A-2 and DV22-7 64
Figure 23. CA22-2A-2 isomekes. 65
Figure 24. Core-to-rim traverses of garnets in the mafic samples CA16-01 and DV16-03B. 66
Figure 25. Representative QuiG inclusions 68
Figure 26. Average isomekes (solid red) with ± 2 standard deviations (dashed red lines) 71
Figure 27. Mean Zr concentrations of all grains, by sample.. 73
Figure 28. Grain mean Zr concentrations by sample. 74

Figure 29. Zr concentrations along traverse 75
Figure 30. Calcium amphibole classification diagram 77
Figure 31. Ti content (apfu) of amphiboles. 78
Figure 32. A thermal gradient across the coherent amphibolite.. 93
Figure 33. PT results based on QuiG and ZiR 97
Figure 34. Schematic diagram of the Catalina Schist amphibolite mélange and coherent amphibolite 99
Figure 35. Conceptual model for emplacement of coherent amphibolite..... 103

Introduction

Subduction is a fundamental component of Earth's tectonic system. It is a process known to occur only on Earth (Stevenson, 2003) and it has shaped our planet in myriad ways. At the subduction zone trench, sediments can accrete to the overriding plate and contribute to the growth of continental crust (Clift and Vannucchi, 2004). The sinking of the downgoing plate, or slab, drives mantle convection and contributes to the overall motion of Earth's plates (Stern, 2002). The slab releases fluids as it descends, and these fluids affect the long-term geochemistry of the mantle while also forming economic ore deposits and inducing melting beneath volcanic arcs (Grove et al., 2006; Sillitoe, 2010). Arc volcanoes play an important role in the growth of the continental crust while also posing significant hazards for nearby populations (Stern, 2002; Chaussard and Amelung, 2014). The collision of the two plates generates abundant seismic events, including megathrust earthquakes, the largest earthquakes on Earth and the source of tsunamis (Bilek, 2010). Subduction is therefore a multifaceted process with both geologic-scale impacts and human-scale hazards, yet questions abound about its exact mechanisms, timescales, and controlling factors.

Aside from geophysical studies, which have low resolution and require networks of instrumentation, the best way to study subduction is by looking at exhumed rocks. The subduction interface, or the boundary between the downgoing slab and overriding plate, is a zone of intense deformation, mineral transformations, fluid interactions, and seismic activity (Agard et al., 2018). The position of this zone is variable over time and space, and sometimes suites of rock are detached from the interface and avoid being subducted into the mantle. Eventually, through erosion, these suites of rock are returned to the

surface and studied as paleosubduction zones. They represent “fossilized” pieces of the subduction interface and are today found all over the world (Penniston-Dorland et al., 2015). Paleosubduction zones offer a crucial look at the complex processes that are taking place in subduction zones today but are otherwise unobservable.

Paleosubduction zones build up through a process known as underplating. The subduction interface is a complex region that evolves both thermally and mechanically through time. The interface can at times become mechanically coupled to the overriding plate (Agard et al., 2018). When this occurs, strain is redistributed to new layers and parts of the downgoing slab can become detached from the main interface. When they couple to the overriding plate, they are said to be underplated (Ellis et al., 1999). Successive layers can be underplated over time, creating stacked complexes of distinct tectonometamorphic slices that have downward younging ages. This has been observed at a number of localities worldwide, including in the western Alps (Angiboust et al., 2014), Chile (Angiboust et al., 2018), and northern California (Dumitru et al., 2010). In this way, paleosubduction zones record changes in the subduction interface over time.

There are two dominant modes of rocks exhumed from subduction zones, coherent terranes and mélange zones (Penniston-Dorland and Harvey, 2023). Both occur as distinct, mappable units. Coherent terranes are continuous, kilometer-scale slabs of intact rock. While coherent terranes may have experienced brittle and/or plastic deformation, the original spatial relationships between parcels of rock are maintained. Mélange zones, however, are made of centimeter to hundred meter-scale blocks that have been chaotically mixed in a fine-grained matrix. In a mélange zone, rocks that have been metamorphosed in one facies may be juxtaposed against blocks metamorphosed in

another (e.g., Harvey et al., 2021a). Both coherent rocks and mélange can consist of metasedimentary, metamafic, and meta-ultramafic lithologies (Bebout and Penniston-Dorland, 2016). Coherent terranes and mélange rocks are often found together; example localities include the Rio San Juan Complex (Dominican Republic), the Franciscan Complex (California, USA), and the Shimanto Belt (Japan) (Krebs et al., 2011; Ukar, 2012; Phillips et al., 2020).

Despite commonly being found together, the relationship between coherent terranes and mélange has not been closely examined. The Catalina Schist, a paleosubduction complex in southern California, offers an excellent opportunity to probe this relationship because it contains an amphibolite-grade mélange and a well-exposed, underlying amphibolite facies coherent terrane. The mélange has been well studied (e.g., Sorensen and Barton, 1987; Bebout and Barton, 2002; Penniston-Dorland et al., 2018; Harvey et al., 2021a; Harvey et al., 2021b), but the coherent amphibolite has received less attention. Limited geochronologic evidence suggests that the coherent amphibolite may be older than the mélange (Anczkiewicz et al., 2004; Harvey et al., 2021b). This study seeks to understand whether the coherent amphibolite experienced the same metamorphic history as the mélange.

In order to do so, field and petrographic observations are combined with two relatively new techniques in geothermobarometry. Quartz-in-garnet barometry relies on the Raman peak shifts of quartz inclusions to estimate when those inclusions were entrapped in garnet (Kohn, 2014). It does not depend on calculations from mineral equilibria, as some previous estimates from the Catalina Schist have done (Sorensen and Barton, 1987). Similarly, Zr-in-rutile thermometry uses the temperature dependence of rutile's uptake of

Zr to estimate metamorphic temperatures (Zack et al., 2004; Tomkins et al., 2007; Kohn, 2020). Zr-in-rutile is particularly useful in metamafic lithologies, which often lack the assemblages necessary for other geothermometric tools. The Zr-in-rutile results are supplemented here by another trace element thermometer, Ti-in-amphibole (Ernst and Liu, 1998; Liao et al., 2021). Taken together, these results are used to estimate the peak metamorphic conditions experienced by rocks in the coherent amphibolite.

Unraveling the relationship between the coherent amphibolite and the amphibolite mélange is important for better understanding the nature of the deep (~30-40 km) subduction interface. The distribution of strain at the interface, which controls the movement of materials, also determines seismic activity. Episodic tremor and slip (ETS) is a family of low frequency seismic events and aseismic creep phenomena that are commonly observed in the deep subduction interface of modern subduction zones (Bürgmann, 2018; Peacock, 2009). ETS is thought to potentially trigger larger, up-dip megathrust earthquakes, which cause serious damage, generate tsunamis, and threaten human life (Rogers and Dragert, 2003). The Catalina Schist represents a part of the subduction interface that likely experienced ETS (Kotowski and Behr, 2019), and so the relationships it preserves may provide context for studying slow slip events. Ultimately, incorporating coherent terranes into models of subduction interface processes will allow for more holistic interpretations of modern and paleo- subduction zones.

Geologic Background

The Catalina Schist is an exhumed paleosubduction terrane located on Santa Catalina Island off the coast of southern California (Figure 1; Platt, 1975; 1976). It formed by

subduction of the Farallon plate beneath North America and it locally records mid-Cretaceous ages (Grove et al., 2008). The Catalina Schist consists of a stack of thrust slices metamorphosed from low-grade lawsonite-albite up through high-grade amphibolite facies (Grove and Bebout, 1995). The stack is inverted, meaning that the high-grade amphibolite is structurally highest, and the individual units are separated by low angle thrust faults (Platt, 1976). The protoliths include sedimentary, mafic (oceanic crust) and ultramafic (mantle-derived) rocks. While mafic and sedimentary material occur together in every unit, higher proportions of mafic material occur in the amphibolite and the relative amount of sedimentary material increases moving down sequence (Grove et al., 2008). The differences in protolith reflect long-term (~20 Ma) changes in the subduction system.

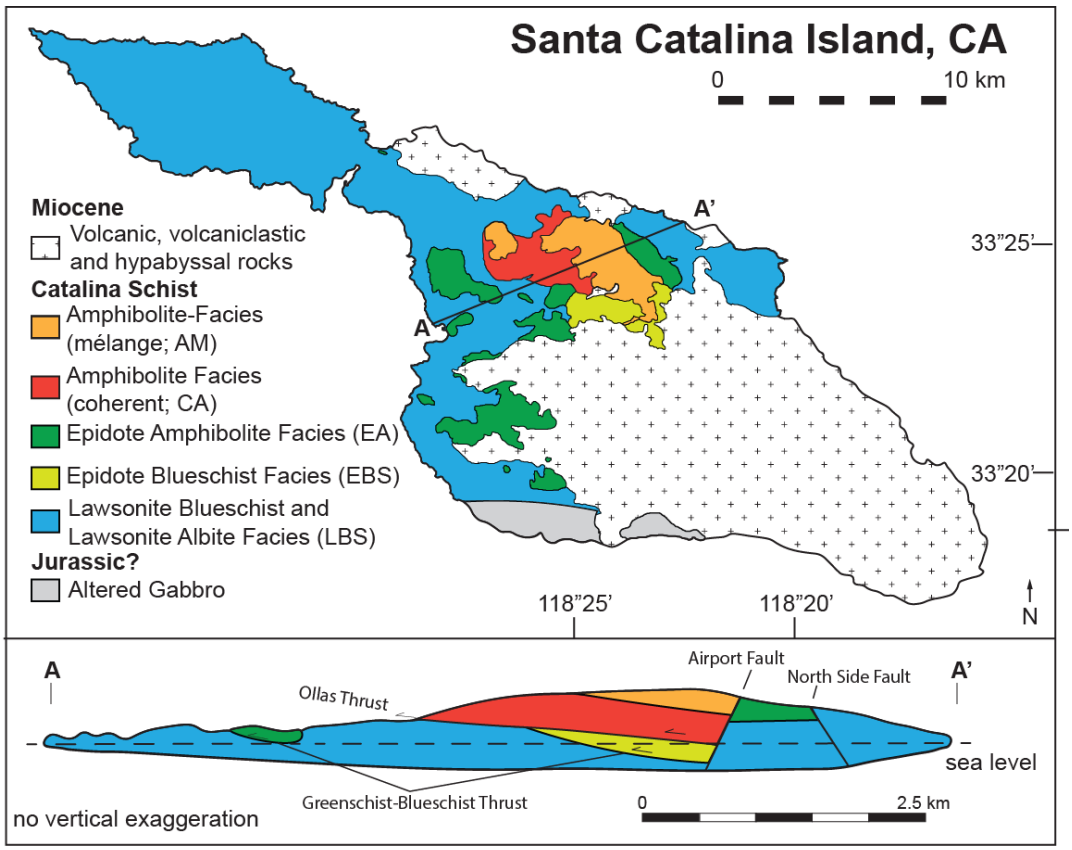


Figure 1. Geologic map of Santa Catalina Island with cross section. Major faults are labelled. Adapted from Platt (1975; 1976).

The Catalina Schist is well known for its mélange, which consists of block-in-matrix structures and formed by progressive tectonic mixing at the plate interface (Sorensen and Grossman, 1989; Bebout and Barton, 2002; Penniston-Dorland et al., 2018; Harvey et al., 2021a). Mélange occurs in all of the metamorphic units and is juxtaposed against (and sometimes intercalated with) large, intact sections of coherent rock. The mélange in the amphibolite facies has been the most extensively studied. Its matrix is fine-grained, schistose, and contains the major phases talc, chlorite, anthophyllite, calcic clinoamphibole, enstatite, and minor quartz. Minor phases include Ni-Fe sulfides, chromite, magnetite, ilmenite, rutile, zircon, apatite, dolomite, and clinopyroxene (Bebout and Barton, 2002). The matrix can be divided into two chemical endmembers: an

aluminous matrix dominated by chlorite, and a siliceous matrix dominated by amphibole or talc. The siliceous matrix is thought to be derived from ultramafic rocks, while the aluminous matrix is of mafic origins. Intermediate matrix compositions have been reached via progressive metasomatic and mechanical mixing at the subduction interface (Bebout and Barton, 2002; Penniston-Dorland et al., 2014). Blocks in the mélange are predominantly mafic and ultramafic, with only rare metasedimentary blocks (Bebout and Barton, 2002). Mafic blocks are typically garnet amphibolite and contain clinoamphibole, garnet, rutile, zircon, and quartz, and variable amounts of chlorite, plagioclase, epidote, phengite, and retrograde titanite rimming rutile (Penniston-Dorland et al., 2018). Ultramafic blocks are serpentinite and contain lizardite, chrysotile, and magnetite (Sorensen, 1988). Some blocks are migmatitic and/or are ringed by reaction rinds and selvages (Sorensen and Grossman, 1989; Penniston-Dorland et al., 2014).

Constraints on the metamorphic conditions of the amphibolite mélange have been revised by several authors. Platt (1976) first estimated that it had been metamorphosed between 500-700 °C and 0.8-1.2 GPa on the basis of the amphibolite mineral assemblages. Sorensen and Barton (1987) combined garnet-clinopyroxene thermometry, the jadeite component of clinopyroxene, constraints from fluid inclusion experiments, and mineral reaction curves to estimate conditions of ~640-750 °C and 0.8 to 1.1 GPa. Grove and Bebout (1995) used phase equilibria to broadly constrain the amphibolite metamorphism to ~600-750 °C and ~0.8 to 1.2 GPa. Zr-in-rutile thermometry was first applied by Penniston-Dorland et al. (2018) to blocks in the amphibolite mélange and resulted in temperatures of 650 to 730 °C at an assumed pressure of 1 GPa and using the calibration of Tomkins et al. (2007). The most recent work by Harvey et al. (2021a) recalculated this

range to be 643-735 °C using the updated Zr-in-rutile calibration of Kohn (2020) and reported pressures of 1.34 to 1.44 GPa based on quartz-in-garnet elastic thermobarometry (Figure 2). This is consistent with a maximum burial of around 40 to 45 km (Grove et al., 2008). The statistically distinct differences in peak conditions recorded by the blocks have been interpreted to mean that they have been transported to their current locations via flow of the weak, fine-grained mélange matrix (Penniston-Dorland et al., 2018; Harvey et al., 2021b).

The history of the coherent amphibolite, on the other hand, is relatively unconstrained. Early work by Platt (1975, 1976) identified that it consists primarily of layered mafic amphibolite, which he calls green hornblende schist. Sitting structurally on top of the mafic amphibolite is a semipelitic schist, which others have referred to as paragneiss, metagraywacke, or simply metasedimentary rocks (Sorensen and Grossman, 1989; Grove et al., 2008; Bebout et al., 1999). In order to distinguish the semipelitic schist from other rocks of sedimentary origin, it will be referred to here as paragneiss. Thin layers of garnet quartzite, which Platt (1976) suggested may have originally been bedded cherts, are scattered throughout the coherent amphibolite but make up a relatively small proportion of the overall unit. An ultramafic body of serpentinite was identified in the Dawn Valley of the coherent amphibolite, but its relationship with the amphibolite mélange is unknown. The serpentinite, along with the surrounding coherent amphibolite, is involved in a kilometer-scale, synmetamorphic anticlinal fold (Platt, 1976). Some localized extension is evidenced by a conjugate pair of opening and shearing faults in the eastern coherent amphibolite, within ~100 m of the top of the coherent body (Grabiec, 2017). At that locality, the fault interfaces are filled with material that resembles mélange matrix

and has elevated concentrations of Ni and Cr compared to the surrounding wall rock. These elements are enriched in ultramafic rocks and also in the mélange matrix, which suggests that mélange matrix was actively deforming at the same time as coherent amphibolite metamorphism (Grabiec, 2017). At its base, the coherent amphibolite is separated from epidote blueschist facies rocks by the Ollas thrust (Platt, 1976). Work by Harvey et al. (2021a) found that the Ollas thrust was likely active during peak metamorphism.

According to Platt (1976), the mafic amphibolite contains hornblende, zoisite, and titanite, and variable amounts of clinopyroxene, clinozoisite, plagioclase, and quartz. Trace amounts of pyrite and magnetite have been observed, garnet is sometimes present, and rutile and/or ilmenite are sometimes present instead of titanite. The paragneiss contains quartz, plagioclase, white mica, biotite, garnet, kyanite, graphite, clinozoisite and/or zoisite, hornblende, and the accessory phases rutile, ilmenite, apatite, and zircon (Bebout et al., 1999). Quartzite layers are mostly quartz and garnet (Platt, 1976). The only estimate of metamorphic conditions for the coherent amphibolite is a Zr-in-rutile temperature of 690 ± 3 °C for a paragneiss sample (Harvey et al., 2021a).

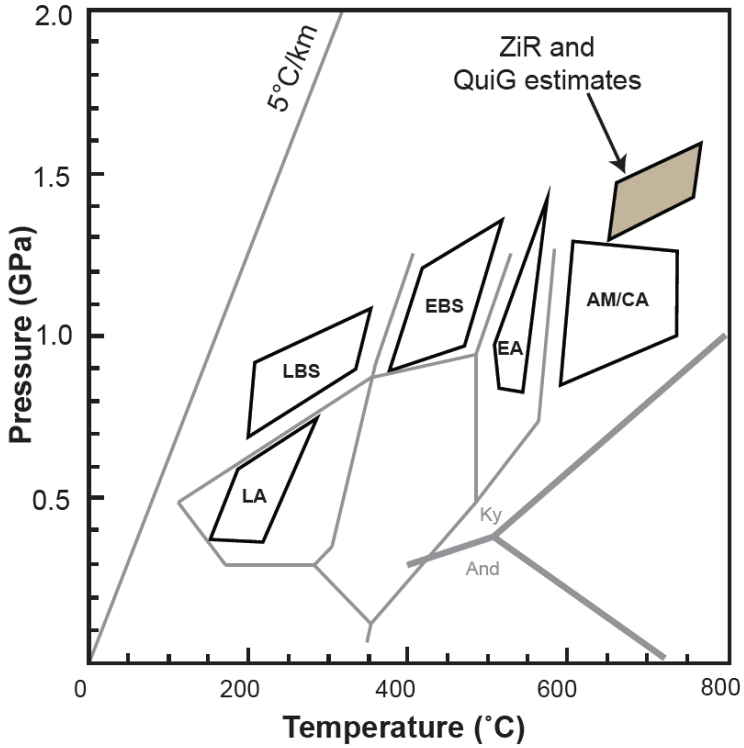


Figure 2. Pressure-temperature diagram of the conditions of metamorphism for the units of the Catalina Schist. White polygons are from Grove and Bebout (1995). Grey polygon represents the latest estimates for blocks in the amphibolite mélange, calculated using quartz-in-garnet barometry (QuiG) and zirconium-in-rutile thermometry (ZiR) (Harvey et al., 2021). Abbreviations are as follows: LA=lawsonite albite, LBS=lawsonite blueschist, EBS=epidote blueschist, EA=epidote amphibolite, AM=amphibolite mélange, and CA=coherent amphibolite.

The Catalina Schist is part of a regional network of Jurassic and Cretaceous-age subducted rocks exposed in a discontinuous belt that includes the Franciscan Complex in northern California and the Pelona-Orocopia-Rand Schists in Arizona and Mexico (Jacobsen et al., 2011). The degree to which the Catalina Schist is genetically related to these other features is debated, but it falls chronologically in the middle of the paleosubduction belt, which ranges from 180 Ma in the north (Mulcahy et al., 2018) to <60 Ma in the southeast (Jacobson et al., 2011). Blocks in the Catalina Schist amphibolite mélange record garnet Sm-Nd ages between 107 ± 5.5 to 115.5 ± 3.0 Ma (Harvey et al., 2021b), while the coherent amphibolite has been dated at 114.5 ± 0.5 Ma using garnet

Lu-Hf (Anczkiewicz et al., 2004) (All age errors are 2σ throughout). This is similar to U-Pb isochron dates for Catalina garnet amphibolite blocks of 111.7 ± 1.5 to 114.1 ± 2.1 Ma (Mattinson, 1986). The maximum depositional age of the amphibolite metasediments is 122 ± 3 Ma based on detrital zircon U-Pb systematics (Grove et al., 2008). The metasediments then cooled slowly (~25 °C/m.y.) until they reached ~350-400 °C, the closure temperature in K-Ar for muscovite, at 105-100 Ma (Grove and Bebout, 1995; Grove et al., 2008). The lower-grade units trend younger downwards, ending with the accretion of the lawsonite-albite at around 95 Ma (Grove et al., 2008). Final exhumation of the Catalina Schist occurred during regional Miocene uplift and extension (Atwater, 1998).

Among paleosubduction terranes, the Catalina Schist is somewhat unusual because it includes rocks metamorphosed at amphibolite facies conditions, which are hotter than the conditions expected in most subduction zones (Gerya et al., 2002; Syracuse et al., 2010; Penniston-Dorland et al., 2015). The Catalina amphibolite represents a geothermal gradient that is approximately 16 °C/km (Harvey et al., 2021a). Amphibolite metamorphism in subduction zones is enigmatic, and the cause may vary between subduction zones. For the Catalina Schist, two main models have been proposed. Platt (1975) suggested that the amphibolite may have been metamorphosed in a nascent subduction zone in which the overlying mantle wedge had not yet been refrigerated. Dating of the Peninsular Range batholiths, however, shows that subduction was well underway by the time of amphibolite metamorphism (Kistler et al., 2003). Grove et al. (2008) hypothesized that the amphibolite represents a forearc thrust adjacent to the magmatic arc that was then juxtaposed by subduction erosion against the underlying

metamorphic units, which display more typical subduction-related geothermal gradients. This model, however, is based on limited detrital zircon data and remains untested. A recent study by Dong et al. (2022) have argued for an eclogite-facies event preceding the amphibolite metamorphism based on pseudosection modeling and the inferred presence of lawsonite pseudomorphs. They calculated peak metamorphic conditions of 2.4-2.7 GPa and temperatures > 580 °C, which would represent a geothermal gradient of ~7 °C/km, significantly cooler than the current interpreted gradient (Harvey at al., 2021a). Future research is needed to confirm this result.

Methods

Field Work and Sample Collection

Most of the samples for this study were collected over a ten-day period in April 2022. The newly collected samples were integrated with a small suite that were previously collected by Dr. Kayleigh Harvey and Dr. Sarah Penniston-Dorland. A sampling plan was prepared in advance with the help of Google Earth satellite imagery and digitized geologic maps created in QGIS. The coherent amphibolite is crosscut by a series of NE-SW oriented dry streambeds which were used as traverse pathways because they often expose bedrock in their banks and because they cut roughly parallel to the vertical thickness of the unit. Samples were collected along five separate traverses through the coherent amphibolite. Each was between ~1 to 1.5 km long and about 4.5 km separate the westernmost traverse from the easternmost. Some additional sampling took place on ridges and hillsides when streambeds were inaccessible.

The collected samples include representative examples from each of the different lithologies observed in the coherent amphibolite. Samples were collected from geographically diverse regions of the coherent amphibolite. Only samples that were relatively unweathered, resistant to breaking with a rock hammer, and of sufficient size for making thin sections were collected. Samples were particularly useful if they contained rutile and/or garnet, because they can be used for the quartz-in-garnet and Zr-in-rutile thermobarometric techniques, but samples without these minerals were collected as well. Aided by a hand lens, estimates of modal mineralogy, grain size, and observations of rock fabric and lithologic layering were made at each major outcrop.

Structural observations were also collected along each traverse. Where possible, the strike and dip of foliation were measured using the digital compass-clinometer app Fieldmove Clino for Apple iOS. This app includes GPS mapping of observations in real time, as well as the ability to take georeferenced photos. Fieldmove Clino has been tested and found to be suitable for almost all applications in field geology (Allmendinger et al., 2017). The accuracy of the app measurements was further confirmed by simultaneously measuring the strike and dip of foliation using a traditional compass. Where possible, the orientations of faults and folds were also measured. Additional general observations included the relative abundance and morphology of veins and fractures. The thickness of individual lithologic layers was estimated using a tape measure. All photos and notes recorded in Fieldmove Clino were then exported and backed up on a computer.

Petrography

Samples were prepared in the UMD rock cutting facility and made into 100 μm “thick” sections (for quartz-in-garnet [QuiG] barometry) and 30 μm thin sections (for everything

else) by Wagner Petrographic. Sample mineralogy and texture were characterized optically using a Nikon LV100POL petrographic microscope at the University of Maryland. The microscope is equipped with QCapturePro software for taking photomicrographs. Thin sections were initially scanned using an Epson Perfection 4490 Photo scanner and then mapped in detail by taking overlapping 1.5x magnification photomicrographs, which are stitched together in Adobe Photoshop to create a composite map of the entire thin section. Samples were mapped in both plane polarized light, which is useful for quartz-in-garnet barometry, and in reflected light, which is useful for zirconium-in-rutile thermometry. Higher magnification images were taken of specific rutile and garnet grains, as needed. To facilitate the indexing of individual mineral grains, these maps and images were annotated using Adobe Illustrator. Minerals not readily identifiable via optical determination were analyzed using electron dispersive spectroscopy on the JEOL 8900R electron probe microanalyzer (EPMA) at the University of Maryland Nanocenter.

Quartz-in-garnet Barometry

Quartz-in-garnet (QuiG) barometry is a relatively new method for determining metamorphic pressures from quartz inclusions in garnet (Enami et al., 2007; Kohn, 2014; Thomas and Spear, 2018). It is one of the most common examples of a broader suite of methods known as elastic geothermobarometry. The principles underpinning this technique are derived from a consideration of mineral elasticity in host-inclusion systems. At the time of their entrapment, quartz inclusions experience the same pressure (due to the lithostatic load as well as any regional pressure gradients) as their garnet hosts. The two minerals, however, have different elastic properties, namely thermal expansivities

and compressibilities. During exhumation from high pressure conditions, as overburden is removed and the effect of regional gradients is reduced, the quartz inclusion expands more than the garnet host and a pressure mismatch occurs (Kohn, 2014). The magnitude of this mismatch, known as residual pressure, depends on the elastic properties of the host and inclusion and the P-T conditions at entrapment. The elastic properties, particularly the shear moduli and the relationship between molar volume and pressure-temperature (P-T) for each mineral (Kohn, 2014), have been determined experimentally. Measuring the residual pressure of a quartz inclusion inside what is an otherwise "relaxed" garnet can thus be used to determine the possible P-T conditions at the time of entrapment.

In order to measure an inclusion's residual pressure, we use what is known as Raman spectroscopy. This non-destructive technique relies on the principles of light scattering. A Raman spectroscope focuses a laser on a sample, either on the surface or at some depth inside, and measures the energy of photons after they have interacted with the specimen. Most of the incident photons are simply scattered and reflected with the same energy as the laser. Some of the back-scattered photons (approximately 0.00001%), however, vibrate with the chemical bonds of the sample and return with a different energy than the laser source (Pasteris and Beyssac, 2020). These are detected by the Raman spectroscope and displayed as a spectrum, with each spectral peak representing an energy shift in the back-scattered photons (Neuville et al., 2014). A Raman spectrum is unique to the molecular arrangement of the substance being measured (Pasteris and Beyssac, 2020).

For many minerals, the exact positions of the peaks in the Raman spectrum are pressure-dependent (Kohn, 2014). The residual pressure of a mineral inclusion can therefore be quantified using its Raman spectrum. While many host-inclusion pairs are possible

thermobarometers, the quartz-in-garnet system is the most well-established (Korsakov et al., 2020). In QuiG barometry, the Raman spectrum of a quartz inclusion in garnet is directly compared to that of an unstrained quartz standard. The magnitude of the shifts in Raman peak positions is a function of the residual strain on the inclusion's crystal lattice (Enami et al., 2007). Shifts in peak position are typically measured as changes in wavenumbers (the inverse of wavelength), $\Delta\omega$ [cm^{-1}], which are then converted to residual pressure (Neuville et al., 2014).

The exact method for converting Raman peak shifts to inclusion pressure (P_{inc}) has been an area of ongoing research. Previously, quartz inclusions were assumed to be under hydrostatic pressures (e.g., Enami et al., 2007; Thomas and Spear, 2018), which could be calculated directly from the position of the dominant (464 cm^{-1}) band in quartz using a calibration curve constructed via hydrostatic diamond anvil cell experiments (Schmidt and Ziemann, 2000). This approach has been utilized in some studies on natural samples (e.g., Wolfe et al., 2021; Schwarzenbach et al., 2021; Dunkel et al., 2020). Recent experimental work, however, has shown that more accurate and precise results are obtained when deviatoric stresses resulting from the anisotropy of quartz are taken into account (Bonazzi et al., 2019; Murri et al., 2018). This approach has already been applied to blocks in amphibolite mélange in the Catalina Schist (Harvey et al., 2021) as well as other high pressure and ultrahigh pressure terranes (e.g., Gilio et al., 2022; Alvaro et al., 2020; Gonzalez et al., 2019).

For this project, garnets were selected for QuiG analysis based on the availability of inclusions and a limited extent of fracturing and alteration. In order to obtain the most

accurate measurement of P_{inc}, inclusions were selected only if they fit the following parameters:

- Shape was near-spherical (Campomenosi et al., 2018; Mazzucchelli et al., 2018).
- Inclusion was located more than 3x the radius of the inclusion away from the surface of the thin section (Bonazzi et al., 2019). For this purpose, 100-μm polished "thick" sections were made for QuiG analysis.
- Inclusion was more than 3x the radius of the inclusion away from the edge of the garnet, fractures, or other inclusions (Mazzucchelli et al., 2018).

Inclusions that do not meet these conditions may show reduced pressure (when proximal to grain boundaries or fractures) or increased pressure (when proximal to other inclusions), compared to the true residual pressure due to entrapment (see references above). Most inclusions analyzed for this project were situated between 15 and 50 μm depth from the surface of the thin section.

Inclusions were analyzed using the Horiba Jobin Yvon LabRAM ARAMIS confocal Raman microscope housed in the University of Maryland Surface Analysis Center. This instrument was calibrated daily using a polished silicon standard. Data were collected using a 532-nm laser, 400 μm hole, 100 μm slit, 1800 gr/mm grating, 30% neutral density filter, a 100x optical objective, and a spot size of 1 μm. Resulting spectra were the average of three accumulations collected over 10 seconds each. Data were collected from multiple garnets in each sample and from as many inclusions as were available. Each inclusion was analyzed at the approximate center and where inclusions were large enough, multiple spectra were collected to confirm homogeneity across the crystal.

Inclusions were analyzed directly following the analysis of a natural "Herkimer diamond" quartz standard at ambient conditions.

Spectra were then fit to the instrument's output points using a mixed Gaussian-Lorentzian function in the MATLAB program ipf.m (O'Haver, 2023). Spectra were taken to be the best of 10 fits using a linear baseline correction. The most prominent spectral peaks for quartz are the 128 cm^{-1}, 206 cm^{-1}, and 464 cm^{-1} modes; the position, height, width, and area were recorded for each of these, as well as the R^2 and percent error (calculated as the standard deviation of the residuals, reported as a percentage of the peak height). Analyses with percent errors larger than 5% were excluded. The standard deviation in peak position for each mode of the quartz standard was calculated on every day of analysis. The largest single-day uncertainty for each peak was taken to be the analytical uncertainty for a given mode. One sigma uncertainties for the 128 cm^{-1}, 206 cm^{-1}, and 464 cm^{-1} modes were 0.27 cm^{-1}, 0.18 cm^{-1}, 0.24 cm^{-1}, respectively. No systematic external drift of the quartz standard was observed for this instrument. In all cases, the analytical uncertainty was larger than the uncertainties in peak fitting. Inclusions with analyses that had non-overlapping peak positions were excluded.

The wavenumber shifts ($\Delta\omega$) for each of the three peaks in a given sample analysis were calculated by subtracting the preceding standard peak position from the sample peak position. Peak wavenumber shifts were converted to residual strains using the program stRAinMAN (Angel et al., 2019). stRAinMAN is a freely available program for Windows that has been experimentally tested for quartz inclusions in garnet (Bonazzi et al., 2019). All three of the peak shifts are needed to calculate the strain state because of the anisotropy of quartz. The peak shifts are known as "phonon-mode" wavenumbers

because they reflect interactions of the incident laser photons with the intermolecular bonds of the crystal lattice, as opposed to the intramolecular bonds (Neuville et al., 2014). stRAinMAN converts wavenumber shifts to strains using a phonon-mode Grüneisen tensor, which is a second-rank symmetric tensor that describes the relationship between three-dimensional strain and the peaks of the Raman spectra (Angel et al., 2019; Murri et al., 2018; Grüneisen, 1926). Because the quartz structure is in the trigonal crystal class, meaning its short axis is the same length in all directions perpendicular to its long axis, only two strains are needed to fully describe the strain state (Angel et al., 2019). The results from stRAinMAN are therefore reported as $\varepsilon_1 + \varepsilon_2$ and ε_3, because ε_1 and ε_2 are identical for quartz. Uncertainties on the strain elements are calculated as a least squares inversion of the Grüneisen tensor operation, and a covariance matrix and χ^2 value are reported as well (Angel et al., 2019).

Once the strains were calculated, they were converted to stress using the freely available, web-based program EntraPT (Mazzuchelli et al., 2021). EntraPT converts residual strain to residual stress using the equation of state (EoS) for quartz (Angel et al., 2017a) and a rescaled elastic modulus tensor (Lakshtanov et al., 2007). The residual pressure of the inclusion is then taken to be the average of the normal stresses (Mazzucchelli et al., 2021):

$$P_{inc} = -\frac{\sigma_1 + \sigma_2 + \sigma_3}{3}$$

EntraPT propagates the uncertainty on P_{inc} by transposing the strain covariance matrix to stress covariance and then converting it to standard deviation (1σ) (Mazzucchelli et al.,

2021). Entrapt also uses the latest EoS for pyrope, almandine, and grossular (Angel et al., 2022).

Once this process has been repeated for all of the quartz inclusions in a given sample, a representative P_{inc} needs to be determined. There is no agreed-upon method for doing this. Some researchers simply take the highest recorded P_{inc} in a sample (e.g., Wolfe et al., 2021; Szczepański, et al., 2022), while others group inclusions by location within garnet zones (i.e., core, mantle, or rim) and then take a mean P_{inc} for each stage of garnet growth (e.g., Cisneros et al., 2022; Gilio et al., 2022). While the purpose of this work is to determine peak metamorphic pressures, using only the highest recorded P_{inc} to calculate entrapment pressure is not necessarily appropriate because it runs the risk of influence from localized overpressures. In such a scenario, unseen inclusions or structural heterogeneities within the garnet could inflate the inclusion's residual stress beyond that which is due to entrapment. Similarly, an all-inclusive average, whether for the sample as a whole or broken down by garnet zone, can include inclusions that, due to cracks undetected during sampling, no longer retain their original host-inclusion stress relationship. In this case, the P_{inc} could be lower than expected and skew the mean for that sample. For this reason, the highest statistically robust sub-population of P_{inc} values was determined for each sample using Peakfit Explorer, a graphical user interface (GUI) developed by Dr. Buchanan Kerswell (https://github.com/buchanankerswell/pkft) and based on the IsoplotR package (Vermeesch, 2018). Peakfit Explorer takes data and their associated standard deviations and identifies overlapping sub-populations using a Gaussian mixture model. It produces equivalent results to the Unmix routine within the original Isoplot extension for Microsoft Excel (Ludwig, 2012), which used the Sambridge

and Compston (1994) approach to deconvolution. Aside from being more user-friendly, Peakfit Explorer was selected over Isoplot Unmix because it does not require the *a priori* input of the number of sub-populations. Peakfit Explorer identifies whether sub-populations exist and then groups the P_{inc} values accordingly. All of the P_{inc} values that fell within the highest sub-population were taken to be the representative residual pressures for that sample. A weighted mean of these representative P_{inc} values was then determined using the weighted mean function of IsoplotR, version 5.1 (Vermeesch, 2018). IsoplotR reports the 2σ standard deviation of the weighted mean P_{inc}, based on the uncertainties copied over from EntraPT.

The P_{inc} of a given inclusion represents the residual stress that the crystal is experiencing at ambient conditions. The magnitude of that stress is the result of the interplay between the mechanical properties of the quartz and the properties of its garnet host, both of which are described by mathematical expressions called equations of state (EoS). With a P_{inc} as a starting point and the equations of state as a guide, it is therefore possible to model all of the conditions in the crust at which that garnet could have trapped that particular quartz inclusion. Such a model is called an isomeke and is represented by a line in P-T space (Angel et al., 2014). An isomeke that represents a sample as a whole, and not just an individual inclusion, can be calculated using the "best-fit" weighted mean P_{inc}.

All isomeke calculations were performed using the freely available platform EosFit-Pinc, version 2.2 (Angel et al., 2017b). EosFit-Pinc has been verified experimentally for quartz in garnet by Thomas and Spear (2018). At the time of writing, EosFit-Pinc was equipped with the EoS for quartz (Angel et al., 2017a) and the EoS for almandine, grossular, and pyrope (Angel et al., 2022). To take into account the differences between these end-

members, a generic garnet composition was calculated for each lithology using wavelength-dispersive X-ray spectroscopic (WDS) analyses collected on the EPMA at the University of Maryland Nanocenter. Measurements of garnet major element chemistry were made using a 15 kV accelerating current, 25 nA beam current, and a 1 μm spot size. Spots were placed in the cores, rims, and mantles (where possible) of two to four garnets from each of the mafic, paragneiss, and quartzite lithologies. All Fe was assumed to be in its +2 valence state (meaning zero andradite is present). The mole fraction of the almandine, pyrope, and grossular endmembers for every analysis was renormalized and then averaged for each lithology as a whole. To aid in the interpretation of garnet growth histories, four garnets (from two mafic amphibolites) were selected for major element X-ray maps. Maps of Al, Ca, Fe, Mg, and Mn were made using the same 5 WDS detectors on the EPMA at UMD. X-ray maps were processed using the software ImageJ. The average garnet composition for a given lithology was used to weight the results of the EosFit-Pinc end-member isomeke calculations for the "best-fit" P_{inc}. Isomekes for individual inclusion P_{inc} values were also calculated using the average garnet compositions. Ultimately, variation in the garnet composition has been shown to not significantly change the isomekes (Kohn, 2014).

Existing QuiG data for blocks in the amphibolite mélange (Harvey et al., 2021a) were reprocessed using the method described above, starting with the wavenumber shifts of the Raman peaks.

Zirconium-in-rutile Thermometry

Zirconium-in-rutile (ZiR) thermometry is a simple and precise method for determining peak metamorphic temperatures in rocks containing rutile, zircon, and quartz (Tomkins et

al., 2007), all of which were observed in these samples. The method is particularly useful because rutile occurs in a wide variety of settings, many of which lack other useful geothermometers (Zack and Kooijman, 2017). Early development of the Zr-in-rutile thermometer included samples from Catalina Schist amphibolite mélange blocks in its calibration (Zack et al., 2004). The method has been further applied to the amphibolite mélange by Penniston-Dorland et al. (2018) and Harvey et al. (2021a).

Zr-in-rutile thermometry is based on the equilibrium relationship between zircon, quartz, and the zirconium component of rutile:

$$ZrO_2 \text{ (in rutile)} + SiO_2 \text{ (quartz)} = ZrSiO_4 \text{ (zircon)}$$

This relationship is highly temperature-dependent, and it allows for the determination of metamorphic temperatures using the zirconium concentration in rutile (Zack and Kooijman, 2017). Ideal samples will contain all three phases, but the thermometer can still be used on samples that lack quartz if the activity of quartz (*a*SiO2) is calculated (Ferry and Watson, 2007).

The zirconium concentration of rutile was measured on the EPMA at the University of Maryland Nanocenter using a 20 kV accelerating voltage, a 120 nA beam current, and 1 micron beam diameter. Zirconium concentrations were measured on three different spectrometers simultaneously; two counted the peak for 300 seconds, and one counted the peak for 240 seconds. Time spent on backgrounds was 150 and 120 seconds, respectively (half of time spent on peaks). A ZAF correction scheme was used to process the data (Armstrong, 1988), and a natural rutile standard (K13-02) was used to assess their quality. The full suite of measured oxides included TiO_2, ZrO_2, Al_2O_3, FeO, Nb_2O_5,

SiO_2, MnO, and Ta_2O_5. Between 10 and 27 grains were analyzed in each sample. Measurements were taken from the center of each grain in order to avoid any possible diffusional resetting and to record the highest Zr concentration. For all grains that are large enough relative to the beam size, two measurements were taken from the approximate grain center. Populations were divided into matrix rutile and rutile inclusions in garnet in order to more closely link the temperature estimates with the results from quartz-in-garnet barometry. The growth history of rutile was assessed by measuring a core-to-rim traverse in a matrix rutile grain in the paragneiss sample DV16-04B. Target grains are euhedral to subhedral in shape, lacking inclusions or exsolution textures, showing limited grain boundary dissolution, and are not adjacent to zircons. To further avoid the effects of micro-inclusions of quartz and zircon, analyses with Si greater than 300 ppm were excluded (Zack et al., 2004).

The Zr concentration can vary significantly between rutile grains in a single sample, possibly indicating variable growth histories, but grains with the highest Zr concentrations are likely to record the peak metamorphic temperature experienced by the sample (Zack and Kooijman, 2017). There is no consensus on the most statistically accurate way to determine the highest Zr concentration for a sample, but for this project the mean maximum zirconium method was used because it has previously been applied to the Catalina Schist for blocks in amphibolite mélange (Penniston-Dorland et al., 2018; see also Harvey et al., 2021a). Using this method, the highest statistically indistinguishable Zr concentrations are averaged to find a “mean-max” Zr-in-rutile concentration for the sample. In this case, concentrations are considered indistinguishable if they fall within two standard deviations (2σ) of each other (based on the analytical

uncertainty of the EPMA counting statistics). The mean-max method produces comparable results to using the upper quartile of Zr concentrations and is less likely to be affected by the presence of distinct sub-populations in the dataset (possibly arising from retrogression; Harvey et al., 2021a).

For this project, the mean-max method was first applied to individual grains where multiple analyses were collected. If the Zr concentrations overlapped within measurement uncertainty, they were averaged together and their individual uncertainties were propagated. On the other hand, if one analysis had higher Zr than the other and their 2σ uncertainties did not overlap, then only the highest analysis was retained. The mean-max method was then applied to the population of rutile grains in the sample as a whole, similarly comparing their 2σ uncertainty ranges and averaging the highest non-overlapping sub-populations. The uncertainties of the individual grain mean-max Zr concentrations were propagated for the sample mean-max. In order to assess whether there are differences between matrix rutile and rutile included in garnet, the mean-max Zr process was repeated for each of those subsets.

Once the mean-max Zr concentrations were determined, metamorphic temperatures were calculated using the combined experimental-empirical thermometer calibration of Kohn (2020). This is the most up-to-date calibration of the thermometer in the α-quartz stability field, and it can be expressed as:

$$T\ (°C) = \frac{71360 + 0.378 \cdot P(bars) - 0.130 \cdot C(ppm)}{130.66 - R \cdot ln\ [C(ppm)]} - 273.1$$

where C is the Zr concentration and R is the gas constant. Isopleths in P-T space were generated by varying the pressure from zero to 24,000 bars (2.4 GPa).

Uncertainty in ZiR results can arise from several sources. As stated earlier, natural geologic variability creates a spread in Zr concentrations usually ranging by <400 ppm for a given sample. Analytical uncertainty on the EPMA counting statistics is typically <15%, and more often <10%. These uncertainties are propagated through the mean-max Zr determination and the thermometer calculation. Uncertainty on the thermometer calibration itself is ±10-15 °C (2σ; Kohn, 2020).

Titanium-in-amphibole Thermometry

The concentration of Ti in Ca-amphibole has long been recognized to correlate positively with increasing temperature (Raase, 1974; Gilbert et al., 1982; Ernst and Liu, 1998; Schumacher, 2007). For this project, the Ti concentration of amphibole rims and cores was measured on the EPMA at UMD using a 15 nA current, 15 kV accelerating voltage, 5 μm beam size, and 30-s counting time for Ti. Fifteen to seventeen grains were measured in 4 samples from across a single traverse of the coherent amphibolite. Each grain was measured once in its core and once at its rim. Amphibole formulae were determined using the AMFORM model described in Ridolfi et al. (2018), normalized to 22 O. Grain rims and cores were treated as separate populations. A “mean-max Ti” concentration was determined for each sample following an identical procedure as the mean-max Zr method described above. When samples contained an outlier with anomalously high Ti, the outlier was ignored and the second-highest Ti value was designated as the maximum. This approach ensured that at least 8 grains were included in each sample’s mean-max calculation.

The temperatures of amphibole formation were then calculated using the calibration of Liao et al. (2021):

$$T(°C) = \frac{2400}{1.52 - \log Ti^{Amp}} - 273$$

where Ti^{Amp} is the Ti concentration of amphibole in atoms per formula unit (apfu). The 1σ uncertainty for the calibration is ±35 °C, with a recommended range of 0.1-0.5 apfu. The calibration uncertainty is larger than analytical uncertainty and so is applied to the samples here.

The conditions required for use of the Liao et al. (2021) Ca-amphibole thermometer are that Ti-phases be present and that the oxygen fugacity (fO_2) is less than 2 log units above the Ni-NiO buffer (NNO). Ti-phases such as titanite, ilmenite, and rutile are abundant throughout the coherent amphibolite and their presence was confirmed using the EDS detector on the electron microprobe. Additionally, the presence of sulfides such as pyrite (identified via EDS on the EPMA) and the absence of sulfates suggests that the fO_2 of this system was less than the sulfide-sulfur oxide buffer (SSO), which is roughly equivalent to NNO+2 (Zhou et al., 2022; see also Mungall, 2002). The third requirement is that the system be sub-alkaline, which does not apply to amphibolite. This thermometer has been applied to amphibolites in subduction zones (Dong and Wei, 2021) and other high-grade settings (e.g., Zhou et al., 2022; Corvò et al., 2022).

Scanning Electron Microscope

High-magnification identification of mineral phases in the mafic sample WB22-6 was conducted on a Hitachi SU 5000 field-emission variable pressure scanning electron microscope (FE-SEM) equipped with an energy dispersive spectrometer (EDS) at the U.S. Geological Survey Reston Electron Microbeam Laboratory. The sample was carbon

coated and analyzed using a 20 kV accelerating voltage, a 50 nA spot intensity, and a working distance of 10 mm.

Results

Field Observations

Samples were collected along three main traverses through the coherent amphibolite, with some additional observations made at smaller isolated localities (Figure 6). What follows is a narrative description of the observations made in the field, broken down by location. Schematic stratigraphic columns were constructed using the observations described herein (Figure 3, Figure 4, and Figure 5). They primarily demonstrate lithologic relationships encountered in the field and do not take into account compression due to folding. Approximate unit thicknesses were calculated using an average dip angle of 50°.

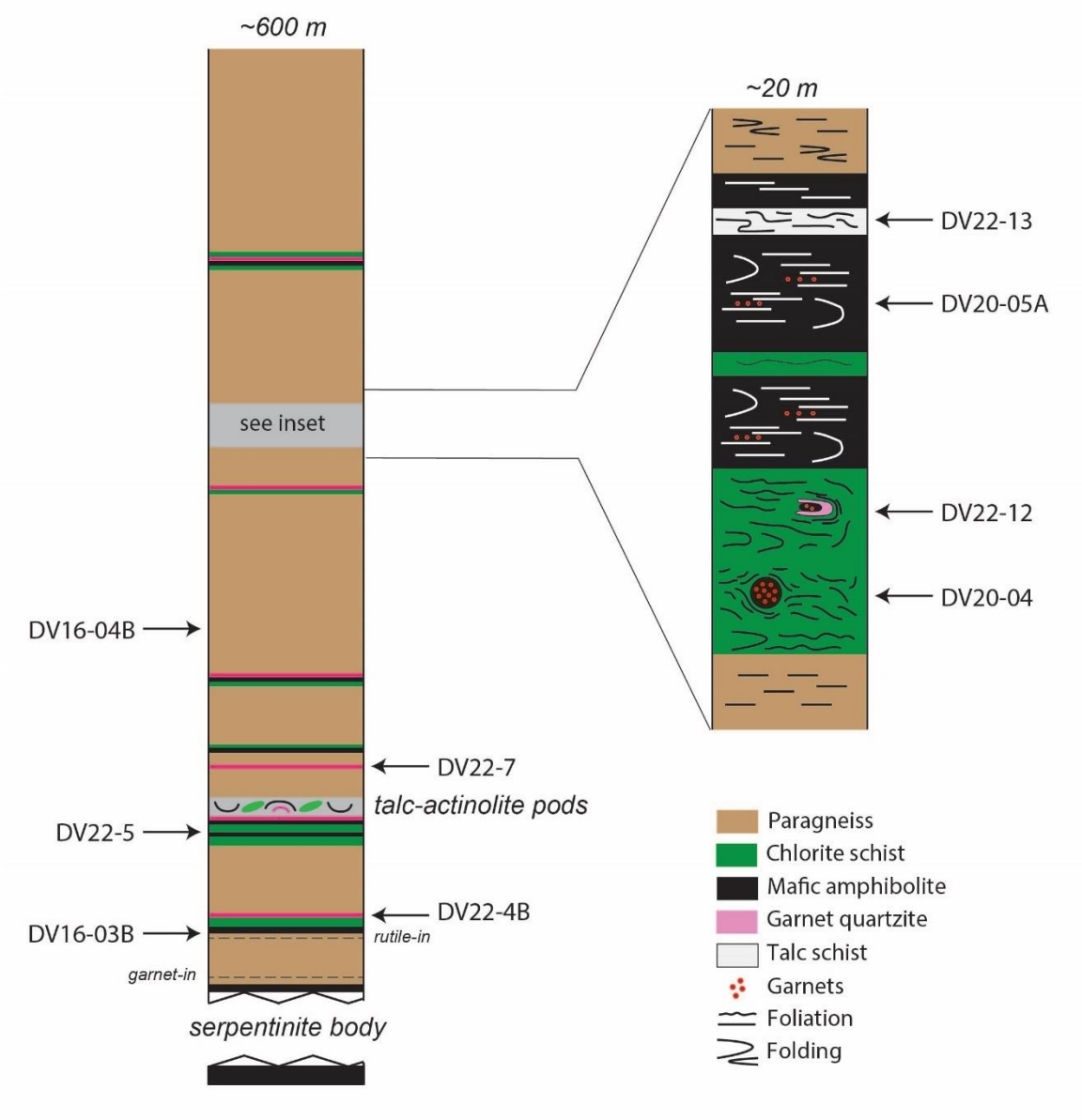


Figure 3. Schematic stratigraphic column of the Dawn Valley traverse. Layers are meant to show approximate location and lithologic contacts, not absolute thickness. Sample positions are marked. The first occurrences of garnet and rutile and marked by dashed lines. Total thickness is about 600 m.

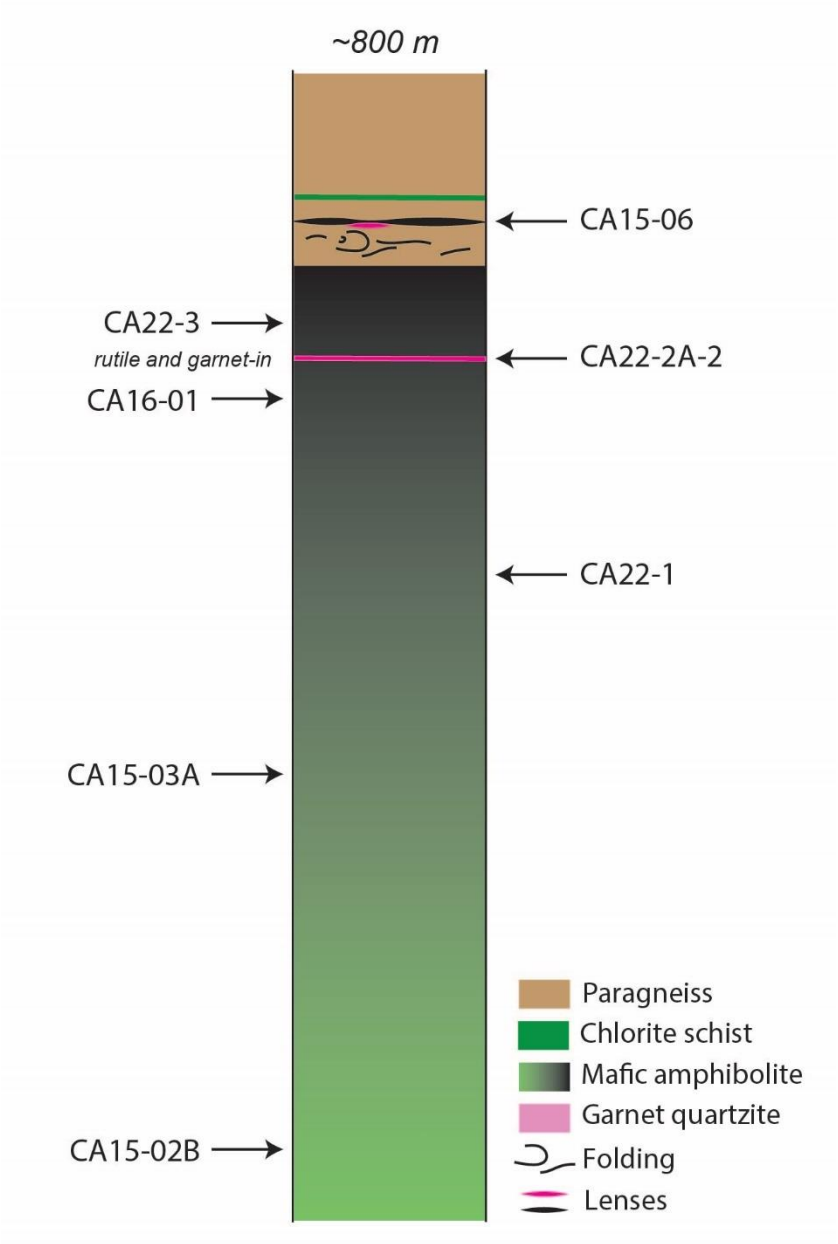


Figure 4. Schematic stratigraphic column of the CA traverse. Layers are meant to show approximate location and lithologic contacts, not absolute thickness. Sample positions are marked. The first occurrence of garnet and rutile coincides with the quartzite where CA22-2A-2 was sampled. Total thickness is about 800 m.

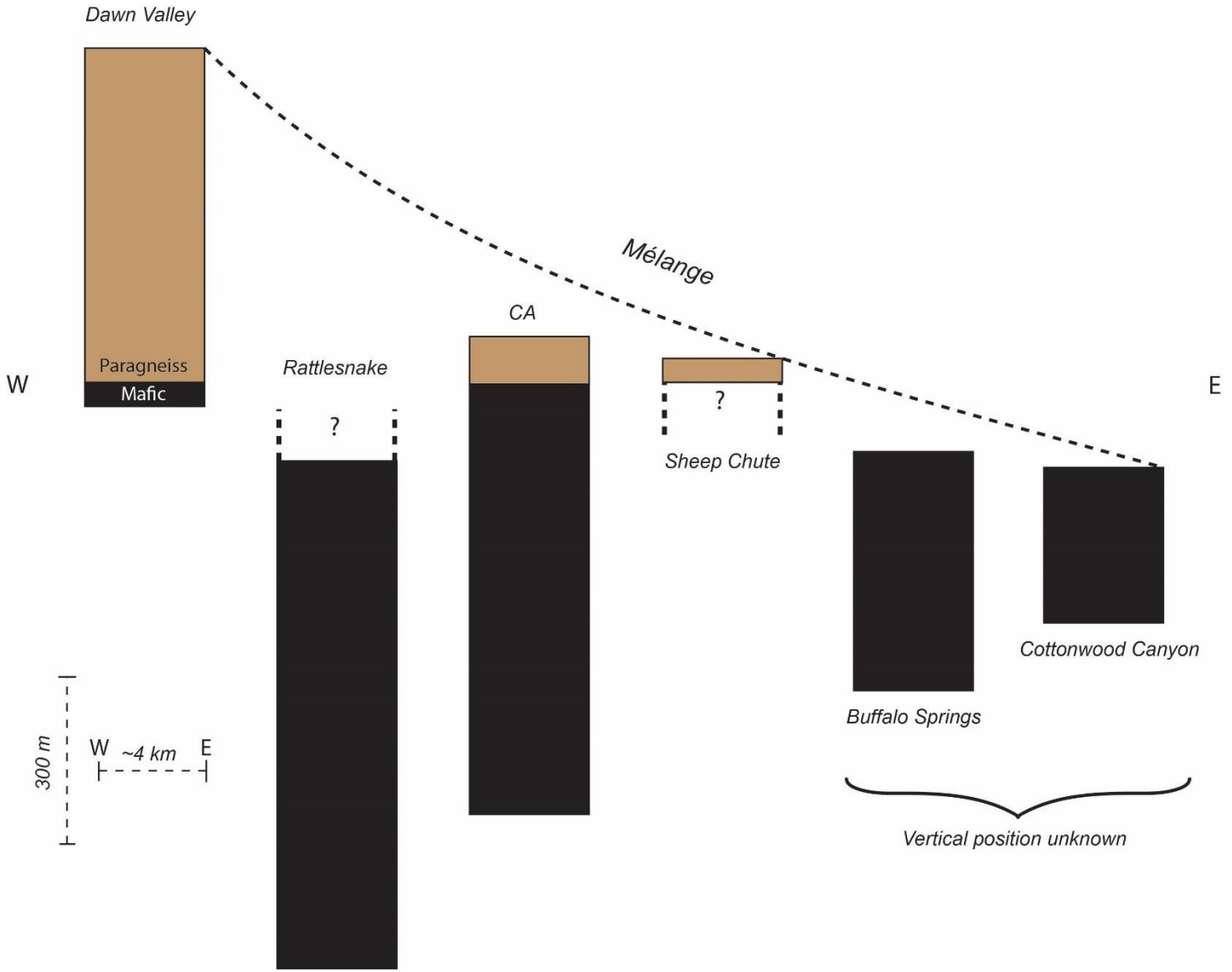


Figure 5. Correlated stratigraphic columns moving from approximately west to east along strike of the coherent amphibolite. Columns are simplified to show only the distribution of mafic amphibolite and paragneiss. The inferred boundary with the amphibolite mélange is shown as a dashed line. Columns were correlated using the contact between coherent mafic amphibolite and paragneiss. Note that the horizontal and vertical scales are different.

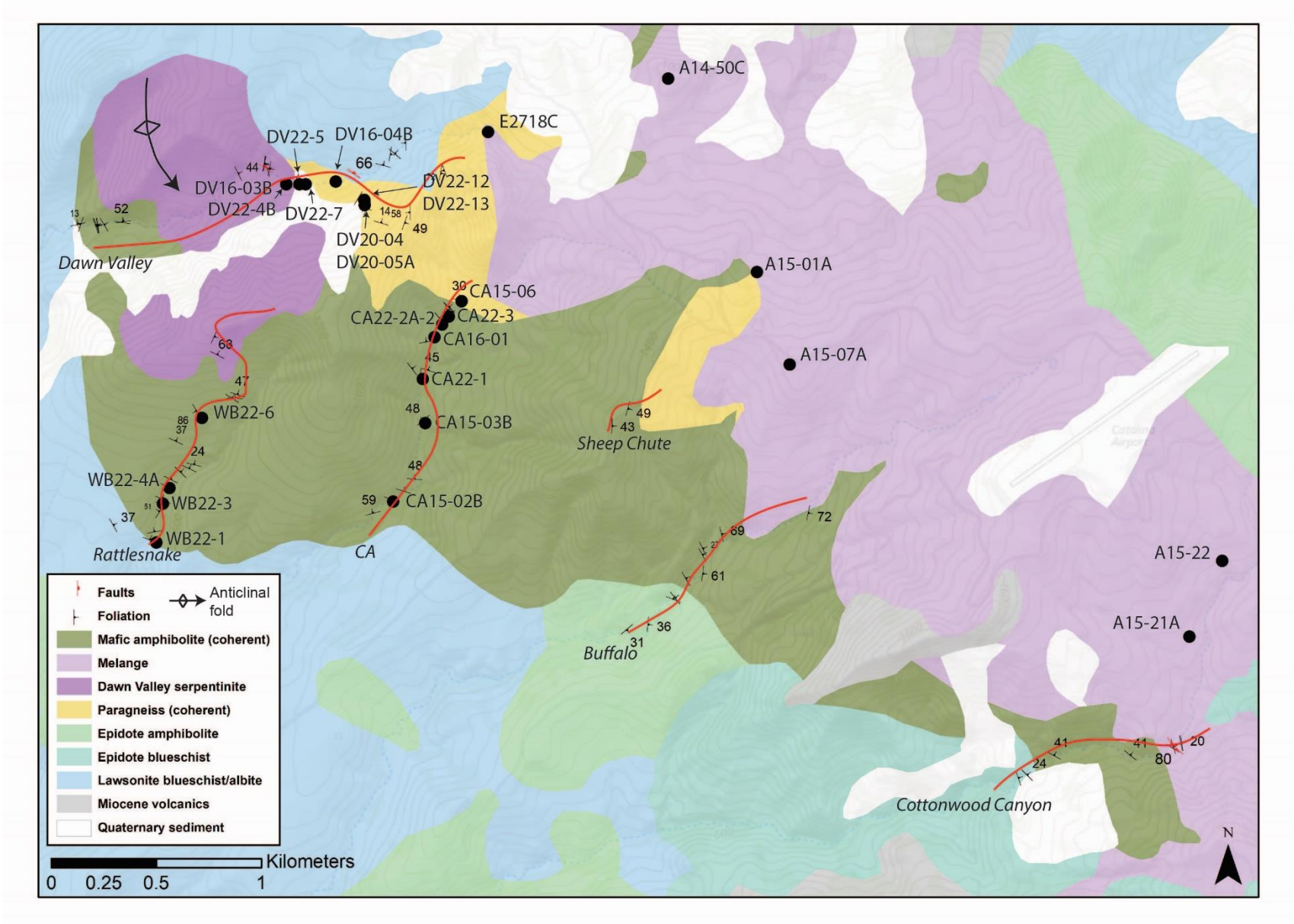


Figure 6. Map of sample locations and traverse pathways (red lines). After Platt (1976) with modifications by Grove and Bebout (1995). Base map is the USGS national topographic map (https://www.usgs.gov/programs/national-geospatial-program/national-map).

Coherent Amphibolite (CA) Traverse

Taking its label from a pre-existing naming convention, the CA traverse is not the only path through the coherent amphibolite, but it does offer one of the most complete snapshots of the subducted slab in terms of lithology. Starting from its contact with the lawsonite blueschist at its more southerly end, the CA traverse follows a streambed uphill through the mafic coherent amphibolite. In this way, the traverse moves stratigraphically up through coherent amphibolite nappe. Outcrops are regularly exposed in the stream's bank and along its sides.

The first coherent amphibolite encountered at the base of the CA traverse is mafic, foliated, and consisting primarily of hornblende and plagioclase, with some epidote (estimated in the field, see Petrography results for more precise mineralogical descriptions). There are millimeter to centimeter-scale quartz veins and some folding present. Much of the mafic amphibolite follows this same basic description and varies only in the proportion of the different minerals and in the degree of veining and folding (Figure 7).

Moving up through the CA traverse, the rocks gradually become more mafic with increasing amounts of amphibole. Felsic minerals are at times concentrated in patches and layers, and sometimes are dispersed throughout a rock. The amount of epidote varies, with some rocks including very little and some including up to about 30%. Similarly, the color of the rocks varies from black to green. At CA22-1, about the halfway point of the mafic amphibolite, titanite became visible in hand sample.

The mafic amphibolite begins to change towards the top of the section. Approximately 0.5 to 1-m thick quartzite layers are present with mafic layers on either side. Garnets were first observed in these quartzites, and then in the mafic layers themselves. Rutile is now the Ti-bearing phase, instead of titanite, although it is not visibly present in every layer. Local folding and felsic veining become more prevalent as well. Sample CA22-2A-2 is a garnet quartzite exposed in between mafic layers, and CA22-3 is a garnet and rutile-bearing layered mafic amphibolite.

Continuing up the CA traverse, the mafic amphibolite soon gives way to metasedimentary paragneiss. The paragneiss is a poorly consolidated, brown-yellow rock that consists primarily of plagioclase feldspar, quartz, and mica. Garnet and rutile were not observed in hand sample in the CA traverse paragneiss. At one outcrop, paragneiss was interlayered with mafic garnet amphibolite and garnet-bearing chert in complex, meter-scale folds that seemed to be concentrated in a discrete layer, distinct from the less resistant, underlying planar paragneiss (Figure 8a). This is the same location from which the chert pod CA15-06 was previously collected (Harvey et al., 2021a). Moving up the streambed from this outcrop, ~6 to 10 m thick layers of paragneiss alternate with ~3 m thick layers of chlorite schist. The chlorite schist is a weakly consolidated, foliated, green metasomatic rock that in hand sample consists almost entirely of chlorite. Continuing up section, the paragneiss continues in this manner, with interlayers of chlorite schist, until the talc schist matrix of the amphibolite mélange is encountered.

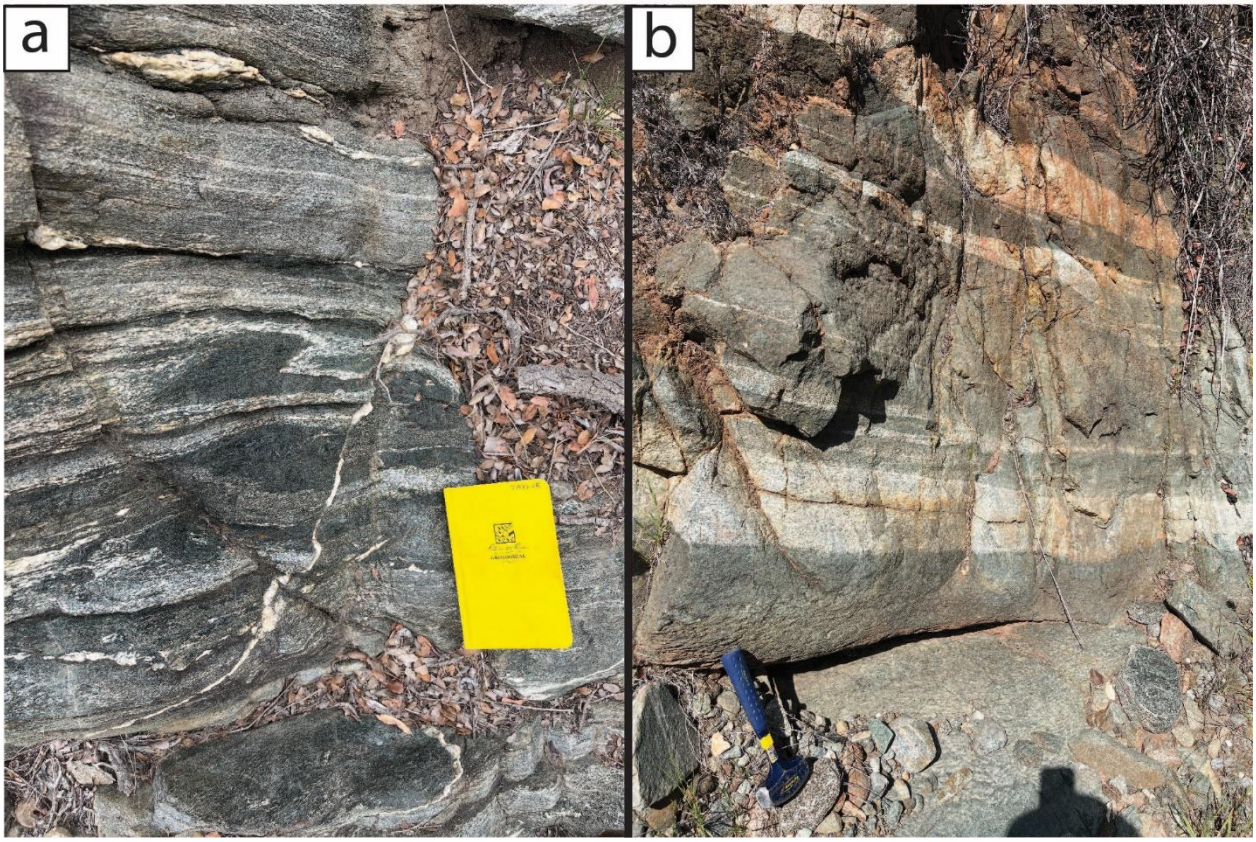


Figure 7. ***a****. Folded, dark green mafic amphibolite with felsic layers and cross-cutting veins at base of CA traverse.* ***b****. Green-black mafic amphibolite with undeformed felsic banding in Rattlesnake traverse. Note hammer for scale.*

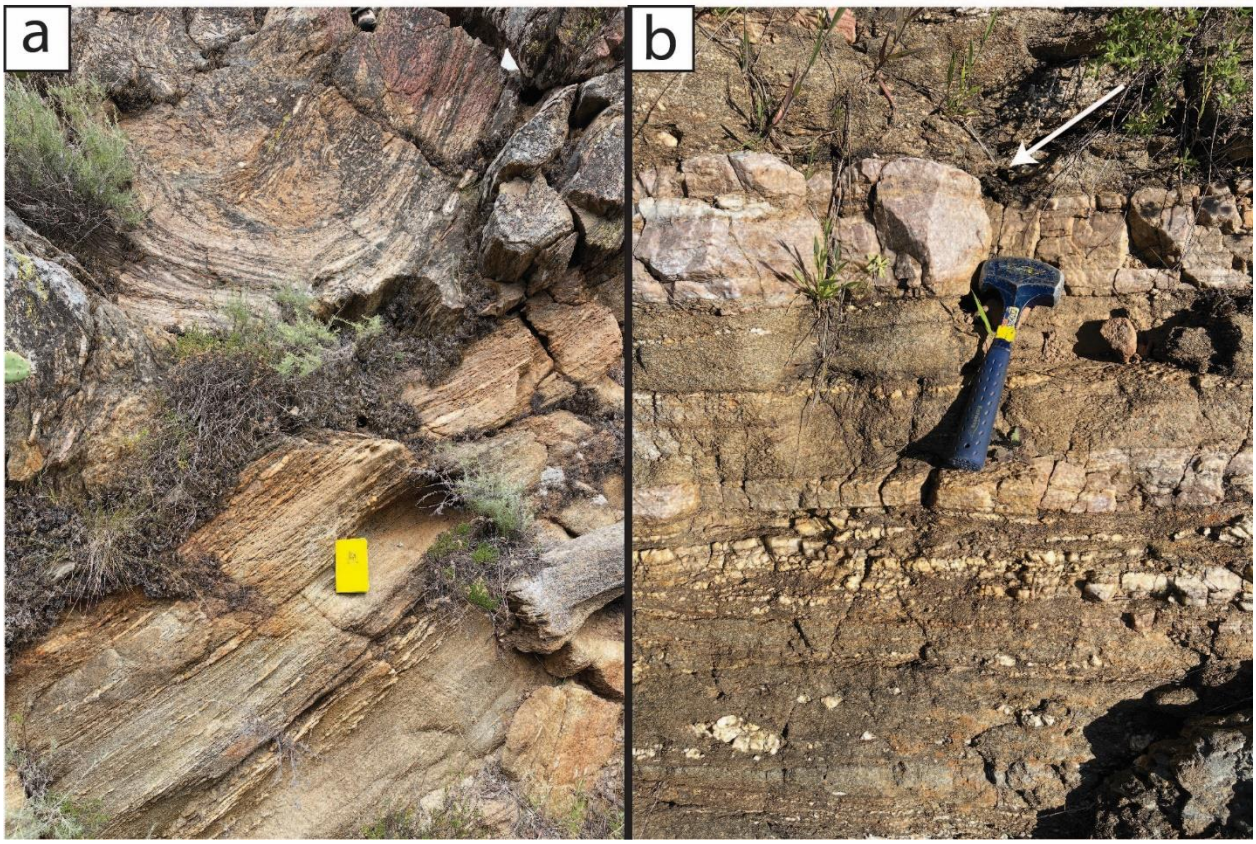


Figure 8. ***a****. Paragneiss in upper CA traverse. Lower layers are planar and less resistant, while upper layers are folded and contain interlayers of black mafic material.* ***b****. Paragneiss in the upper Dawn Valley side gully. Arrow points to a layer of garnet quartzite.*

Rattlesnake Traverse

Also known as West Buffalo (samples from here are labelled “WB”), this traverse is approached via a dirt road leading up from Little Harbor. The approach passes outcrops of blueschist and exotic migmatitic garnet amphibolite mélange blocks (see Harvey et al., 2021a). The first coherent amphibolite encountered is an unusual grayschist rock found in the side of the stream bed. This dark, dull rock was not found elsewhere in the coherent amphibolite, but its foliation and orientation suggests that it is a coherent rock. Forty yards upstream is a similarly oriented, green mafic amphibolite, which is more consistent with the rest of the traverse.

The mafic amphibolites of the Rattlesnake Traverse are, on average, greener and more epidote-rich than the CA traverse. The outcrops often form resistant ledges that cut across the streambed and are relatively unweathered. Compositional banding was observed in WB22-3, with layers of green amphibole and well-formed epidote crystals (up to 2 inches long) juxtaposed against felsic layers. The bands appeared to have been ductilely deformed. Twenty yards upstream was a completely different outcrop, with fine banding, smaller epidotes, linear quartz veins, and no evidence for ductile deformation. This pattern of localized variations in epidote morphology, veining, and deformational style continued through the lower part of this traverse.

About halfway, the amphiboles became darker, signaling a change in composition, and epidote less prevalent. Shortly after these changes were observed, a rattlesnake (hence the name of the traverse) forced a diversion of the route. Moving up the steep slope of the hillside, several small exposures of heavily weathered amphibolite with some felsic banding were encountered. WB22-6 was collected from a finely layered rock in the hillside.

The rocks appeared to become more uniform as the top of the ridge was approached. Amphibole grains in this area are typically 2 to 3 mm in length and the rocks were approximately evenly distributed between dark amphiboles and the light felsic minerals. On top of the ridgeline, outcrops are heavily weathered and it was difficult to collect clean samples. They were typically felsic amphibolite, although one exposure was of a rock that consisted entirely of coarse-grained (~1 to 2 inch long) dark, interlocking amphibole crystals.

Dawn Valley

Approaching from the west (and from lower down, stratigraphically), the Dawn Valley traverse begins with several outcrops of mafic coherent amphibolite. Quartz veins up to 3 cm thick are abundant, sometimes contain epidote, and are arranged in complex isoclinal folds. Moving up stream, the rocks display variation in terms of foliation and the proportion of chlorite present. A body of ultramafic material is soon encountered. The rocks of this weak, schistose body are chaotically oriented and contain veins of fibrous, green serpentine minerals. At the contact between the two units, foliated and tightly folded coherent amphibolite directly underlies layer of coarse, unfoliated hornblende which soon gives way to weak, vertically-oriented ultramafic material. The nature of this ultramafic body and its relationship to the amphibolite mélange is enigmatic. Much of the body as mapped is covered by alluvial sediments. The orientations of the surrounding mafic coherent amphibolite suggest that folds are present. Towards the eastern end of the ultramafic body, a measured lineation and foliation within the serpentinite broadly line up with the surrounding coherent amphibolite. Quartz veins, pods of mafic amphibolite, and patches of possibly metasedimentary material were also observed within the ultramafic body.

The mafic amphibolite that contacts the eastern end of the ultramafic body contains garnets, which were absent at the western end. The mafic material quickly gives way to metasedimentary paragneiss. Bedding within the paragneiss may be originally lithologic. Layers vary in their degree of consolidation, with loose and solid paragneiss layers separated by thin contacts. Three small faults were observed in a layer of poorly consolidated paragneiss. Two approximately parallel fault surfaces, striking N14W and

dipping 50° W, separated by ~25 cm, are crosscut by a near vertical fault surface striking N-S. The fault surfaces consisted of a black, glassy material and were about 2 cm thick. They are further evidenced as faults by offsets in the numerous ~1 cm thick quartz veins that were present in the outcrop.

Approximately 40 m upstream is ~3 m thick layer of mafic amphibolite containing garnet, hornblende, needles of epidote, plagioclase, and folded quartz veins. This is where DV16-03B was collected. On top of the mafic amphibolite is a layer of dark black hornblende, which directly contacts a heavily deformed, 3 m thick layer of green chlorite schist. The chlorite schist is capped by a 3 cm thick garnet quartzite, which also contains an Fe-oxide. The quartzite is gently undulose, resting on the boudins of the chlorite schist below. The quartzite then directly contacts more paragneiss, from which DV22-4B was collected.

The next outcrop encountered upstream is an 8 m thick section of chlorite schist with two ~0.5 to 1 m thick mafic layers, which contain rutile. The second mafic layer also contains folded quartzite interlayers. After this, moving upstream, is an outcrop with more complicated lithologic relationships. Two limbs of a meter-scale fold are present, each consisting of a ~0.5 m thick chlorite schist with interleaved mafic amphibolite and topped by a layer of quartzite. The limbs of the fold are oriented N25W dipping 48°W and N60E dipping 80°N. The fold axis is plunging 55° to the north. On the inside of the fold are two ~1 m long pods of talc-actinolite schist, which probably represent metasomatized ultramafic material. Past this outcrop is an approximately 10 m thick layer of chaotically folded material consisting of strung-out chlorite schist, mafic amphibolite, talc-actinolite,

and quartzite all boudinaging together. All of the units are repeatedly juxtaposed against each other as you move upstream.

This is followed by an area of tightly folded paragneiss with garnet quartzite horizons (where DV22-7 was collected), that transitions into more coherent, undeformed paragneiss. Paragneiss continues up the main streambed of the Dawn Valley, with regular interlayers of the other lithologies. Usually less than 1 meter thick, the interlayers at times consist of a single lithology, such as mafic amphibolite or chlorite schist, or at times appear in pairs. A mafic amphibolite and quartzite layer were observed directly contacting paragneiss, while elsewhere were boudins of mafic material interleaved with paragneiss. Tight isoclinal folding and abundant quartz veins were observed throughout. Garnet is visible in the paragneiss in this upper section of the traverse.

These relationships are best exposed in a side gully that branches off the main Dawn Valley streambed near its northeastern termination. This gully cuts steeply into the hillside and exposes ~40 m of continuous bedrock (Figure 3). At the bottom and the top of this side gully are thick packages of paragneiss with occasional thin (~0.5 to 2 m) thick layers of chlorite schist and isolated layers of garnet quartzite (~2 cm thick). In the middle, however, is an ~14 m thick package of mafic and metasomatic rocks. Moving upslope, a layer of tightly folded chlorite schist gives way to approximately 2 m of lighter-colored talc schist. Within the chlorite schist is an undeformed block of mafic garnet amphibolite (DV20-04; Figure 9a) and another pod of mafic material wrapped in a ~10 cm thick fold of garnet quartzite (DV22-12, Figure 9b). The talc schist transitions back into chlorite schist, which then alternates with layers of foliated mafic amphibolite of variable thickness until paragneiss returns farther upslope. Isoclinal folds were

observed throughout this middle package, and a similar folding pattern continues into the paragneiss above.

Continuing uphill from this side gully, paragneiss exposures are less frequent but are still associated with chlorite schist and quartzite layers (Figure 8b). Once the top of the ridge is reached, numerous folds and small faults are observed in the paragneiss. One fault, striking N55W, has near vertical paragneiss on one side and shallower west dipping paragneiss on the other. A chevron fold was observed approximately 3 m away from a gently curving fold. The structures on top of the ridge reveal significant meter-scale complexity in the upper Dawn Valley paragneiss, which continues until the amphibolite mélange is reached farther up the ridge.

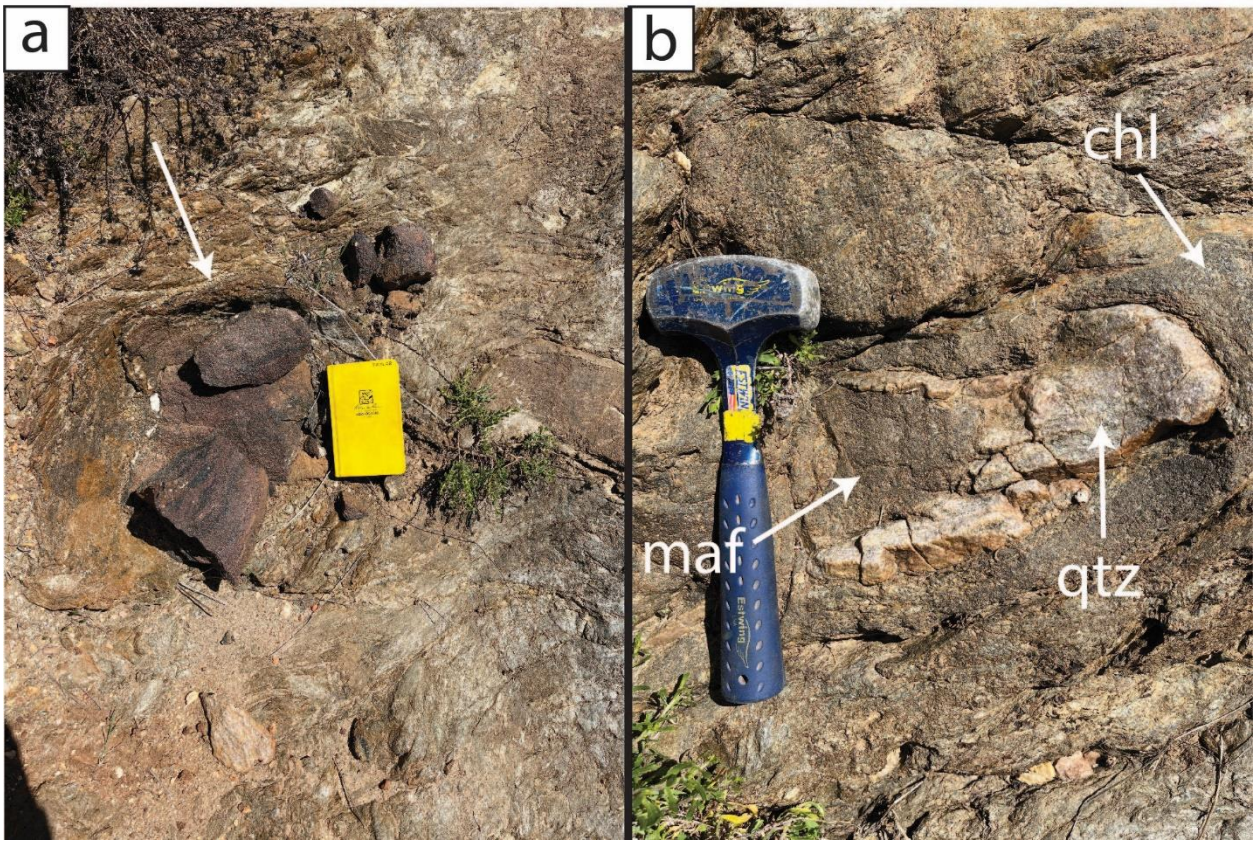


Figure 9. ***a****. Garnet-hornblende block DV20-04 in the Dawn Valley side gully. Block is surrounded by a matrix of chlorite schist. Parts of the block have broken off and are sitting as float on top of the schist.* ***b****. Upslope from the view in (**a**) is a folded garnet quartzite layer (qtz). On the inside of the fold is mafic material (maf), while the outside is a matrix of chlorite schist (chl).*

Cottonwood Canyon

Hiking trails heading south from the island's airport go past several blocks in amphibolite mélange. In the bank of a stream is the only known exposure where coherent mafic amphibolite directly contacts mélange (Figure 10). It is apparent in outcrop that the mélange and coherent rocks are discordantly juxtaposed. No visible reaction zone was observed between them.

To the southwest of the contact, and moving down stratigraphically through the coherent amphibolite, is a pair of conjugate faults that were previously described by Grabiec

(2017). The larger of these is a near vertical, ~0.75 m wide channel infilled with mélange matrix. Both the hanging wall and footwall are coherent mafic amphibolite, and the schistose matrix appears to have flowed into the channel while the fault was active. Some low temperature reactivation of the faults is evidenced by pumpellyite in the fault zone. Slickenfibers were observed on both faults.

Farther west a short distance is the contact between the coherent amphibolite and the Ollas thrust, which separates the coherent amphibolite from the underlying epidote blueschist. The Ollas fault zone has previously been described by Harvey et al. (2021a). The coherent amphibolite becomes tightly folded as it approaches the fault zone, which is made up of several amphibolite-grade mafic blocks entrained in two mineralogically distinct, but highly deformed, matrices.

From its contact with the amphibolite mélange at the top to the Ollas thrust at its base is about 450 m vertical thickness of coherent mafic amphibolite. No paragneiss or other lithologies are observed in the Cottonwood Canyon coherent amphibolite. No garnet or rutile were observed in the Cottonwood Canyon amphibolite, though rutile is found within the Ollas fault zone (Harvey et al., 2021a).

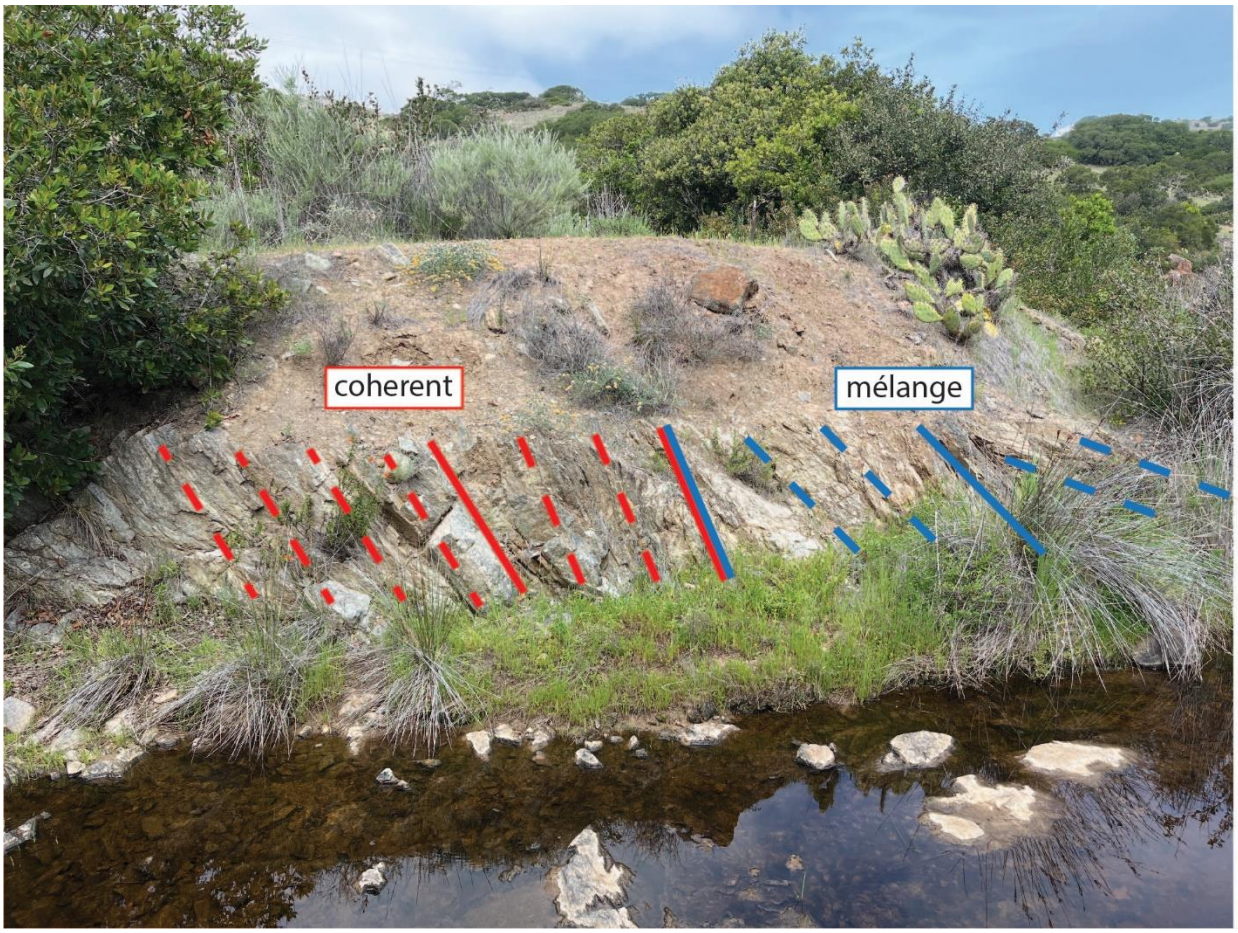


Figure 10. The contact between coherent amphibolite and amphibolite mélange in Cottonwood Canyon. Solid lines separate rocks with distinct orientations, and dashed lines indicate a schematic estimate of the dip angle for the coherent (red) and mélange (blue).

Buffalo Springs

A traverse of similar length to Cottonwood Canyon can be found by hiking up the Buffalo Springs Canyon, east of the airport. Buffalo Springs lacks, however, clear and direct contacts between the coherent amphibolite and its surrounding units. At the base of the traverse is an enigmatic outcrop where blueschist is juxtaposed against talc and epidote schists, which may be related to the Ollas fault zone, but this was impossible to determine in the field. Farther upstream is a low, ~12 m long outcrop in the stream bank that exposes what is unambiguously mafic coherent amphibolite. A layer of chlorite

schist is found within the mafic layers. Moving northeast, exposures of green and black mafic amphibolite continue to be seen near the stream and on the hillsides until amphibolite mélange matrix is encountered.

Sheep Chute

Off of Empire Landing Road, west of the island's airport, is a ridge with several small exposures of highly weathered bedrock. Both garnet-bearing paragneiss and rutile- and garnet-bearing mafic amphibolite were observed in close proximity to one another. The mafic amphibolite may have been a layer within the paragneiss. The rocks here are poorly consolidated.

Structural Measurements

The strikes and dips of foliation measured using the app Clino are largely consistent with those measured using a traditional compass, and with those reported previously by Platt (1975; 1976). The coherent amphibolite generally strikes NW-SE and dips ~45° to the NW, although there is spread in the data due to localized folding (Figure 11). The average orientation was determined using the mean vector calculation of the freely available program Stereonet 11 (https://www.rickallmendinger.net/stereonet).

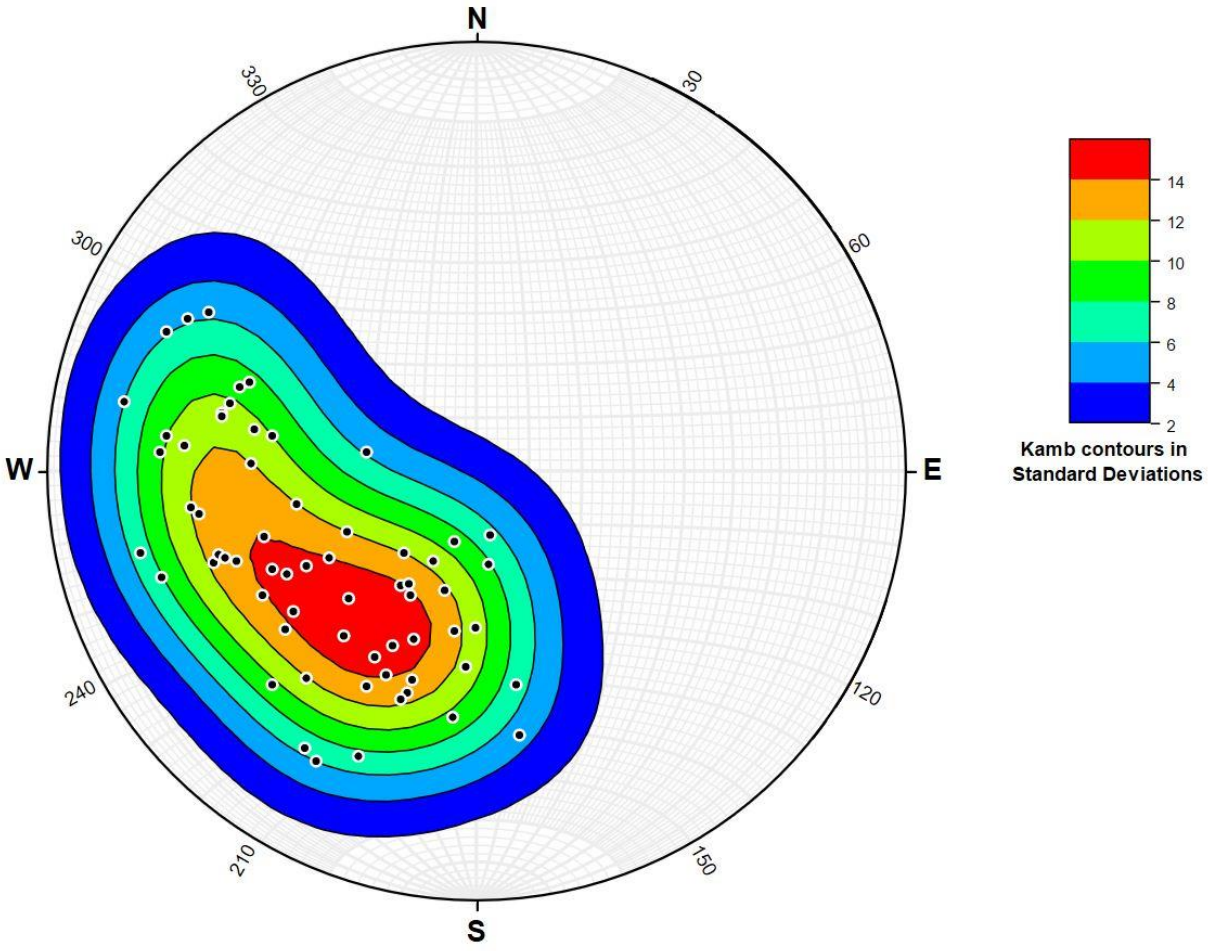


Figure 11. A stereonet plot of poles to foliation (n=64) in the coherent amphibolite. Coloured contours indicate standard deviations using the Kamb (1959) method. Produced using Stereonet 11 (Allmendinger et al., 2012; Cardozo and Allmendinger, 2013).

Petrography

Mafic Amphibolites

The mafic constituent of the coherent amphibolite is composed primarily of calcic clinoamphibole (henceforth referred to as Ca-amphibole), epidote group minerals, and plagioclase, and contains variable amounts of chlorite, white mica, quartz, titanite, ilmenite, rutile, garnet, and the minor phases zircon, apatite, and pyrite (identified using EDS on the EPMA).

The Ca-amphibole varies in color and modal proportion moving up section through the coherent amphibolite. At its base, actinolite is the amphibole phase. It is lightly colored in plane polarized light and makes up roughly 30% of the rock. In the Rattlesnake traverse, the actinolite pleochroism is colorless to pale green-yellow. In the CA traverse, it is tan to light green. The amphiboles grade gradually upwards into darker colors, indicative of a transition to hornblende compositions (Figure 12a-d). CA22-1, from roughly the stratigraphic middle of the coherent amphibolite, shows light yellowish green to blue green to green pleochroism. A mafic layer within paragneiss in the upper Dawn Valley traverse, near the top of the coherent amphibolite, contains amphibole that is brown to dark green. The modal proportion of Ca-amphibole also gradually increases, going from 30% at the base to roughly 85% near the top of the coherent amphibolite. Ca-amphibole typically appears as elongate tabs or rhombs, or as masses interstitial with epidote. Most range from 0.5 to 1.5 mm in length, with the most coarse-grained going up to 5 mm. They are often altered along fractures and cleavages.

The mafic amphibolites usually contain either clinozoisite or epidote (differentiated on the basis of optic sign). Samples from lower in the coherent amphibolite are more likely to contain clinozoisite, while samples from higher in the section are more likely to contain epidote, although the gradation from one to other is not consistent. Their modal proportions vary, ranging from around 50% of the most epidote-rich samples to <5%; the amount of epidote group minerals is generally highest at the base of the coherent amphibolite and decreases until almost all epidote is gone in the upper parts of the section. The epidote group minerals occur in three different ways in these samples. First, they most commonly appear as small (<0.5 mm) sub-rounded or pill-shaped grains that

display 1st order grey and/or anomalous blue interference colors in cross-polarized light (Figure 13a). Second, they sometimes occur as sub-rounded grains with irregular zoning defined by either 3rd order blue-yellow interference colors or 3rd order yellow and magenta interference colors, with the latter showing simple twins (Figure 13b). Lastly, the epidote group minerals are sometimes observed as euhedral diamond-shaped grains with 1st order grey interference colors that display "fir-tree" sector zoning (Figure 13c). This last group sometimes shows preferential dissolution of the darker fir-tree zones as demonstrated by replacement with hornblende in the interiors of these grains. The fir-tree sector zoning, while distinct in XPL, was not visible in back-scatter electron (BSE) mode on the SEM. In WB22-6, the distribution of Group II and Group III epidotes defines the sample's layering.

The felsic minerals in the mafic amphibolites are more commonly plagioclase feldspar, with minimal quartz present. Plagioclase usually appears as sub-rounded interstitial grains that often contain numerous micro-inclusions. A few samples display polysynthetic twinning. Plagioclase in the mafic amphibolite is often saussuritized. In the mafic amphibolite samples, the degree of saussuritization varies. Some plagioclase grains are unaffected, some show distinct epidote group crystals forming in their interiors or along cracks, as well as epidote-plagioclase symplectite textures, and some show complete conversion of plagioclase to dense networks of epidote group crystals. This variation is sometimes observed within a single sample (Figure 14).

The two key minerals for this project are garnet and rutile. In the mafic amphibolites, garnets range from ~0.3 to ~2.8 mm in diameter. They are typically euhedral, heavily fractured, and rich in inclusions. The largest garnets, in DV16-03B, contain sinusoidal

titanite inclusion trails. The most common inclusion phase in mafic amphibolite is zircon; quartz is uncommon. Garnet is limited to the upper sections of the coherent amphibolite. Rutile usually occurs as small (~0.05-0.35 mm) grains and is similarly confined to the upper coherent amphibolite (see lines on Figure 6 and Figure 3 and Figure 4). In DV16-03B, rutile is found only in the cores of titanite grains, presumably the result of later retrogression to titanite.

There are a few notable outliers in the mafic amphibolite samples. WB22-3, from lower down in the Rattlesnake traverse, contains several grains of heavily altered clinopyroxene (Figure 15). These grains are often interstitial and show dissolution around their edges. They are altered to fine-grained masses along their cleavage planes. Overall, they appear to be older than the grains that surround them. Pyroxene was not observed in any other sample from the coherent amphibolite.

WB22-1 was identified as a grayschist and part of the coherent mafic amphibolite in the field, but in thin section looks drastically different from the rest of the mafic samples (Figure 16). It is made up of fine, fibrous chlorite-rich layers alternating with layers of undulatory (in XPL) plagioclase. Some muscovite and Ca-amphibole are present in the chlorite-rich layers. There are tabular euhedral epidote group minerals, about 3.5 mm across, that have dissolved around their edges. Chlorite porphyroblasts (~1 mm) are interpreted to be entirely chloritized garnets, as evidenced by their generally round shape, inclusions, and relict strain shadows. While most of the plagioclase is smaller (~0.1 mm), subrounded, and dynamically recrystallizing, some large grains (~1.5 mm), rich in inclusions and displaying Carlsbad twinning, are seen recrystallizing around their edges. There are rutile grains retrogressed to grungy titanite around their rims. Lastly, there are

abundant small (<0.05 mm), black grains of graphite throughout the sample, not observed elsewhere in the mafic amphibolite.

DV20-04 is a mafic amphibolite block found within a talc schist in the upper Dawn Valley traverse. It differs from the surrounding mafic amphibolites in several key ways. First, it contains a higher proportion of garnet (~70%). Its garnets are also larger, going up to ~4.5 mm in diameter and rounded in shape, and often display "atoll" growth patterns, in which a garnet core is completely interrupted by a mantle of inclusions and then surrounded by a garnet rim (Figure 17). The garnets also contain abundant exsolution needles of rutile (confirmed on the EPMA), which are not observed elsewhere in the mafic amphibolite (Figure 18). Second, the hornblende in this block is tan to brown and generally granoblastic polygonal in texture. By contrast, a nearby mafic layer within paragneiss (DV20-05A) shows strongly foliated, brown to dark green, elongate hornblende crystals and a lower proportion of garnet (~20%; Figure DV20-05A). Its garnets are also euhedral, smaller (~0.5-1.5 mm), and lack exsolution needles.

Paragneiss

The sedimentary-derived paragneiss samples contain quartz, plagioclase feldspar, potassium feldspar, biotite and/or muscovite, garnet, rutile, and sometimes Ca-amphibole, as well as minor ilmenite, hematite/magnetite, pyrite, zircon, and apatite (minor phases identified with EDS on the EPMA). Unlike the mafic amphibolites, which showed variation across the coherent amphibolite, the paragneiss samples are fairly consistent. Their foliation is defined by mica-rich and plagioclase/quartz-rich layers (Figure 19e). The garnets are typically ~0.8 to ~1.5 mm in diameter and are heavily altered by fractures and dark, opaque masses of alteration products. They are generally rich in inclusions and

often have dense inclusion clouds concentrated in their cores (Figure 19b). The rutile are abundant and are typically tabular or arranged in masses in the matrix. They often show dissolution textures around their rims. Rutile included in garnet are smaller and more euhedral. Mica grains are often intertwined and show kink banding (Figure 19c). The size distribution of quartz and plagioclase grains suggests that they experienced dynamic recrystallization (Figure 19d). Plagioclase is often completely saussuritized into dark, fine-grained masses.

Quartzite

The quartzite samples from the coherent amphibolite consist predominantly of quartz (~80%) and garnet (10-20%). They also contain rutile, often arranged in masses, a sheet silicate (either biotite or chlorite), some Ca-amphibole, epidote, plagioclase, and minor zircon and apatite. Ilmenite and titanite are sometimes seen rimming rutile (identified using EDS on the EPMA). There is some evidence for multiple generations of garnet in quartzite. The majority of garnets are around (<0.1 to ~0.5 mm) in diameter and euhedral. They are either colorless in plane polarized light, light red in color, or optically zoned with a red core and colorless rim (Figure A.1c in Appendix A). The quartzites also often contain a few larger (~1 mm), rounded garnet grains that are fractured and more rich in inclusions. They more closely resemble the garnets in the paragneiss (Figure A.1d). In some samples (e.g., CA22-2A-2), the garnets are arranged in thin layers, whereas in others they are distributed throughout. The quartz in these samples range from ~0.2 to 1 mm in size, are generally subhedral, and show evidence for dynamic recrystallization (Figure 19e). In DV22-7, a secondary quartz vein was observed cutting across the main rock fabric. It contains a network of orbicular, radiating quartz crystals.

Schists

Two varieties of schist were observed in the coherent amphibolite. The more abundant chlorite schist was too friable for making thin sections. The talc schist was observed only in the upper section of the Dawn Valley traverse. In thin section, it is roughly 95% talc with some amphibole porphyroblasts.

Textures

In addition to the foliation observed throughout the coherent amphibolite, mineralogical layering is also observed in some samples. As previously mentioned, WB22-6 contains zones that are differentiated by epidote's appearance.

Some secondary features are recorded in these rocks as well. In addition to the quartz vein in DV22-7, a millimeter-scale, boudinaged shear zone was observed in the mafic amphibolite WB22-6 (Figure 20). It is filled with larger hornblende and epidote grains surrounded by a fine-grained mass of quartz. The crystals have a preferred orientation at about 45 degrees from the walls of the shear zone. SEM images of the shear zone are shown in Figure 21.

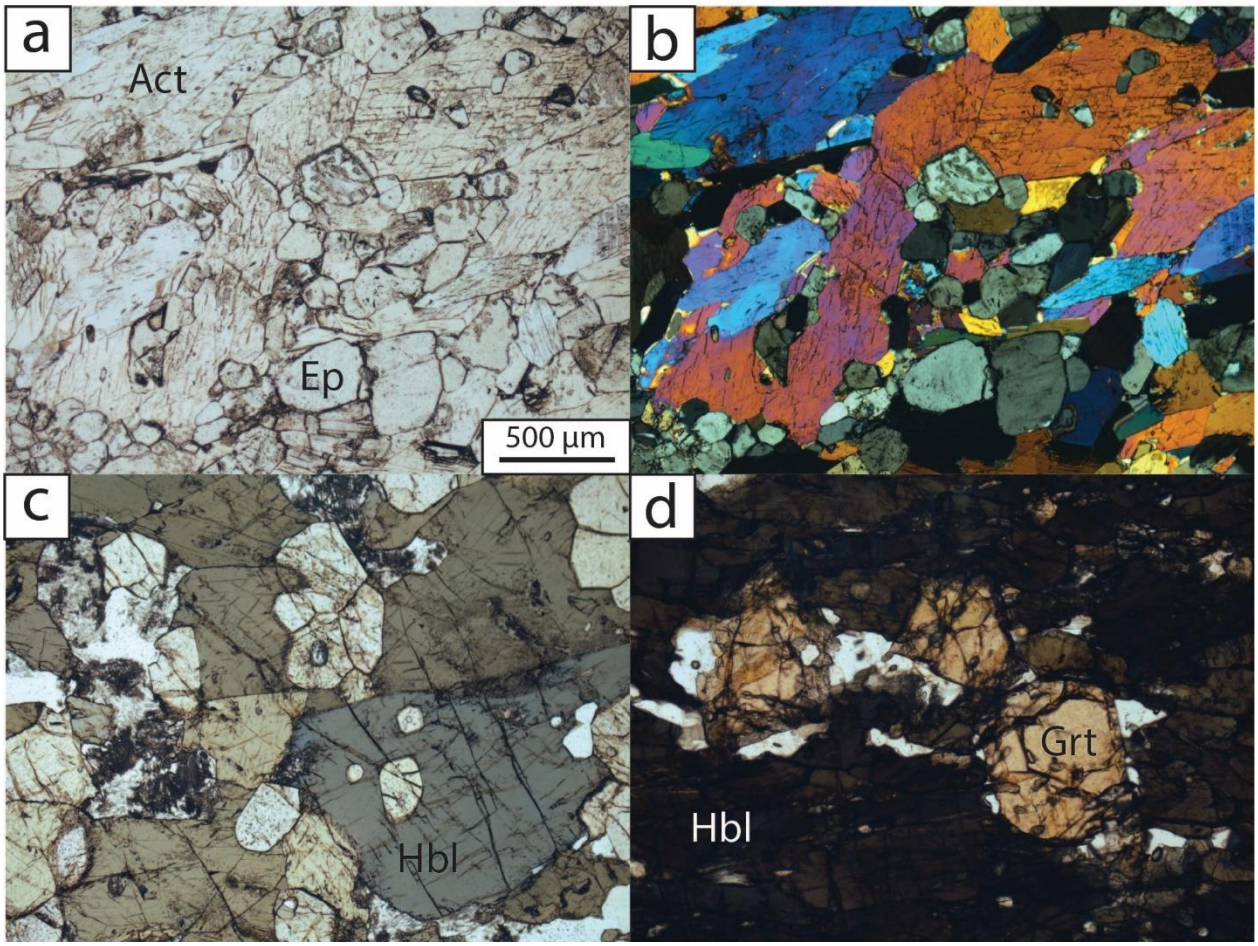


Figure 12. Photomicrographs of representative Ca-amphiboles from the mafic amphibolite. All images are 5x magnification. ***a****. Actinolite is near colorless in the lower section of the coherent amphibolite (plane polarized light [PPL], WB22-4A).* ***b****. Identical view as in (a), in cross polarized light (XPL).* ***c****. In middle of coherent amphibolite, the Ca-amphibole is now brown to blue-green hornblende (PPL, CA22-1).* ***d.*** *In a mafic layer within paragneiss in the upper section of the coherent amphibolite, hornblende is now dark green. Note that this is a 100-µm thick section, which amplifies the color darkening (PPL, DV20-05A). Mineral abbreviations throughout are after Whitney and Evans (2010).*

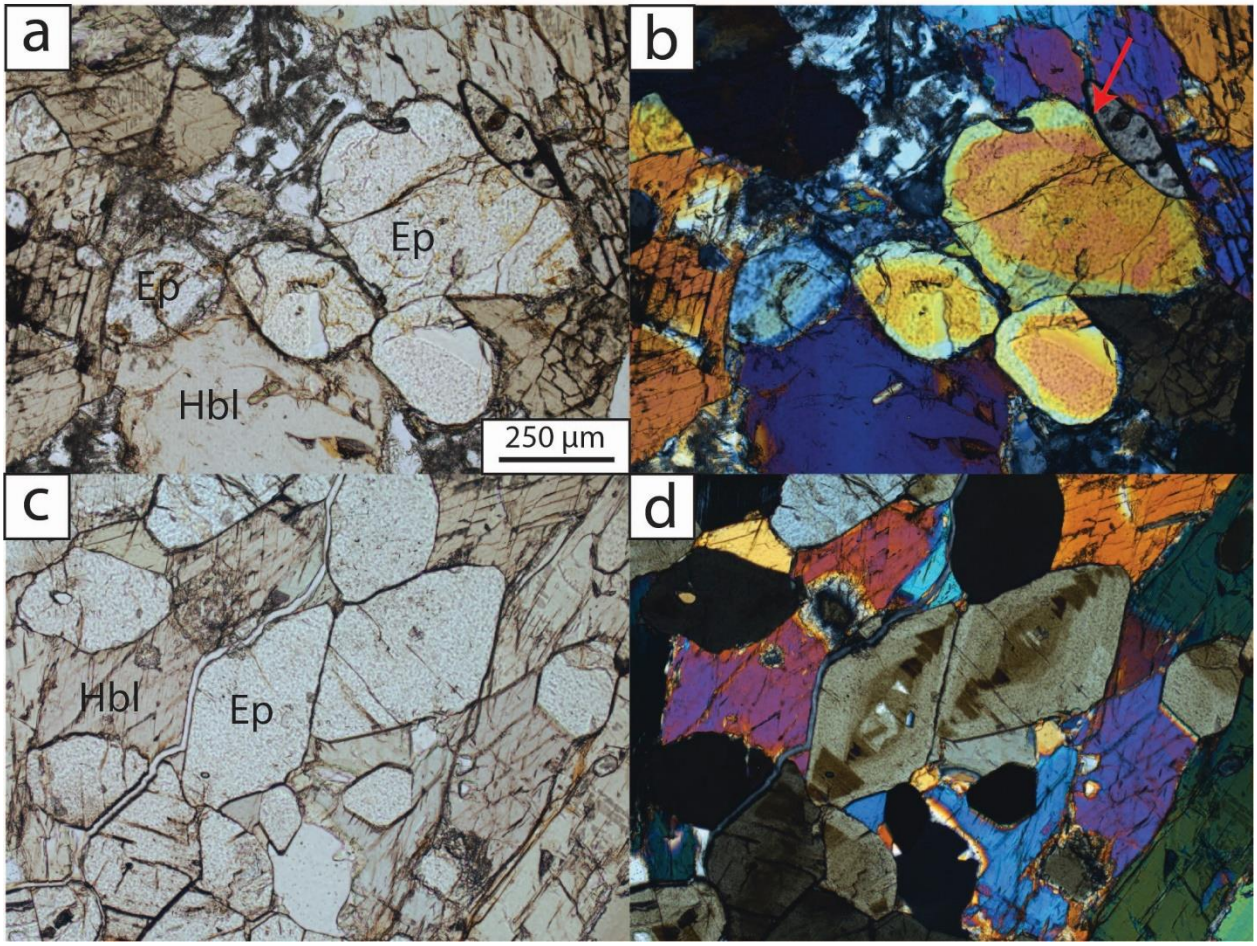


Figure 13. Photomicrographs of epidote group minerals in a mafic amphibolite (WB22-6). All images are 10x magnification. ***a.*** *Mid to high relief, sub-rounded grains of epidote group minerals (PPL).* ***b.*** *Identical view as in (a), in XPL. Note the zoned 3rd order orange, yellow, and blue interference colors. Red arrow is pointing to the hinge of a Carlsbad twin in the larger grain.* ***c.*** *Euhedral, diamond-shaped epidote group minerals (PPL).* ***d.*** *Identical view as in (c), in XPL. The epidotes show 1st order gray to anomalous khaki interference colors. Note the fir-tree sector zoning.*

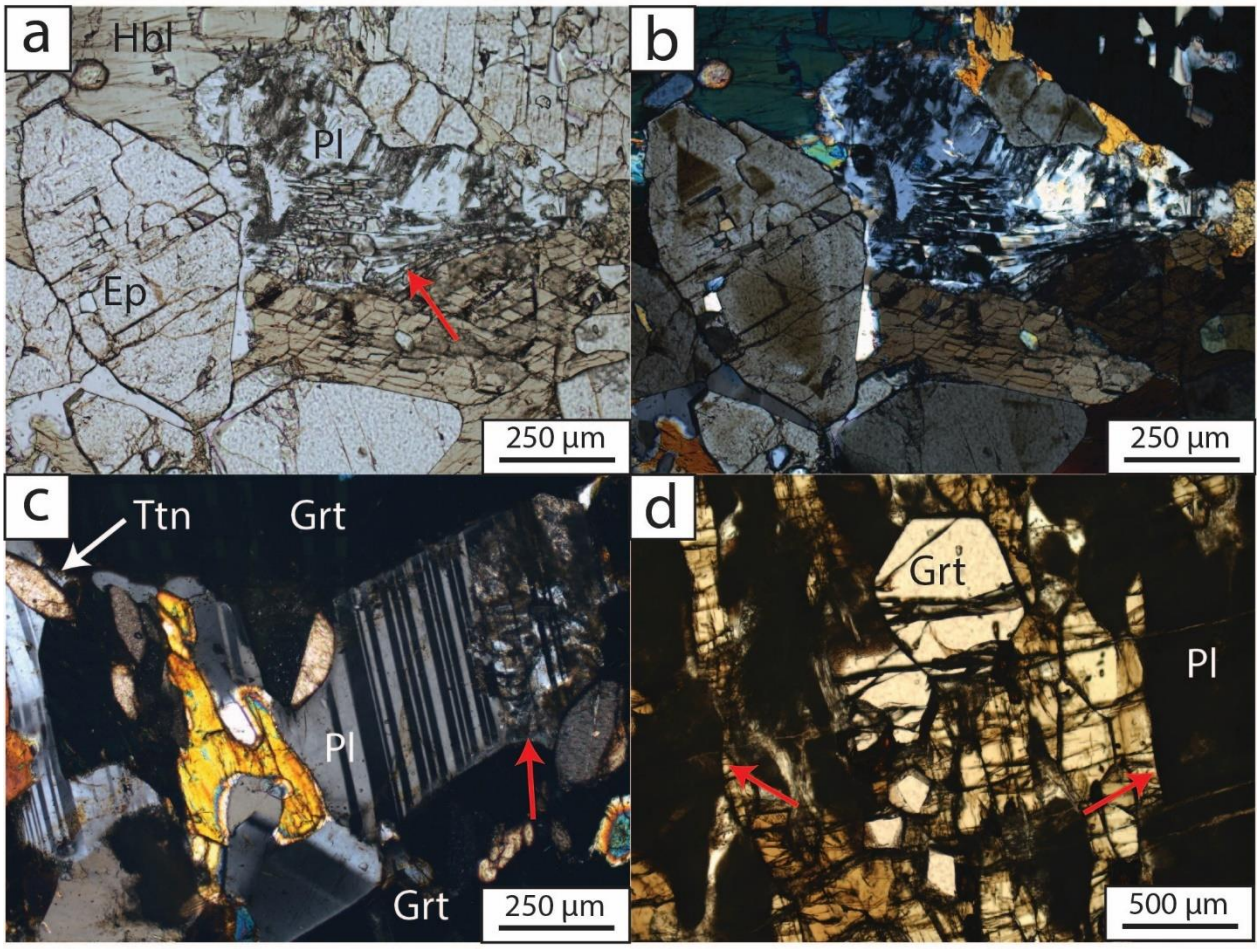


Figure 14. Photomicrographs of representative plagioclase feldspar in mafic amphibolite. ***a.*** *Incipient saussuritization in a plagioclase grain. Distinct needles of epidote group minerals are present. The red arrow is pointing to epidote and plagioclase symplectite (10x, PPL, WB22-6).* ***b.*** *Identical view as in (a), in XPL.* ***c.*** *Partially saussuritized (red arrow) plagioclase between two garnets. Grain still retains its polysynthetic twinning. Lens shaped titanite is also present (10x, XPL, CA16-01).* ***d.*** *Plagioclase (red arrows) fully saussuritized to dark, fine-grained masses. Note that this is a 100-µm thick section (5x, PPL, DV22-5).*

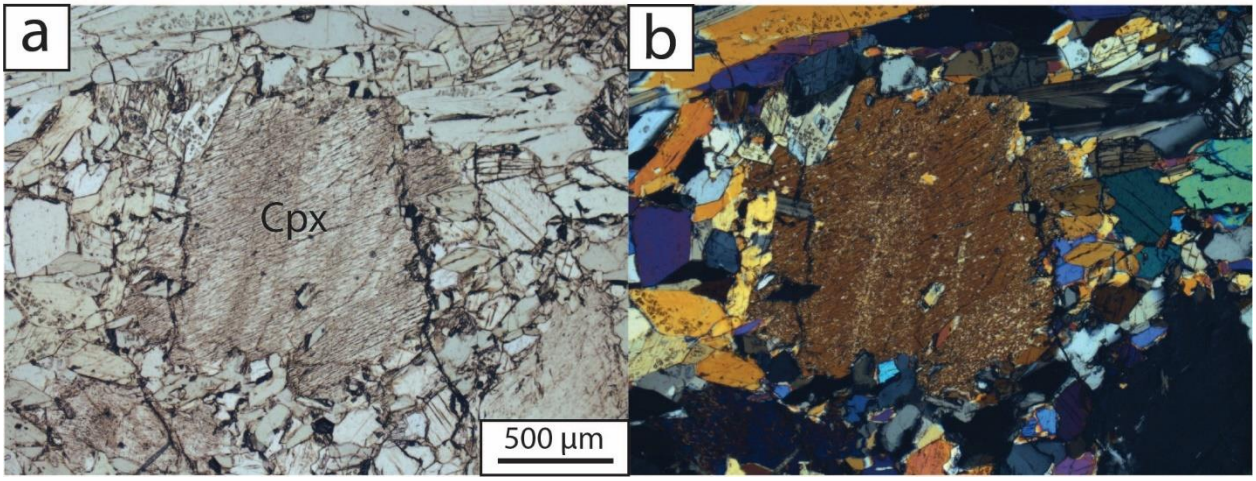


Figure 15. Photomicrographs of calcic clinopyroxene in a mafic amphibolite (WB22-3). ***a****. In PPL, and (****b****) in XPL. Note the disequilibrium textures around the edges of the grain. Both images are 5x magnification.*

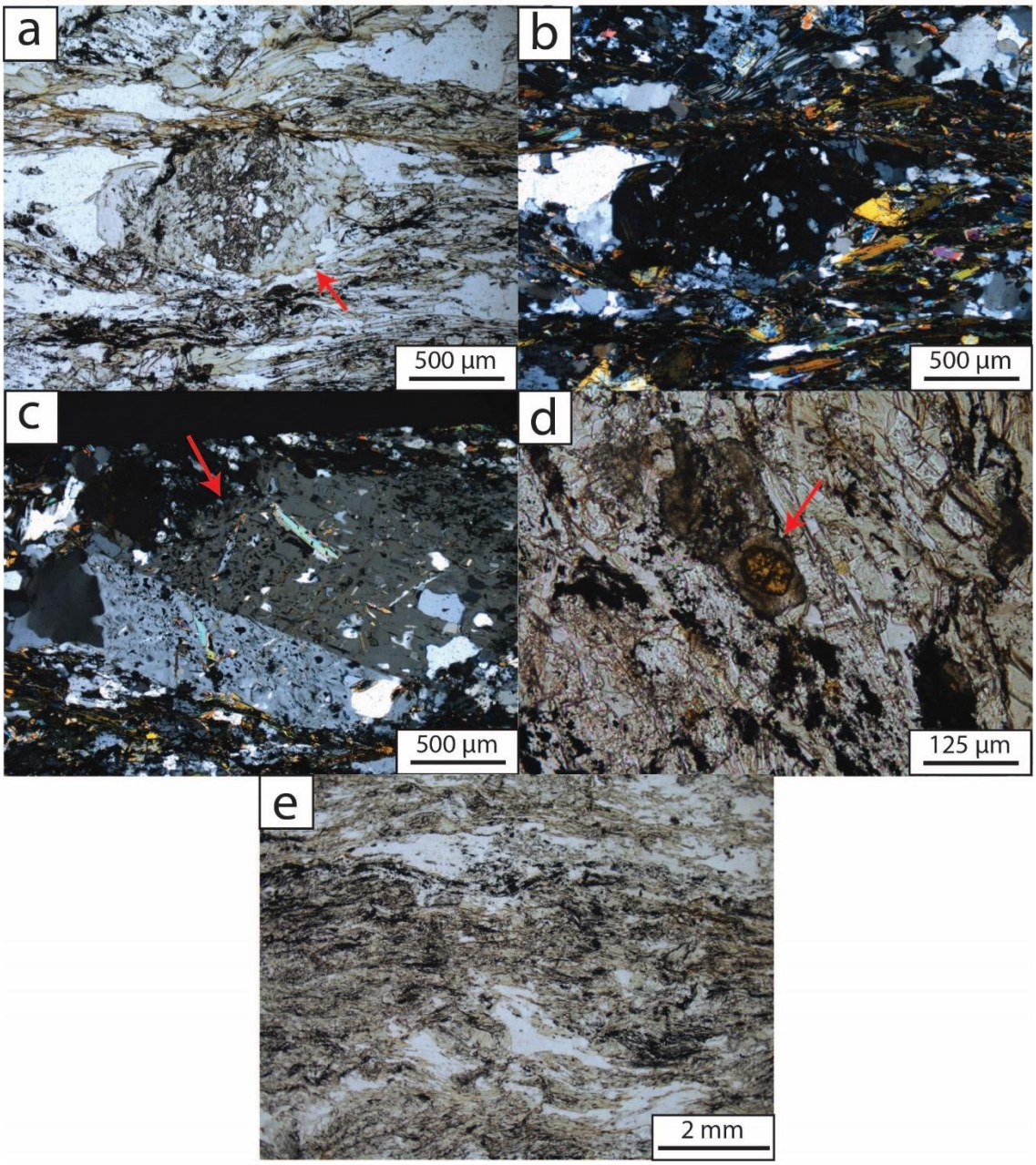


Figure 16. Photomicrographs of features in the mafic amphibolite WB22-1. ***a.*** *Chloritized garnet porphyroblast with relict strain shadows. Matrix is predominantly muscovite, chlorite, and black graphite (5x, PPL).* ***b.*** *Identical view as in (**a**), in XPL.* ***c.*** *Simply twinned, inclusion-rich porphyroblast of plagioclase (5x, XPL).* ***d.*** *Yellow-orange rutile surrounded by grungy titanite rim (20x, PPL).* ***e***. *The foliation of WB22-1 is defined primarily by sheet silicates and black, fine-grained graphite (1.5x, PPL).*

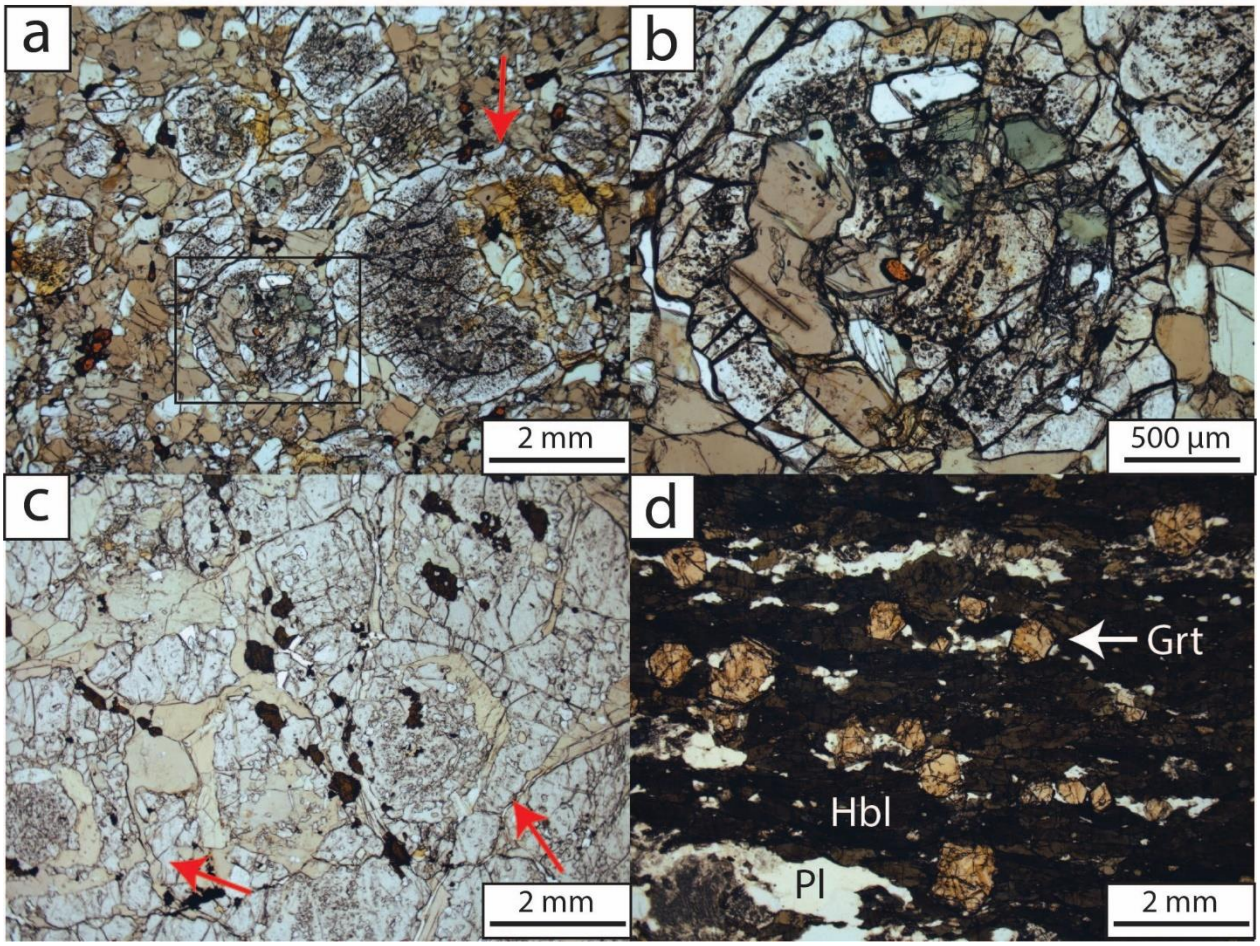


Figure 17. ***a.*** *Atoll garnets in DV20-04, a mafic block in chlorite schist in the coherent amphibolite. Arrow points to largest grain (1.5x, PPL). Black box indicates field of view in (**b** [5x, PPL]). Note the granoblastic polygonal green-brown hornblende.* ***c.*** *Atoll garnets (red arrows) in a mafic block in amphibolite mélange (1.5x, PPL, CA16-02A).* ***d.*** *Garnets and foliated dark-green hornblende in a mafic amphibolite layer near DV20-04 (1.5x, PPL, DV20-05A). Note that (**a**), (**b**), and (**d**) are 100-µm thick sections.*

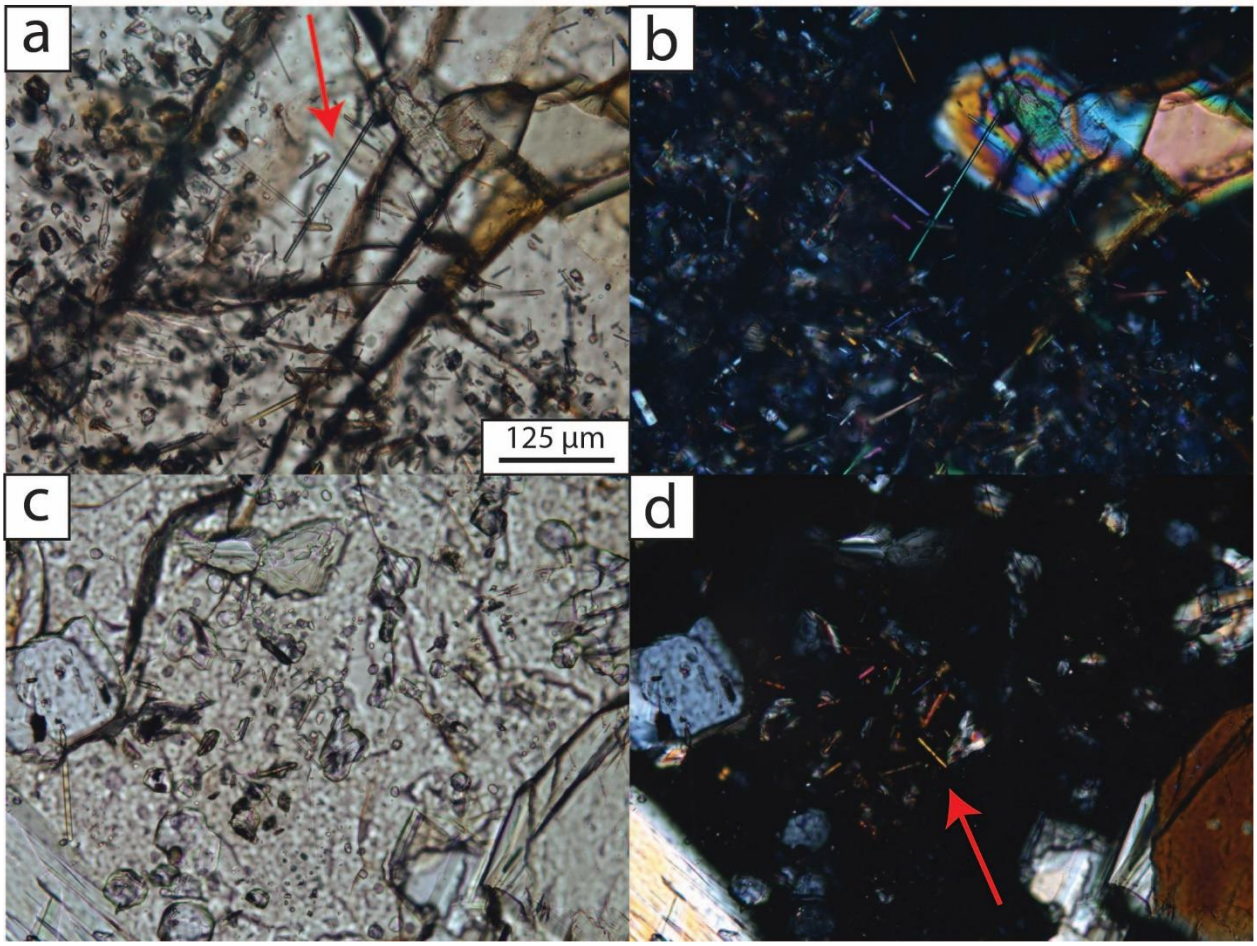


*Figure 18. Photomicrographs of rutile exsolution needles in garnet in the mafic blocks DV20-04 (**a** and **b**), from the coherent amphibolite, and CA16-02A (**c** and **d**), from the amphibolite mélange. All images are 20x magnification. (**a**) and (**c**) are PPL, and (**b**) and (**d**) are XPL. Arrows point to prominent needles. Note that (**a**) and (**b**) are from a 100-µm thick section.*

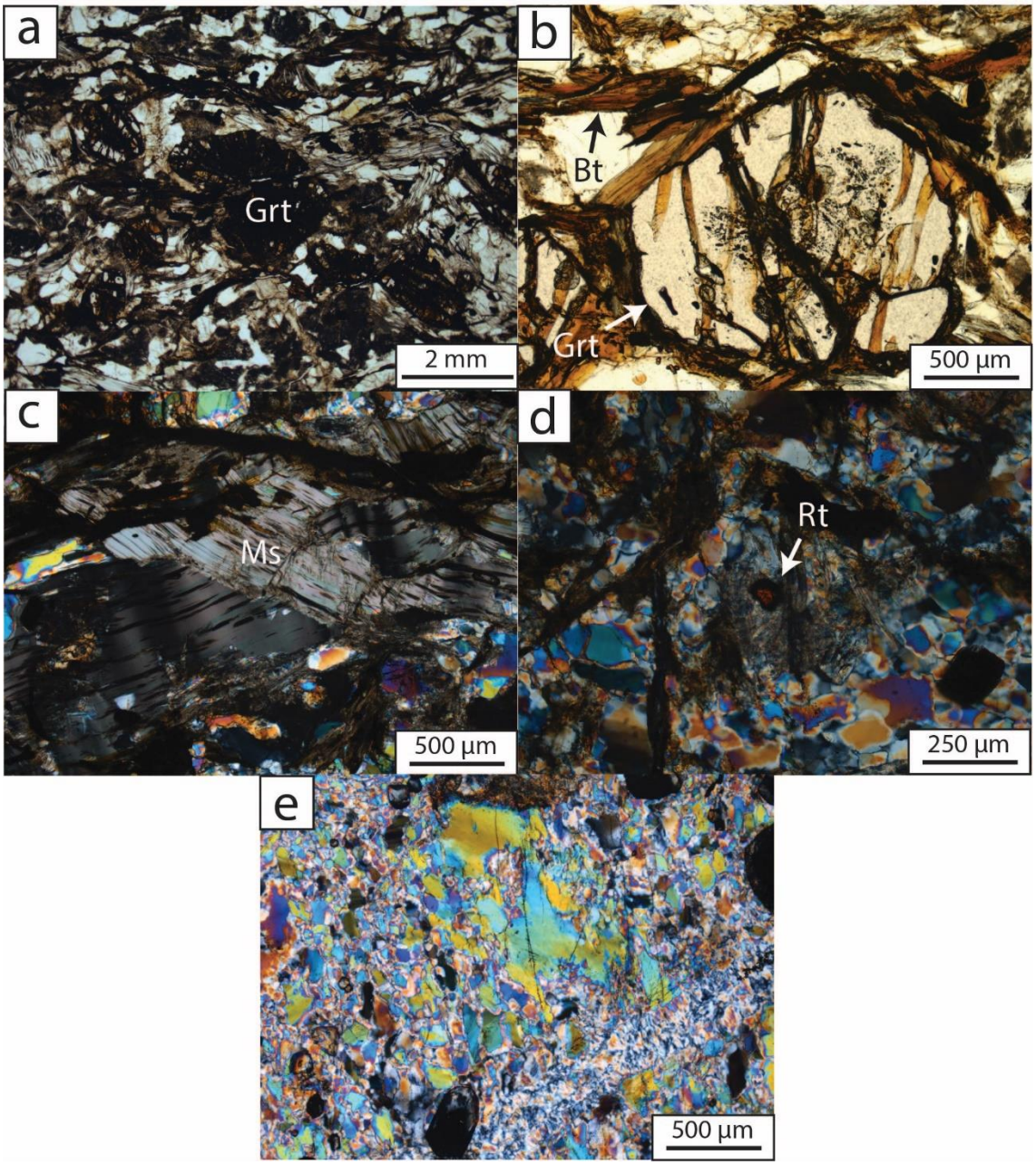


Figure 19. Photomicrographs of paragneiss samples (a-d) and a quartzite sample (e). Note that all five are from 100-µm thick sections. ***a****. Heavily altered garnets and a foliation defined by micas (1.5x, PPL, DV16-04B).* ***b****. A garnet with an inclusion cloud in the center (5x, PPL, DV22-4B).* ***c****. Kink bands in muscovite. Interference colors are elevated to 4th order by section thickness (5x, XPL, DV16-04B).* ***d****. Dynamic recrystallization in quartz (brightly colored, low relief grains). Interference colors are elevated due to section thickness (10x, XPL, DV16-04B).* ***e.*** *Quartzite sample DV22-7 showing quartz grain sizes ranging from ~0.2 to 1 mm across. Note that quartz appears in bright 2nd/3rd order interference colors (5x, XPL).*

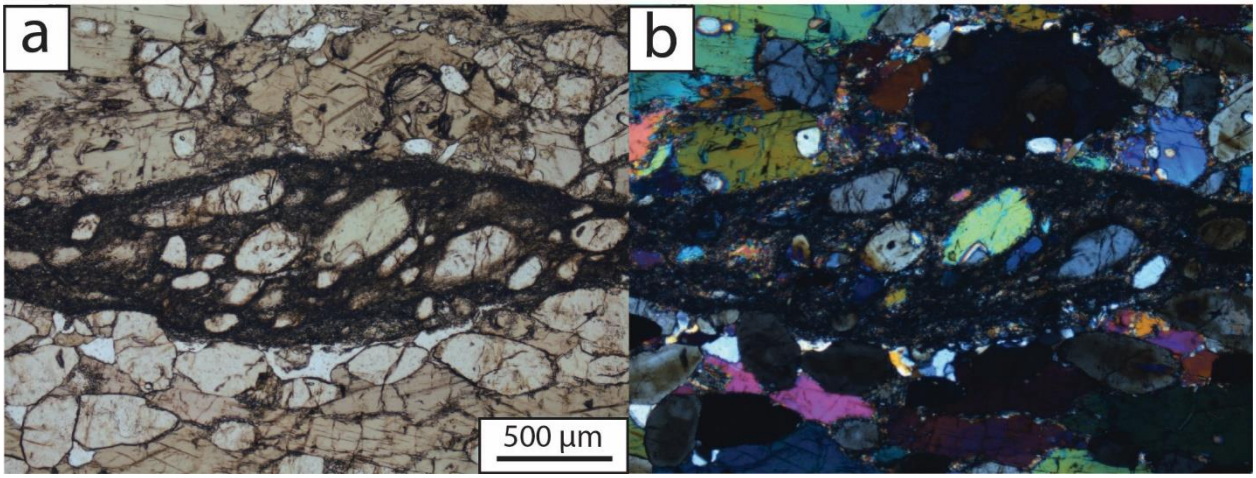


*Figure 20. Photomicrographs of a boudin in a shear zone in a mafic amphibolite (WB22-6), in PPL (**a**) and XPL (**b**). Both images are 5x magnification. The feature is filled with a dark, fine-grained mass of crystals and larger grainss of hornblende and epidote group minerals. The shear zone extends laterally across the width of the thin section.*

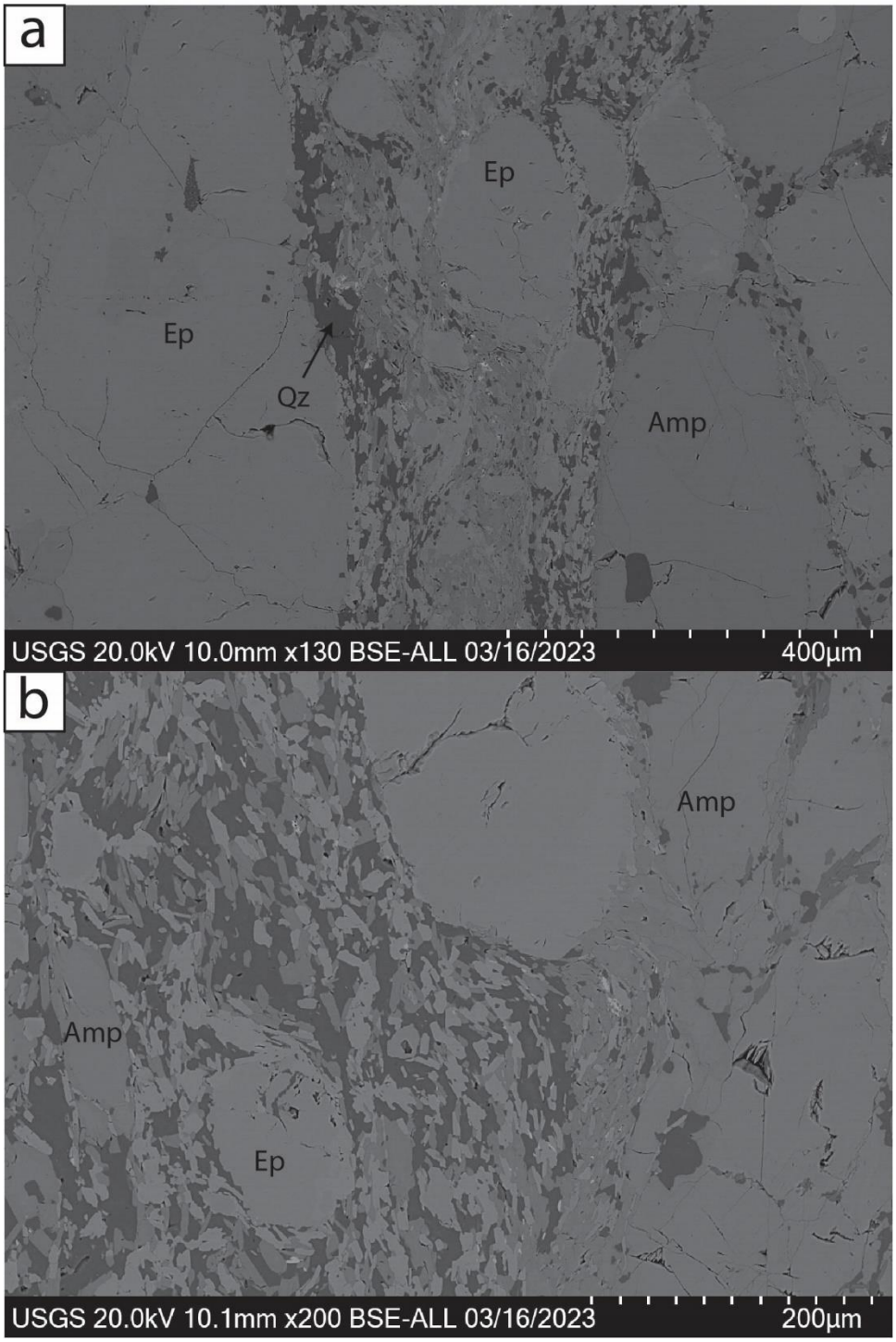


Figure 21. SEM back scatter electron (BSE) images of shear zone in WB22-6 (here oriented north-south). EDS spectra confirmed that the major minerals inside the shear zone are the same as the wall rock: amphibole and epidote. The dark interstitial phase is quartz. ***a.*** *130x magnification.* ***b****. 200x magnification.*

Quartz-in-garnet Barometry

Garnet Chemistry

Two garnets in the paragneiss sample DV22-4B were analyzed with 5 rim-to-rim WDS spots each and have an average composition of 60% almandine, 29% pyrope, 9% grossular, and 1% spessartine (Figure 22a and Appendix A.1). Garnet 25 and Garnet 29 have radii of approximately 550 and 840 μm, respectively. Their profiles closely resemble one another, with slight decreases in Fe and increases in Ca in their rims in otherwise flat profiles. Their pyrope and spessartine profiles are flat. Their zonation is subtle enough to not significantly impact QuiG calculations (see Figure 23), and so the average composition was determined by taking a simple mean of all the analyses. No equation of state for spessartine is available at this time, so the results were renormalized without spessartine. The average paragneiss garnet composition used in the QuiG calculations is therefore 61% almandine, 29% pyrope, and 9% grossular (with rounding). Figure 23a shows that the effect of varying the endmember proportions is minimal. The difference between pure grossular and pure almandine is within the 2σ uncertainty range of a single sample (CA22-2A-2 in the figure). Pyrope produces a slightly lower isomeke, although the weighted average for CA22-2A-2 still overlaps with pure almandine.

Garnets in two quartzite samples were analyzed for major element chemistry. Profiles in all garnets were relatively uniform (Figure 22). Most garnets were small and euhedral with radii <150 μm, so only partial (core-to-rim) traverses were measured. The exception is G1 in DV22-7, which is less euhedral and large enough (radius ~240 μm) for a rim-to-rim traverse. The garnets within each of the two analyzed samples are fairly similar to

each other. G1 in DV22-7 deviates negligibly from the more euhedral grains Q2 and Q8. All of the quartzite garnets have significantly higher spessartine content than the paragneiss sample (~10% vs 1% sps). The garnets are overall unzoned, with relatively flat major element profiles. The two samples are, however, different from one another. CA22-2A-2 has slightly higher almandine, grossular, and spessartine contents and a significantly lower proportion of pyrope (~15% difference). For the purposes of QuiG, this variation is not meaningful. Figure 23 shows that isomekes calculated using the separate compositions of CA22-2A-2 and DV22-7 produce overlapping results with an isomeke calculated using an average of the two. The average quartzite composition is thus taken to be 49% almandine, 28% pyrope, 13% spessartine, and 11% grossular, which renormalizes without spessartine to 57% almandine, 31% pyrope, and 12% grossular.

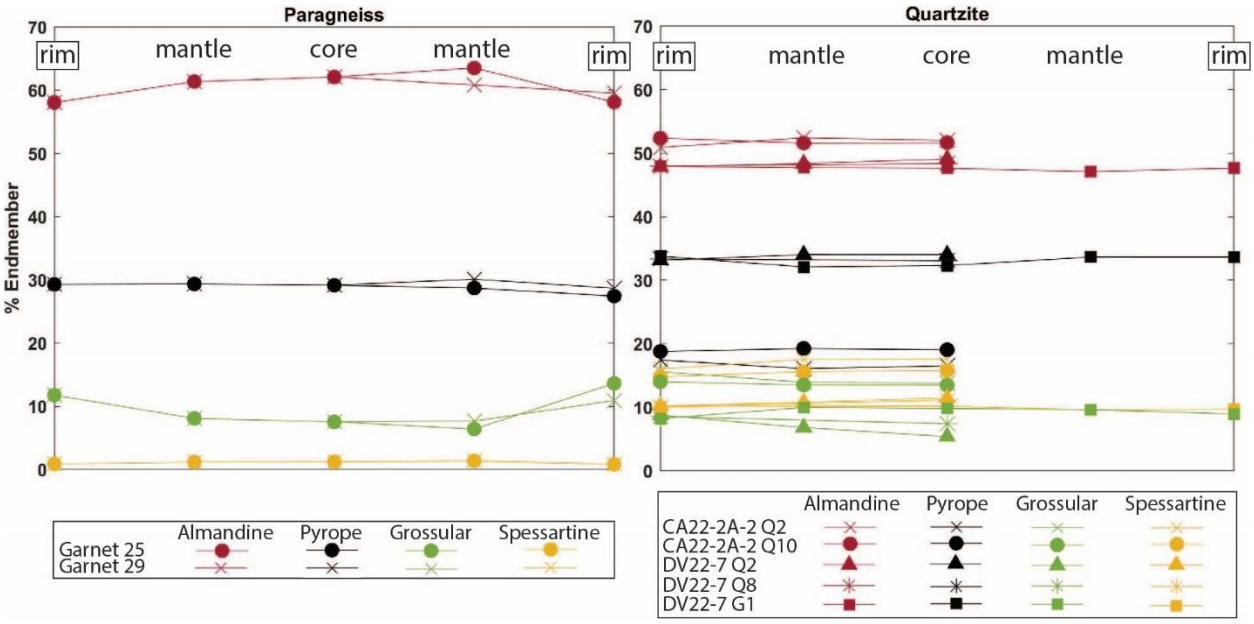


Figure 22. WDS traverses of paragneiss sample DV22-4B and the quartzite samples CA22-2A-2 and DV22-7, with relative locations within garnet (rim/mantle/core).

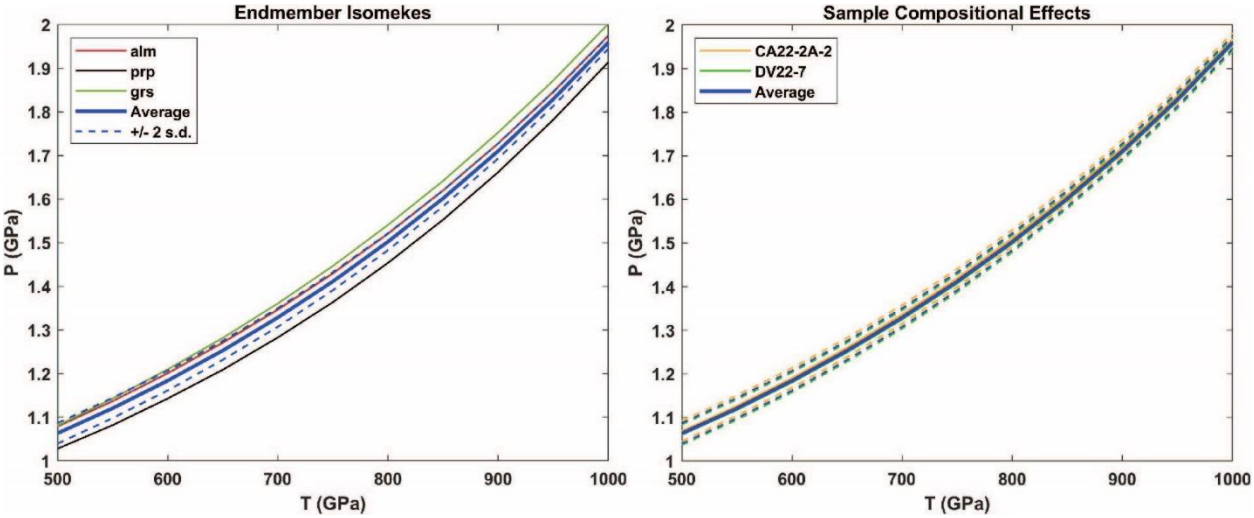


Figure 23. CA22-2A-2 isomekes. ***a.*** *Left chart shows isomekes for the individual garnet endmembers and for the weighted average calculated using the general quartzite composition (see text). The difference between endmember isomekes is <0.1 GPa.* ***b****. Right chart shows the effect of variation in composition between quartzite samples. Weighted isomekes for CA22-2A-2 (with their ± 2 sigma uncertainty) are plotted using the composition of CA22-2A-2, the composition of DV22-7, and the average of the two (same as the chart on the left). The three sets of isomekes overlap within uncertainty. Mineral abbreviations are after Whitney and Evans (2010).*

Garnets from the mafic amphibolite have an average composition of 49% almandine, 36% grossular, 11% pyrope, and 4% spessartine, which renormalizes without spessartine to 51% almandine, 37% grossular, and 12% pyrope. The mafic garnets have a relatively higher proportion of grossular and lower proportion of pyrope than the paragneiss and quartzite garnets. Garnets within a given mafic sample are very similar to one another (Figure 24). CA16-01 shows slight oscillatory zoning, with a decrease in almandine and increase in grossular in the garnet mantles that then reverses in the rims. This is not observed in the spessartine content of CA16-01, which decreases gradually and continuously from core to rim. DV16-03B does not show this oscillation and records only a gentle increase of almandine and decrease of grossular in the rims. The variation within garnets and between samples is again not significant enough to cause variation in the

QuiG results (see Figure 23). These four mafic garnets are some of the largest observed in the coherent amphibolite, with radii between 1400 and 2400 μm.

The mafic garnet WDS traverses correspond with zoning in the X-ray maps in Appendix A.1. Those maps show that the garnets in DV16-03B experienced normal concentric growth zoning. The garnets in CA16-01, however, both record a dissolution event evidenced by irregular and patchy zonation in their mantles (Appendix A.1). Dissolution in CA16-01 indicates that multi-stage garnet growth possibly occurred in the coherent amphibolite, but it will not affect the QuiG results because no quartz inclusions were measured in CA16-01. The impacts of a multi-stage growth history were avoided for the other samples by measuring inclusions from garnet cores, mantles, and rims.

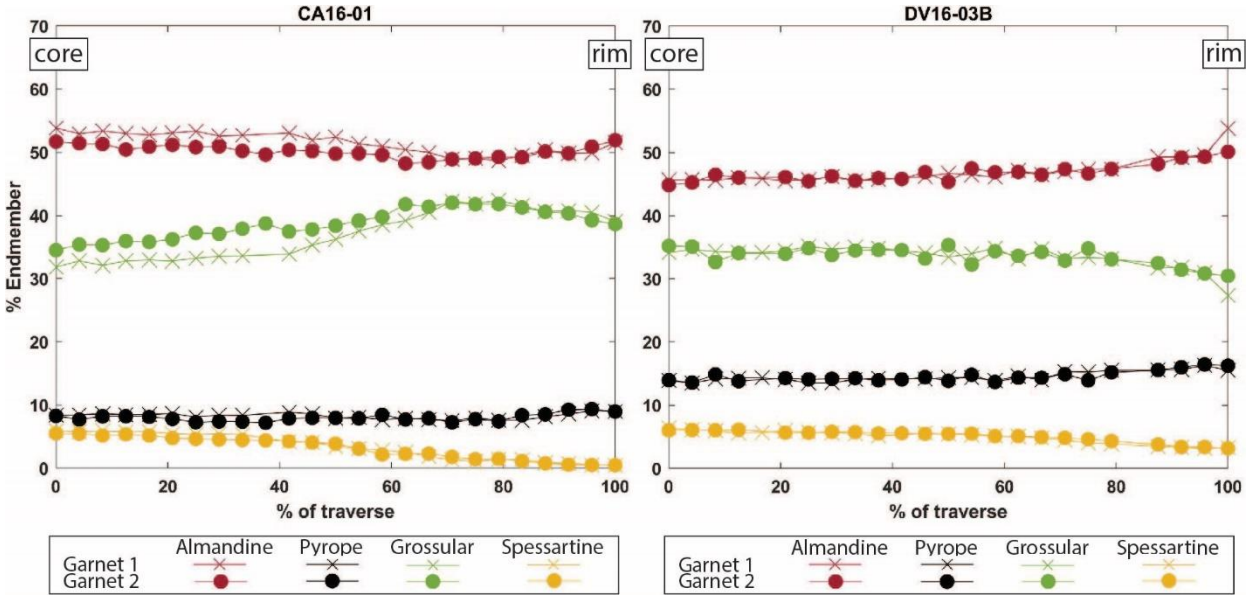


Figure 24. Core-to-rim traverses of garnets in the mafic samples CA16-01 and DV16-03B. Because the garnets are different sizes (see Appendix A1), each measurement's distance from the core was renormalized as a percentage of the traverse.

Quartz-in-garnet Calculations

The availability of usable quartz inclusions is somewhat limited in the rocks of the coherent amphibolite. The mafic amphibolites in particular do not contain abundant quartz inclusions, while garnets in the paragneiss are often heavily weathered and/or filled with dense clouds of inclusions. Nonetheless, four or more inclusions met the criteria for QuiG barometry in 6 samples, 2 inclusions were measured in DV22-12, and a single quartz inclusion was measured in DV16-03B. They were sampled from all garnet zones (e.g., core, mantle, or rim; see Appendix A.2). Inclusions were generally sub-rounded and located between 15 μm and ~40 μm depth within the sample (Figure 25). Measured peak positions for all the analyses, including the Herkimer standard, are reported in Appendix Table A.2. Calculated strains and stress are reported in Table A.3. The maximum uncertainties in the Raman peak positions propagated to uncertainties (1σ) of 0.27 cm^{-1}, 0.18 cm^{-1}, and 0.24 cm^{-1} for the 128 cm^{-1}, 206 cm^{-1}, and 464 cm^{-1} peak shifts, respectively.

For most samples, the residual inclusion pressures (P_{incs}) were classified as a single population by Peakfit Explorer. The only outliers were inclusions with lower P_{incs} than the main population; these were excluded from the calculation of sample P_{incs} (Figure 26 and Appendix A.2). Weighted averages were calculated using IsoplotR. Average P_{incs} for the seven coherent amphibolite samples range from 0.348 to 0.408 GPa, with 2σ uncertainties no greater than 23%, and most less than 10% (Table 1). The higher uncertainties are in the mafic amphibolites. A14-50C is a garnet amphibolite block in mélange that recorded a P_{inc} of 0.346, which is in agreement with the P_{incs} of the five blocks in mélange that were originally reported in Harvey et al. (2021a) and are

recalculated here. A14-50C was selected for analysis because it has the lowest reported zirconium-in-rutile concentration for a block in the amphibolite mélange (Penniston-Dorland et al., 2018).

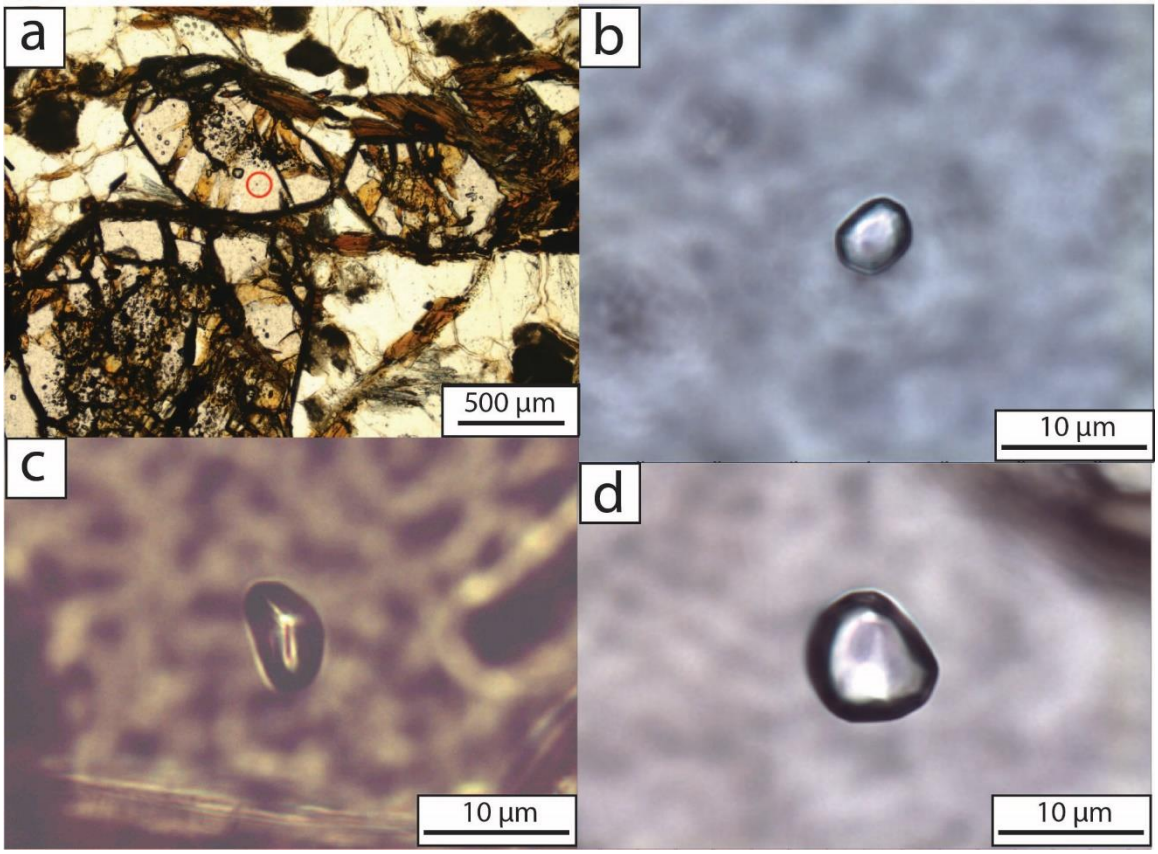


Figure 25. Representative QuiG inclusions. (b-d) taken using 100x objective on Raman spectroscope using PPL. ***a****. Garnet 27 in paragneiss DV22-4B. Red circle indicates the location of the inclusion in (b).* ***b****. Quartz #1 in Garnet 27.* ***c****. Inclusion in Garnet 31 in mafic amphibolite CA22-3.* ***d****. Q10 in quartzite CA22-2A-2.*

Table 1. Average residual pressures of quartz inclusions in garnet from the coherent amphibolite and amphibolite mélange, with the number of analyzed inclusions.

COHERENT AMPHIBOLITE			
Sample	**P_{inc} (GPa)**	**2σ (GPa)**	**n=**
Paragneiss			
DV16-04B	0.353	0.022	5
DV22-4B	0.408	0.015	7
Quartzite			
CA22-2A-2	0.391	0.014	9
DV22-7	0.373	0.020	4

DV22-12	0.423	0.028	2
Mafic Amphibolite			
CA22-3	0.405	0.052	4
DV16-03B	0.348	0.080	1
BLOCKS IN MÉLANGE			
A14-50C	0.346	0.014	7
A15-07A[a]	0.339	0.023	6
A15-21A[a]	0.386	0.025	8
A15-22[a]	0.323	0.008	18
A15-01A[a]	0.346	0.029	9
E2718C[a]	0.376	0.028	7

[a] Recalculated from Harvey et al. (2021a).

Average P_{incs} were used to calculate isomekes for each sample, weighted by the appropriate lithology's average garnet composition. These are shown along with isomekes for individual quartz inclusions in Figure 26. Isomekes at 650 °C fall mostly between 1.15 and 1.25 GPa. Uncertainties in the P_{incs} generally propagate to pressure ranges of around 0.05 GPa, with the exception of DV16-03B and CA22, which range 0.25 and ~0.15 GPa, respectively.

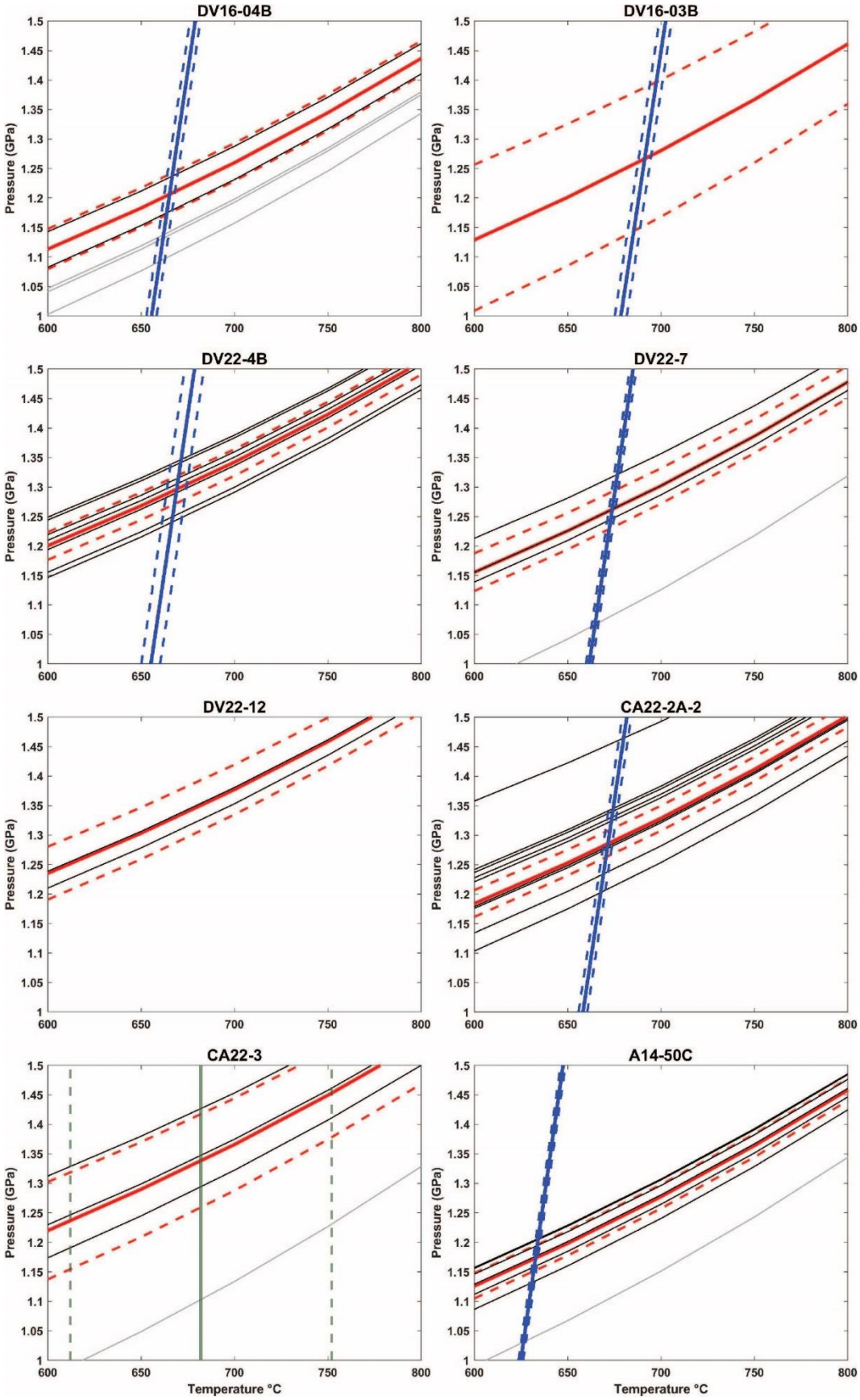

DV16-04B
DV16-03B
DV22-4B
DV22-7
DV22-12
CA22-2A-2
CA22-3
A14-50C
Pressure (GPa)
Temperature °C
1
1.05
1.1
1.15
1.2
1.25
1.3
1.35
1.4
1.45
1.5
600
650
700
750
800

Figure 26. Average isomekes (solid red) with ± 2 standard deviations (dashed red lines). Isomekes for individual quartz inclusions are black if they were included in the calculation of the average isomeke and gray if they were excluded. The near vertical blue lines are mean-max Zr-in-rutile isopleths, and the vertical green line for CA22-3 is its Ti-in-amphibole temperature. Note that only one inclusion was measured in DV16-03B and no ZiR result is available for DV22-12. Isopleths for A14-50C were calculated from Penniston-Dorland et al. (2018).

Zirconium-in-rutile Thermometry

A total of five coherent amphibolite samples were analyzed for ZiR thermometry. Rutile is expected to crystallize at peak metamorphic conditions but also along the prograde and retrograde paths, and this was evidenced by a spread of Zr concentrations across rutile grains within a given sample (Figure 27 and Table B1, in Appendix B). The distributions of Zr concentrations were fairly similar between samples, with quartzites showing slightly smaller ranges than the paragneisses (Figure 28). One exception is the mafic amphibolite DV16-03B, in which the rutile were all rimmed by titanite. It shows a wider distribution of Zr concentrations, although it also contained less rutile and so fewer grains were analyzed. Mean-max Zr concentrations ranged from 398 to 506 ppm, which resulted in temperatures ranging from 665 to 691 (Table 2). Temperatures were calculated using the reference pressures 1.3 and 1.4 GPa, as well as the sample-specific pressure determined from QuiG (where available).

A core-to-rim traverse was measured across a matrix rutile in the paragneiss sample DV16-04B (Figure 29). With the exception of a reduced Zr concentration in its core, the grain shows an otherwise uniform distribution. The lower core Zr in this grain did not affect the calculation of its grain mean-max. Where grains were large enough, a minimum of two points were placed near their centers. Localized dips in concentration should be filtered out by the mean-max processing, and this was the case for this grain (#23).

Three of the five analyzed samples contained rutile in both the rock matrix and as inclusions in garnet. Treating the matrix rutile and the rutile inclusions as separate sub-populations does not result in statistically different mean-max Zr concentrations or in metamorphic temperatures (Table 2).

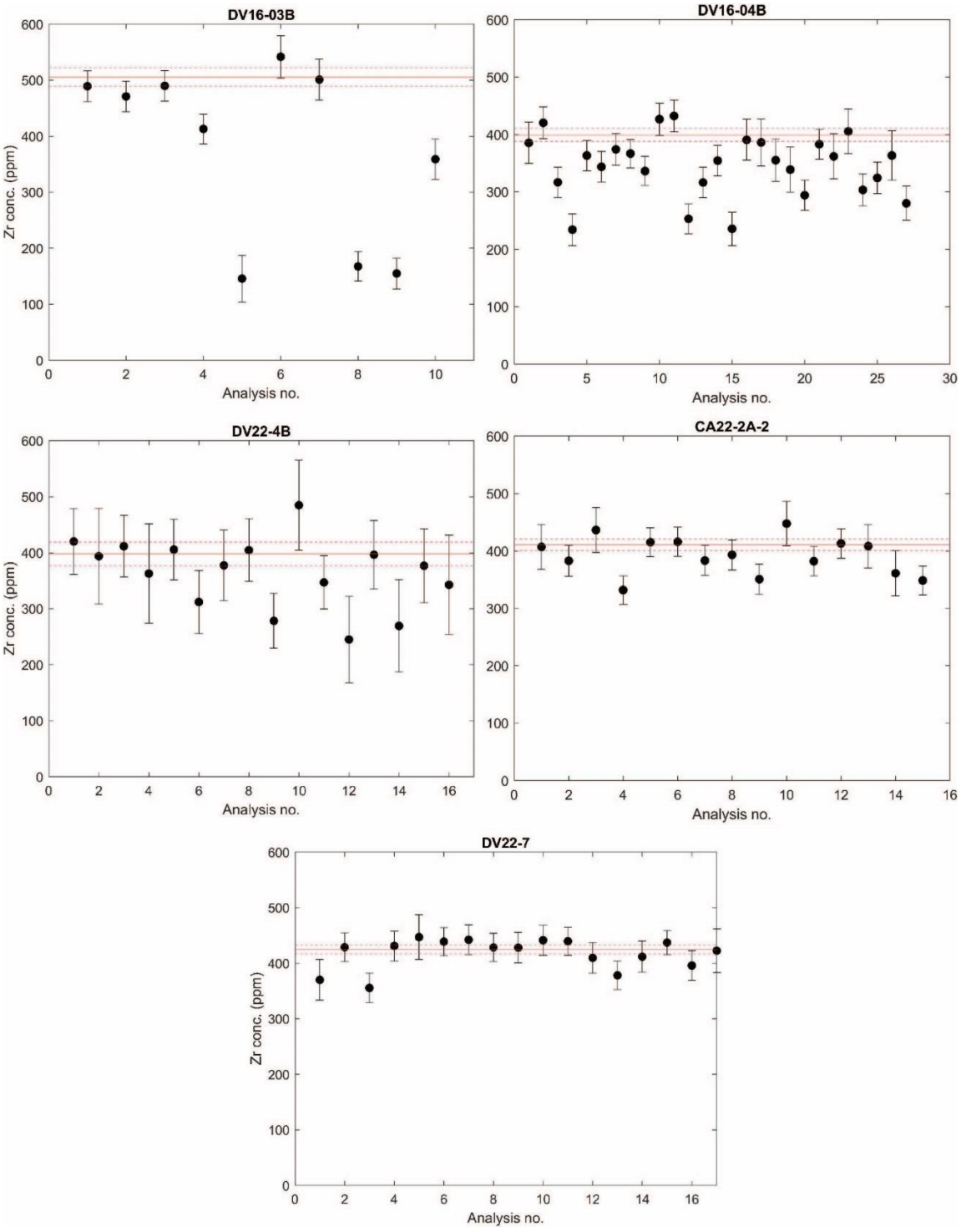


Figure 27. Mean Zr concentrations of all grains, by sample. Error bars are 2σ. The red lines indicate the sample mean-max Zr (solid) and uncertainty (2σ; dashed).

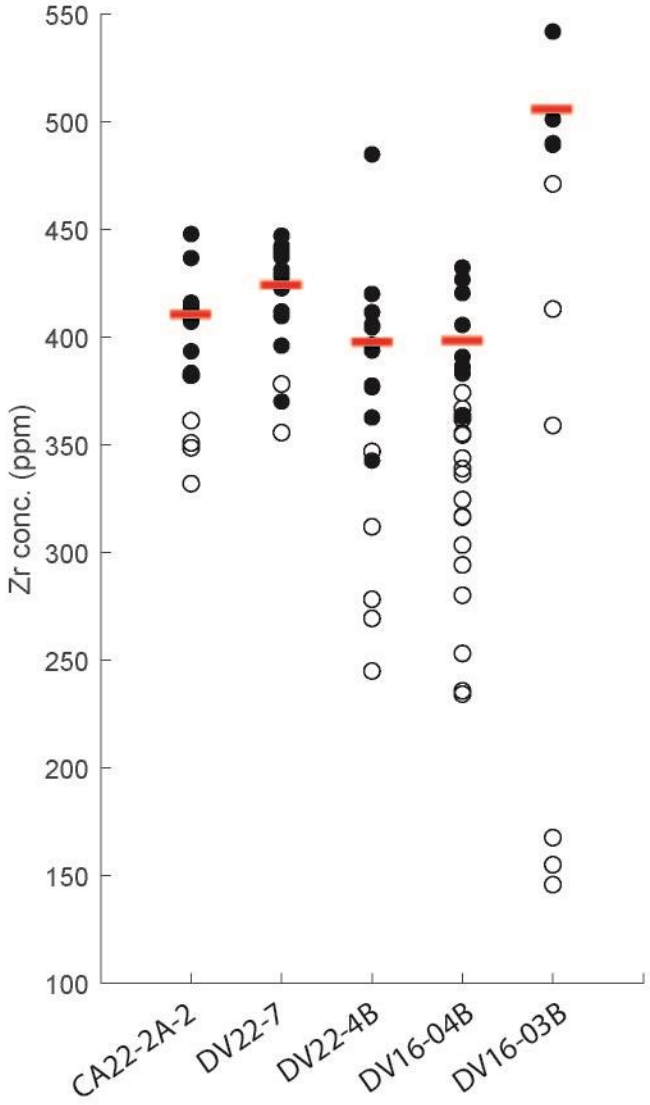


Figure 28. Grain mean Zr concentrations by sample. Grains are solid black if they were included in the mean-max population. Red bars indicate the calculated mean-max concentration.

Table 2. Mean-max Zr concentrations, broken down by location of rutile in sample.

Sample	**No. of grains analyzed**	**Mean max Zr (ppm)**	**2 s.d.**	**T (°C) @ 1.3 Gpa**	**T (°C) @ 1.4 Gpa**	**Sample P (GPa)[a]**	**T (°C)[b]**
Paragneiss							
DV16-04B	27	399	12	670 -3,+2	674 -3,+4	**1.20**	**665**
Matrix	*19*	*403*	*14*	*670 -3,+4*	*675 ± 3*	-	-
Inclusions in garnet	*8*	*396*	*19*	*669 -5, +4*	*673 -4,+5*	-	-
DV22-4B	16	398	21	669 ± 5	674 ± 5	**1.29**	**669**

Matrix	*10*	*374*	*22*	*663 -5,+6*	*668 -6,+5*	-	-
Inclusions in garnet	*6*	*409*	*34*	*672 -9,+7*	*676 ± 8*	-	-
Quartzite							
DV22-7	17	425	8	676 -2,+3	680 -1,+2	**1.26**	**674**
Matrix	*10*	*425*	*10*	*676 -3,+2*	*680 -2,+3*	-	-
Inclusions in garnet	*7*	*436*	*12*	*678 ± 3*	*683 -3,+2*	-	-
CA22-2A-2	15	411	10	672 -2,+3	677 ± 2	**1.29**	**672**
Mafic amphibolite							
DV16-03B[c,d]	10	506	16	693 ± 3	698 -4,+3	**1.27**	**691**

[a] Determined from QuiG.

[b] Calculated by finding intersection of sample isomeke with isopleth.

[c] Sample contained only matrix grains.

[d] Rutile were rimmed by titanite.

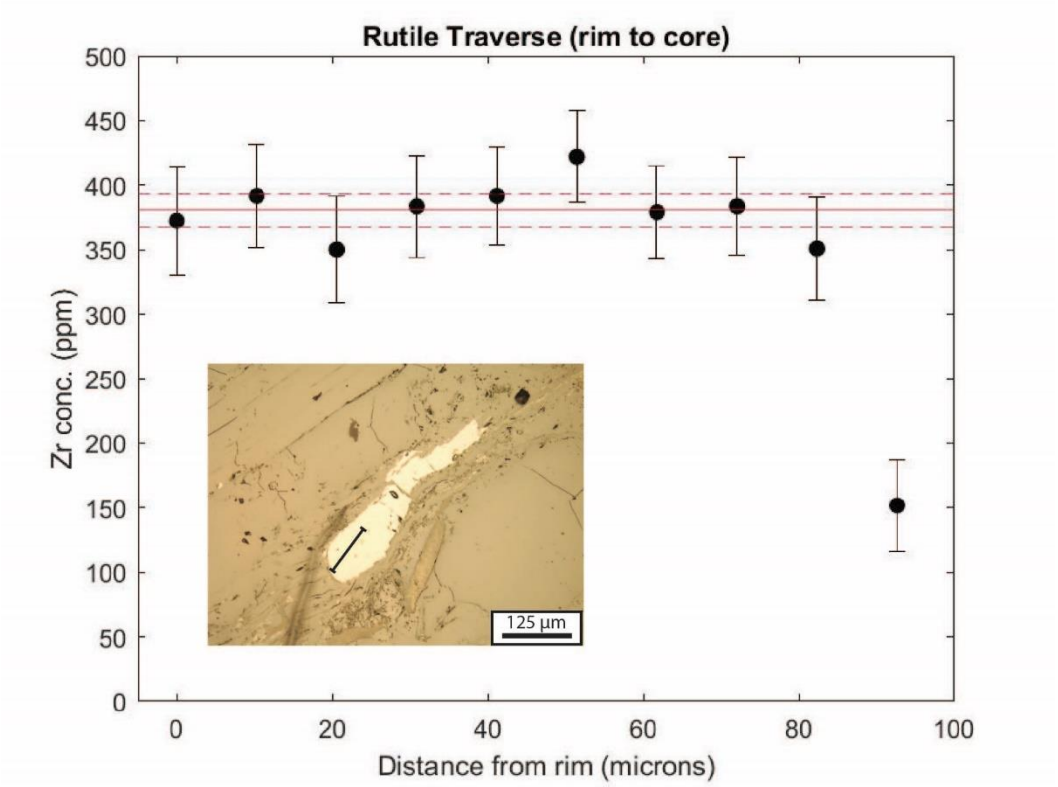


Figure 29. Zr concentrations along traverse from rim to core of matrix rutile grain in DV16-04B. Error bars are 2σ. The red lines indicate the grain mean-max Zr (solid) and uncertainty (2σ; dashed). Inset is a photomicrograph of the grain (20x, reflected light) with black bar indicating path of traverse.

Ti-in-Amphibole Thermometry

The general amphibole formula, arranged by crystallographic site, is:

$$A_{0\text{-}1}B_2C_5{}^{VI}T_8{}^{IV}O_{22}(OH,F,Cl)_2$$

Cations that commonly fill each site are Na, K, and Ca in the A site; Na, Ca, Mg, Mn, Fe^{2+}, and Fe^{3+} in the B site; Mg, Mn, Fe^{2+}, Fe^{3+}, Zn, Ni, Cr, Ti, and Al in the C site; and Ti, Al, and Si in the tetrahedral (T) site (Ridolfi et al., 2018). The amphiboles in these samples are mostly magnesio-hornblende, with some plotting in the tremolite and tschermakite fields of the Ca-amphibole classification diagram (Figure 30). Amphibole composition changes moving up-section through the coherent amphibolite, with CA15-02B representing its base and CA22-3 near its top, close to the contact with the mélange. CA22-1 and in particular, CA22-3, contain higher proportions of the crystallographic A site cations and Al, Fe^{3+}, and Ti in the C site. Grain rims are mostly similar in composition to their cores, though rims are slightly more tschermakitic than their cores in CA22-1 and CA22-3.

The Ti content of all samples is overall low, with values ranging from below the detection limit to 0.132 apfu (Figure 31 and Appendix C). Grain cores and rims generally contain similar amounts of Ti, indicating there were no significant changes of Ti in amphibole during metamorphism. A possible exception is CA22-3, which has slightly lower Ti in the rims and a wider overall distribution of Ti content. CA15-02B and CA15-03B, which were collected from the lower half of the coherent amphibolite, have approximately equivalent Ti in amphibole contents. CA22-1 and CA22-3, which were taken from the upper coherent amphibolite, show increasing Ti in amphibole as the contact with the mélange is approached. The mean-max Ti values range from 0.022 to 0.102 apfu (Table 3).

These Ti concentrations are mostly below the recommended range of 0.1 to 0.5 apfu for the Liao et al. (2021) calibration, so the resulting temperatures should be regarded as exploratory. Temperatures calculated using the Liao et al. (2021) thermometer range from 482 to 682 °C with 2σ uncertainties of ±70 °C. The temperatures calculated for the lower samples CA15-02B and CA15-03B overlap within uncertainty, as do those for upper samples CA22-1 and CA22-3.

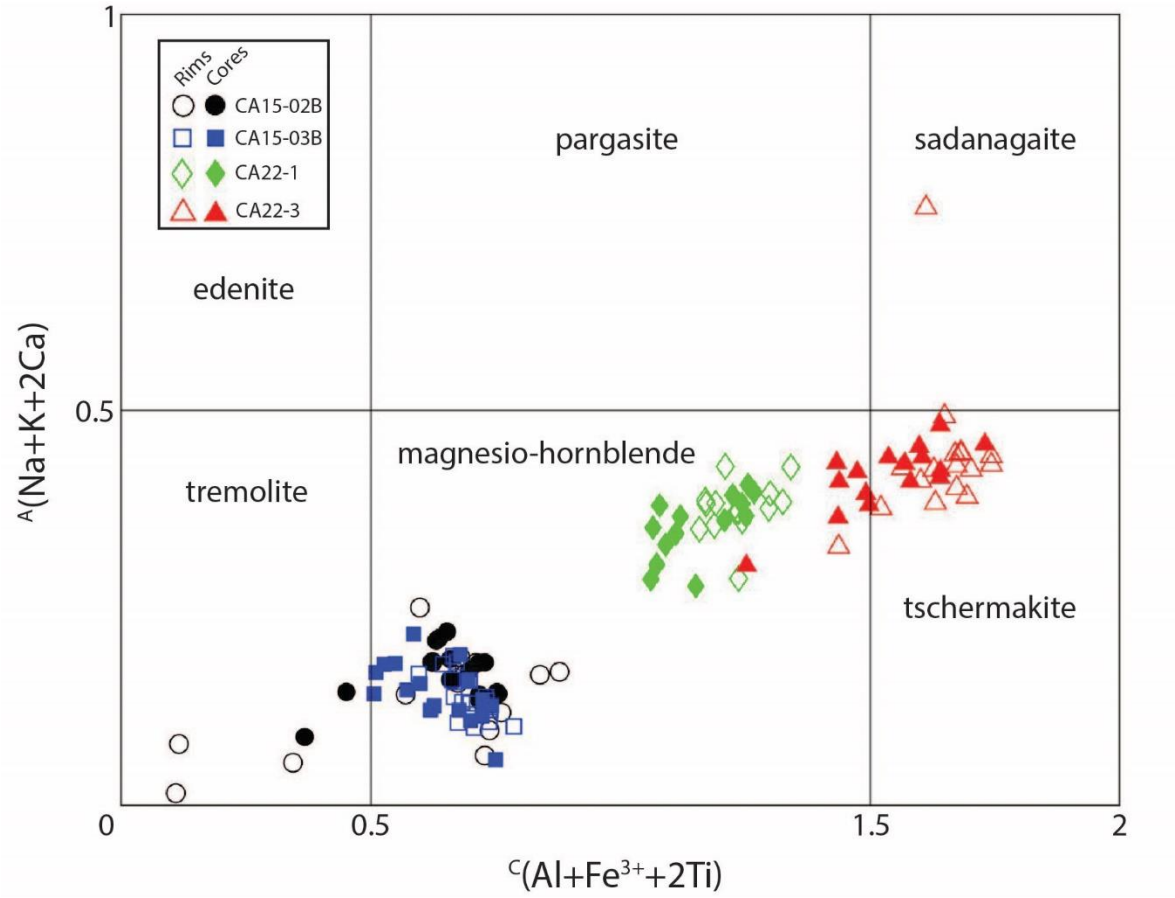


Figure 30. Calcium amphibole classification diagram after Hawthorne et al. (2012). Axes represent A and C site cations, with units of atoms per formula unit (apfu).

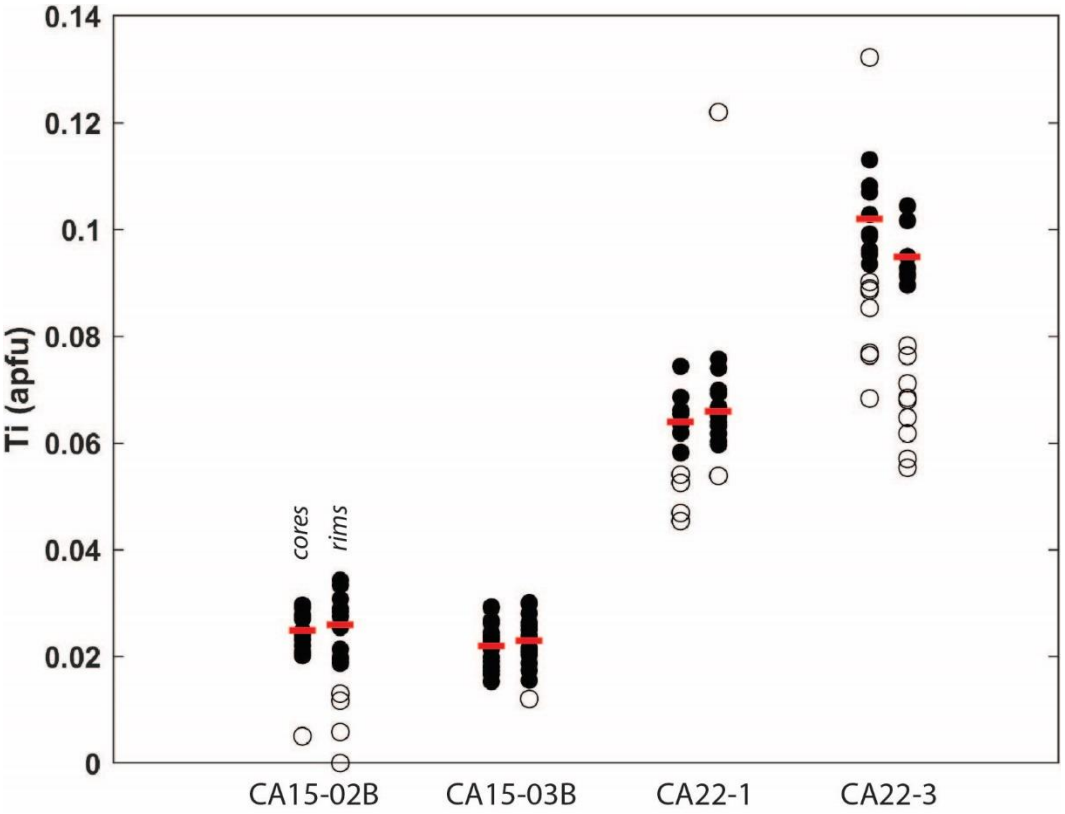


Figure 31. Ti content (apfu) of amphiboles in four mafic amphibolite samples, with grain cores on the left and rims on the right. Analyses are black if they were included in the calculation of the mean-max Ti, which is denoted by the red bars. From left to right, samples move upward through the coherent amphibolite.

Table 3. Ti-in-amphibole compositions and resulting metamorphic temperatures, calculated using the Liao et al. (2021) calibration. The temperature uncertainty is ± 2σ.

Sample	**Position in grain**	**Mean-max Ti (apfu)**	**2 s.d.**	**T (± 70 °C)**
CA15-02B *(n=16)*	Cores	0.025	0.002	496
	Rims	0.026	0.002	498
CA15-03B *(n=17)*	Cores	0.022	0.002	482
	Rims	0.023	0.002	487
CA22-1 *(n=14)*	Cores	0.064	0.003	612
	Rims	0.066	0.003	615
CA22-3 *(n=17)*	Cores	0.102	0.003	682
	Rims	0.095	0.003	671

Discussion

A Snapshot of the Downgoing Slab

Primary Lithologies

The work presented here offers an expansive portrait of a downgoing oceanic slab at amphibolite facies conditions. Platt (1976) suggested that the mafic coherent amphibolite, which he calls hornblende schist, is consistent with a gabbroic protolith. There is variation across the mafic amphibolite in both overall color (from green to black in hand sample), amphibole color and chemistry (see Figure 30), and in the modal proportion of amphibole, epidote group minerals, and plagioclase. These variations could be explained either by changes in metamorphic grade or by changes in bulk rock chemistry. Platt (1976) interpreted the variation as being consistent with a cumulate origin for the gabbro, in which bulk rock changes occurred over time from a single magmatic source or originated from multiple magmatic sources. Subtle differences in color and modal proportions, however, were observed between traverses at approximately the same depth in the coherent amphibolite. Rocks in the lower Rattlesnake traverse, for example, appear greener and contain a higher proportion of epidote than equivalent rocks on the CA traverse. Along strike variations are possibly more likely to arise from a cumulate origin for the coherent amphibolite, while variations from the bottom to the top of the coherent amphibolite may still reflect subtle changes in bulk chemistry while being dominantly controlled by a thermal gradient (discussed below).

The paragneiss, which rests structurally on top of the mafic amphibolite, contains some mica phases and abundant quartz and plagioclase, usually arranged in layers that may be

original lithologic bedding (Platt, 1976). The quartz and plagioclase likely reflect a significant component of near-shore clastic sediment input, likely shed from the nearby continent (Grove et al., 2008). Within the paragneiss are several lithologies that occur both as isolated layers and in contact with one another. The garnet quartzites were probably layers of siliceous ooze on the seafloor and reflect primary deposition. Abrajevitch (2020) proposes a diagenetic origin for chert beds in which silica dissolves and segregates into alternating layers, but the quartzite layers in the paragneiss do not alternate regularly and where they do occur in proximity to one another, are usually separated by several meters. The chlorite schists, on the other hand, are more likely to be a metasomatic rock, rather than a product of sedimentary deposition. They are reminiscent of amphibolite mélange matrix in terms of mineralogy and texture, but they typically occur in discrete layers and possibly represent a fluid pathway that channelized along bedding planes. The layers of mafic amphibolite found within the paragneiss are somewhat enigmatic. They could be derived from surficial pyroclastic deposits or lava flows or from intrusive sills (Platt, 1976).

The juxtaposition of these lithologies within the paragneiss paints a picture of a dynamic depositional environment and it is remarkable that these features are preserved in the coherent amphibolite. If the mafic layers are volcanogenic, rather than intrusive, then their association with garnet quartzites may suggest a relationship between pyroclastic or basaltic inputs and blooms of radiolarian productivity. While isolated layers of quartzite do occur within paragneiss, the majority of quartzites, mafic layers, and chlorite schists occur in conjunction with at least one of the other lithologies. This raises the possibility that the less permeable quartzite and mafic layers became preferred metasomatic fluid

pathways during subduction, locally concentrating the fluids expelled from mineral dehydration reactions and leading to the formation of the chlorite schists. These impermeable layers were not “traps” preventing the vertical circulation of fluids, because chlorite schists occur both above and below them, but perhaps just local boundaries to generalized fluid flow. In this scenario, the chlorite schist likely represents metasomatized mafic material.

There is evidence for pervasive fluid flow in the coherent amphibolite. Plagioclase is almost ubiquitously saussuritized to some degree throughout the entire coherent amphibolite. Saussurite is a hydrothermal alteration product in which the anorthite component of plagioclase is altered to epidote group minerals and the remaining plagioclase is converted to albite. Saussuritization is a metamorphic process, not weathering or alteration, and most notably, the reaction requires the input of water and occurs above pressures of ~0.8 GPa (Franz and Liebscher, 2004). The degree of plagioclase saussuritization varies with depth in the coherent amphibolite. Its effects on plagioclase are minimal at the base of the coherent amphibolite, with relatively unclouded grains and polysynthetic twinning still visible in some samples. At intermediate depths in the coherent amphibolite, incipient saussuritization can be observed in the form of euhedral, acicular grains of epidote group minerals radiating within plagioclase. The epidote minerals are often large enough to display characteristic epidote interference colors in cross polarized light, including anomalous blue colors. At the top of the coherent amphibolite, particularly in the paragneiss, plagioclase has been completely saussuritized. Remnant plagioclase can be identified only by its interstitial grain shapes, as it has been completely converted to dark, opaque masses of

indistinguishable fine-grained crystals (see Figure 14). This depth-dependent saussuritization suggests that the prevalence of hydrous fluids increased as the contact with the mélange was approached.

In addition to its role in saussuritization, epidote serves as an important recorder of changes in the mafic amphibolite during metamorphism. It often occurs as euhedral grains that display growth zoning in cross polarized light, which is a common feature of epidote and can occur due to changes in pressure-temperature conditions, miscibility gaps within the epidote group mineral phases, and changes in oxygen fugacity (Franz and Liebscher, 2004). Fir-tree sector zoning (see Figure 13d), however, is more enigmatic and has not previously been reported in epidote. Sector zoning in general is when compositional zonation in minerals is defined by distinct crystal faces, rather than "tree ring-like" growth of concentric zones (Philpotts and Ague, 2022). Raven and Dickson (1989) argue that fir-tree zoning in calcite is indicative of rapid switches in relative growth rate between two coexisting crystallographic forms. These rapid alternations could be caused by pulsed changes in fluid chemistry (Fe fluctuations, in the case of calcite cements [Raven and Dickson, 1989]). Li isotopic evidence for rapid and pulsed fluid flow has been recorded at other paleosubduction localities, including Monviso (Hoover et al., 2022a), New Caledonia (Taetz et al., 2018), Tianshan (John et al., 2012), and, in northern California, the Franciscan (Penniston-Dorland et al., 2010). Saussurite indicates that fluids were present in the coherent amphibolite at pressures at least above 0.8 GPa (Franz and Liebscher, 2004), so likely coinciding or overlapping with peak metamorphism; this is consistent with findings that fluids are present at these depths in subduction zones (Condit and French, 2022; Condit et al., 2020). Furthermore, the

epidote fir-tree zoning is most pronounced in WB22-6, a sample that also contains a microscopic shear zone (see Figure 20). This shear zone could have acted as a conduit for episodic fluid flow, providing pulsed changes in fluid chemistry that allowed for one crystallographic form to dominate over another in the growing epidote crystals. Only small changes in the Fe-Al content of epidote are required to produce changes in birefringence (Franz and Liebscher, 2004), so fir-tree zoning could result from only minor differences in the chemistry of fluid inputs.

Structural History

The dynamic evolution of the coherent amphibolite is also evidenced by the deformational structures observed throughout. On the km-scale, the coherent amphibolite appears to be involved in a synmetamorphic plunging anticlinal fold, the axis of which passes roughly through the middle of the mafic amphibolite and, according to Platt (1976), plunges to the northeast. This may cause the change in dip direction between the Dawn Valley, which dips W-E, and the other traverses, which dip SW-NE. At the meter-scale, outcrops of relatively undeformed rock with planar foliations are often juxtaposed against rocks that have been folded (see Figure 7 and Figure 8a). This occurs in both the mafic amphibolite and in the paragneiss, particularly in the western half of the coherent amphibolite. The frequency and intensity of local folding, broadly speaking, increase moving up section through the unit. Tight isoclinal folds were observed in the upper Dawn Valley in both mafic and paragneiss layers. At the top of that traverse, near the contact with the mélange, fold axes became erratically oriented, at times plunging vertically and at times sub-horizontally.

The upper part of the coherent amphibolite varies from east to west in terms of its outcrop-scale folds and its lithology. The folding at the top of the coherent amphibolite is not observed in its eastern half. At Cottonwood Canyon, the mafic amphibolite directly contacts amphibolite mélange with no intervening paragneiss. There is also no pattern of intense folding, only a change in dip that takes place over several meters (see Figure 10). There are a few possible explanations for the irregular distribution of paragneiss in the coherent amphibolite. First, it is possible that sedimentation prior to subduction was uneven. In this scenario, the western half of the coherent amphibolite may have been a small basin where sediment was collected and later metamorphosed into paragneiss. This is potentially supported by the way the paragneiss is distributed across the coherent amphibolite (see Figure 5), with a thick package in Dawn Valley that appears to pinch out to the east, around the Sheep Chute area. Along strike variations in sediment input have been documented for some modern subduction zones, including the Hikurangi subduction zone in New Zealand (Barnes et al., 2020) and the Nankai trough in Japan (Tilley et al., 2021). The scale of those variations is somewhat larger (<10 km; Tilley et al., 2021) than observed in the coherent amphibolite (<2.5 km), however, and a complete absence of sediment is observed only the flanks of a seamount (Barnes et al., 2020). A second possible explanation is that the asymmetric distribution of paragneiss resulted from along strike heterogeneities in tectonic erosion during subduction. As the direct interface between the two plates, the mélange would have been affected by asperities and heterogeneities in the overriding and downgoing plates. The coherent amphibolite, which at one time was attached to the downgoing plate, may also have been variably affected by these features (Agard et al., 2018). In this scenario, the uneven corrugations of the

downgoing and overriding plates may have scraped only portions of the sediment away while leaving sediment behind elsewhere (Kirkpatrick et al., 2020). This has been proposed to explain the distribution of great earthquakes in the modern Northern Manila Trench (Tan et al., 2022). The compilation of global subducted sediment thicknesses by Seno (2017) also supports the observation that sediment thickness varies along strike, although nowhere in their dataset does the sediment thickness reach zero. These processes are also not mutually exclusive, and both uneven sediment distribution and variable slab scraping could have affected the downgoing plate.

A final possible explanation for the distribution of paragneiss is suggested by the field observations. At Cottonwood Canyon, the difference in orientation between the mafic coherent amphibolite and the amphibolite mélange shows that the contact between them is discordant. This suggests that the current boundary cuts obliquely across the coherent amphibolite, exposing paragneiss in the west and truncating directly against mafic amphibolite in the east. The exact timing of this juxtaposition is not well constrained, but the mélange material inside the Cottonwood Canyon fault (Grabiec, 2017) indicates that mélange was still active and deforming at the same time as the coherent amphibolite. The oblique coherent-mélange contact therefore likely reflects conditions at the time of the coherent amphibolite's underplating. While there is little field and geochemical evidence to suggest that sediments played an important role in amphibolite mélange formation (Bebout and Barton, 2002), the absence of paragneiss in the eastern half of the coherent amphibolite suggests that it has either been removed or incorporated into the mélange. It is difficult to constrain the nature of the coherent-mélange boundary without other field exposures, but the uneven loss of paragneiss may reflect along-strike variations in the

thickness of the mélange zone or a gradual, oblique shaving of the coherent amphibolite prior to its underplating.

The presence of a large serpentinite body within the Dawn Valley is enigmatic. Platt (1976) described it as a shallow ellipsoidal body and the observations made here support that interpretation. Its contact with the mafic amphibolite, visible at its southwestern edge, is undisrupted and parallel with the foliation in the amphibolite. Its contacts with other units are difficult to find in the field, so it is difficult to establish its exact relationship with the surrounding rocks, but its ultramafic character suggests that it is likely related to the amphibolite mélange, which also contains serpentinite bodies (Bebout and Barton, 2002). Lenses of serpentinite at the base of paleosubduction nappes have also been observed in the Condrey Mountain Schist in the Klamath Mountains of northern California (Tewksbury-Christle et al., 2021). Those authors argue that the serpentinites were likely entrained in the coherent slices during shallow tectonic erosion of the downgoing plate. This is a possibility for the Dawn Valley serpentinite, but without further study its exact origins remain unknown.

At its base, the coherent amphibolite is separated from the epidote blueschist by the Ollas thrust. Harvey et al. (2021a) reported temperatures between 576 and 600 °C for blocks and matrix material inside the Ollas thrust shear zone, indicating that it formed near peak metamorphic conditions. This finding is supported by the mineral assemblage in the grayschist sample WB22-1. Found at the base of the Rattlesnake traverse, near the inferred boundary of the Ollas thrust, it contains garnet and rutile that have since retrograded to lower grade minerals. The heavily dissolving mineral grain boundaries and prevalence of graphite, which is not observed elsewhere in the coherent amphibolite,

suggest that this rock was a mafic amphibolite that experienced metasomatic fluid interactions at amphibolite grade conditions. The Ollas thrust shear zone could have been the conduit for external fluid infiltration that locally allowed for the growth of minerals that do not appear again until several hundred meters higher in the coherent amphibolite.

Proto-mélanges

Some of the most striking observations in the coherent amphibolite are of previously unreported outcrops with similar features to the amphibolite mélange. In the lower Dawn Valley, a chaotically folded region of weak, matrix-like material hosts several pods of talc-actinolite rock intercalated with mafic amphibolite and quartzite lenses. The presence of talc-actinolite, which may have more of an ultramafic affinity, is observed nowhere else in the coherent amphibolite. This region of weak, heavily deformed material is tens of meters thick and is bounded at its top and bottom by folded chlorite schists and paragneiss. Furthermore, in the upper Dawn Valley side gully outcrop is an unusual layer of weak chlorite schist that wraps around blocks of undeformed garnet amphibolite (DV20-04). The schists in the side gully were identified as predominantly chlorite in the field, but sample DV22-13 was later found to be talc schist (see Figure 3). It is possible that other layers in the side gully, including the one hosting the garnet amphibolite blocks, are actually talc schists. Regardless of their mineralogy, the schists in the side gully and in the talc-actinolite pod outcrop are strongly reminiscent of mélange because of their block-in-matrix nature.

Sample DV20-04 resembles garnet amphibolite blocks found throughout the amphibolite mélange. In hand sample, it consists almost entirely of mm-scale garnet grains with intervening black amphibole. In thin section, it looks entirely different from all other

samples of the coherent amphibolite. Its garnets follow an atoll growth pattern, in which their mantles are disrupted by continuous rings of inclusions (see Figure 17). There is no agreed upon mechanism for atoll garnet formation and in fact there may be multiple causes of atoll growth, but hydrous fluids are commonly invoked as an explanation. Rapid temperature increase accompanied by a pulse of water from mineral breakdown could temporarily spike the mineral nucleation rate (Godet et al., 2022), or widespread garnet fracturing from a deformational event could allow for infiltration by fluids and mineral replacement (Massonne and Li, 2022). The garnets in DV20-04 are also distinct for containing abundant rutile exsolution needles (see Figure 18). Ti in garnet increases with increasing pressure and temperature, and exsolution of rutile in garnet has been observed only in rocks that have experienced extreme PT conditions, such as ultrahigh-pressure (UHP) rocks, mantle xenoliths, and ultrahigh-temperature (UHT) granulites (Ague and Eckert, 2012). Overall, DV20-04 is dissimilar from other coherent mafic amphibolite and instead strongly resembles blocks in the amphibolite mélange, which also contain atoll garnets and abundant rutile exsolution needles. These differences could indicate that DV20-04 is chemically different from the rest of the coherent amphibolite, or, given its block-in-matrix morphology in the chlorite schist, could suggest that DV20-04 is a mafic block that has been transported to its present location via mélange type flow of blocks within the surrounding schist.

The presence of DV20-04 raises some important questions: what is its relationship to the rest of the coherent amphibolite, and what implications does it have for mélange formation broadly? Its distinctly high Ti content, inferred from the rutile exsolution in garnet and its overall proportion of matrix rutile, implies that it has either a different bulk

rock composition or it experienced a different metamorphic history than the surrounding rocks. Minor rutile exsolution in garnet was also observed in DV20-05A, a sample from a foliated mafic layer just above where DV20-04 was sampled, but the needles are not nearly as ubiquitous as they are in DV20-04. More tellingly, the major Ti-phase in DV20-05A is titanite, not rutile. Those two samples can also be contrasted in their amphibole appearance. In thin section, the amphiboles in DV20-04 are granoblastic polygonal and relatively undeformed. In DV20-05A, the amphiboles are elongate and strongly foliated. These observations suggest that DV20-04 may have experienced a separate metamorphic history from the surrounding coherent amphibolite.

Exotic blocks do occur in the lower grade units of the Catalina Schist, although they are significantly larger (10s of meters across) than the DV20-04 block (<0.5 m; Harvey et al., 2021a). Those exotic blocks appear to have been transported greater distances along the subduction interface by strain localization (Harvey et al., 2021a). Weaker materials such as sheet silicates are likely to preferentially accommodate strain, thus allowing for greater deformation and movement of blocks (Penniston-Dorland et al., 2018). It is reasonable to conclude, therefore, that the weak chlorite schist acted like a mélange by concentrating strain and transporting DV20-04 to its present location from farther down in the subduction zone. The same chlorite schist layer also contains DV22-12, a patch of recumbent folded quartzite that pinches out ~15 cm down-limb from its tight fold hinge. On the inside of the fold is some mafic material that resembles DV20-04. These relations suggest that not only mafic blocks but also quartzite and potentially paragneiss layers have been incorporated into this particular chlorite schist. It is unknown why exotic

blocks were not observed elsewhere in the coherent amphibolite, but this layer is also thicker than most other chlorite schists.

I propose that the chlorite schist hosting DV20-04 and DV22-12 is a “proto-mélange,” a layer of weakly deforming sheet silicates that transported small blocks of material. It parallels the main subduction interface, represented by the amphibolite mélange, but it is an order of magnitude thinner than that primary shear zone. Two important implications arise from this interpretation. First is that metasomatism to form the chlorite schist had to have preceded the strain localization that allowed for block transport. Second is that the complexity of strain localization at smaller scales is not captured by models for underplating, which typically depict a large (km-scale) shear zone that periodically steps downward when tectonic slices of the downgoing plate become mechanically coupled to the overriding plate (Agard et al., 2018). Rather than a stepped process during underplating, strain localization may instead be transient and temporary, forming one or more meter-scale proto-mélanges prior to the establishment of the next km-scale mélange zone. Whether the proto-mélange was active at the same time as the main amphibolite mélange interface is unknown, but it would seem that mélange-formation may occur on a continuum of scales. Even the micro-shear zone in WB22-6, in which small grains appear to flow around larger clasts, could be seen as a mélange antecedent at an even smaller scale. This model may offer insight into how mélanges form and grow: starting with rocks weakened by metasomatism, incorporating more of the surrounding rock as they grow, and becoming centers for strain localization and mass transport once they achieve a certain thickness.

Several lines of evidence suggest that proto-mélanges such as that seen in Dawn Valley could be related to episodic tremor and slip (ETS) phenomena. The P-T conditions of the Catalina Schist amphibolite (see discussion below) overlap with depths of ETS observations below the seismogenic zone in active subduction zones (Condit et al., 2020). The prevalence of saussuritization indicates that fluids were present in the coherent amphibolite, and cyclic high fluid pressures have been associated with ETS (e.g., Dragovic et al., 2012; Condit and French, 2022). Rheological heterogeneities have been suggested to be a source of episodic tremors in subduction zones (Behr et al., 2018), and the mafic block and quartzite in the Dawn Valley proto-mélange would represent strong rheological contrasts with the surrounding chlorite schist. Lastly, talc-bearing rocks potentially act as hosts for slow slip (French and Condit, 2019; Hoover et al., 2022b), and the presence of talc schist in the Dawn Valley proto-mélange would indicate that it could have been the site of ETS during subduction. This is significant because it suggests that ETS phenomena may occur not only along the main subduction interface, but also at depth inside of the slab, and future field investigations could look to coherent terranes for evidence of ETS.

A Thermal Gradient Across the Coherent Amphibolite

The petrographic observations and peak metamorphic temperatures presented here point to the existence of a thermal gradient across the coherent amphibolite. Amphibole composition changes moving from the base to the top of the coherent amphibolite (see Figure 30), and this is also reflected by their color in plane polarized light changing from colorless to dark green (see Figure 12). Ti in amphibole is known to increase with temperature (Liao et al., 2021), but amphiboles broadly are known to move from

actinolite to hornblende compositions with increasing metamorphic grade (Spear, 1993). A temperature gradient is also suggested by the absence of the higher-grade minerals garnet and rutile from lower sections of the coherent amphibolite (see Figure 4).

The available Zr-in-rutile and Ti-in-amphibole temperature data corroborate the mineralogical evidence (Figure 31 and Figure 32). The Zr-in-rutile temperatures for the upper reaches of the coherent amphibolite all fall between 665 and 691 °C. These are likely accurate estimates of the peak metamorphic temperatures for several reasons. First, they are based on mean-max Zr concentrations. Second, the traverse across the matrix grain in DV16-04B did not capture any evidence for diffusion of Zr. Lastly, while the closure temperature for Zr in rutile is not firmly established, a reasonable estimate is between 700-750 °C for 100 μm grains and a cooling rate of 25 °C/Ma (Dohmen et al., 2019; Cherniak et al., 2007). Perhaps most importantly, these temperatures for the coherent amphibolite are consistent with estimates from other techniques (Platt, 1976; Sorensen and Barton, 1987; Grove and Bebout, 1995).

The Ti-in-amphibole temperatures range from 482 to 682 °C, which creates a geologically unreasonable gradient of ~500 °C/km. The temperatures below 650 °C have to be considered exploratory, however, because their Ti content falls outside the recommended range of the Liao et al. (2021) thermometer. Nevertheless, the results indicate that Ti-in-amphibole increases moving up from the base of the coherent amphibolite and that this reflects the existence of a gradient in metamorphic temperatures.

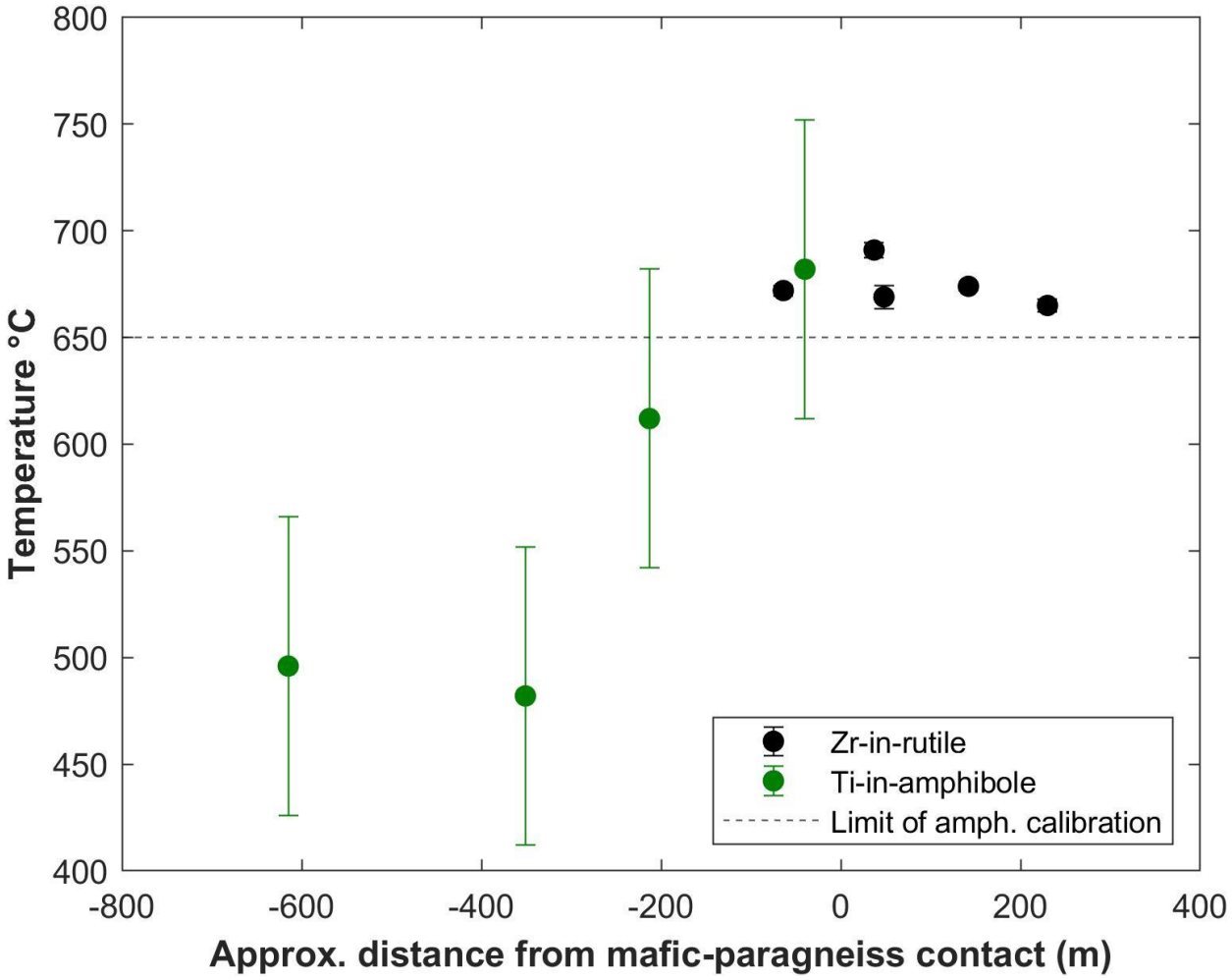


Figure 32. A thermal gradient across the coherent amphibolite. Ti-in-amphibole (green) and Zr-in-rutile (black) data are shown as a function of approximate vertical distance from the mafic-paragneiss contact (which is the only consistent benchmark across traverses). Uncertainty bars are ± 2σ and are in most cases smaller than the Zr-in-rutile markers. Ti-in-amphibole data below the horizontal dashed line are outside the calibration range of the Liao et al. (2021) thermometer. Ti-in-amphibole data are for grain cores, not rims.

Application of the trace element thermometers

The data presented here show that Zr-in-rutile is a useful thermometer for studying the coherent amphibolite. Treating the rutile as separate matrix and garnet inclusion populations produces overlapping estimates of metamorphic temperature. Rutile included in garnet presumably lock in the Zr concentration of the rock at a specific point along the P-T path, and the fact that they agree with the matrix rutile, which experienced the full

lifecycle of the rock's metamorphic history, indicates that Zr-in-rutile is a robust trace element system for estimating peak metamorphic temperatures. It also indicates that the pressure estimates from quartz-in-garnet barometry likely correspond with the peak conditions experienced by the rock.

DV16-03B, in which the rutile were rimmed by retrograde titanite, records the highest Zr-in-rutile temperature (691 ± 3.5 °C). The next highest is 674 ± 2 °C, recorded by DV22-7. It is possible that the rutile-to-titanite reaction affected the remaining rutile such that the measured Zr concentrations no longer reflect equilibrium at peak metamorphic temperatures (Lucassen et al., 2010). Profiles of rutile from the amphibolite mélange, however, show Zr concentrations that remain flat right up to their contact with titanite rims (Cruz-Uribe et al., 2014). Other studies have found that rutile with titanite/ilmenite overgrowths can record Zr concentrations that have been reset from their un-rimmed counterparts (Rehman et al., 2019; Tual et al., 2018), but these result in reduced, not increased, temperature estimates. DV16-03B records a wide spread in Zr concentrations (see Figure 28) and it is possible that the grains with lower Zr have experienced diffusional resetting, but the process of finding a mean-max Zr concentration arrived at a temperature that is slightly elevated, not reduced, from the other coherent amphibolite samples. From this we can conclude that the DV16-03B mean-max temperature estimate likely reflects peak metamorphic conditions, that its deviation from the colder samples may just be due to natural geologic variability, and that the mean-max Zr method is a useful processing tool.

The Ti-in-amphibole thermometer is relatively imprecise, but it still provides meaningful estimates of metamorphic temperature for samples that fall within the recommended Ti-

in-amphibole range of 0.1 to 0.5 apfu. CA22-3, from the upper part of the coherent amphibolite, meets this criterion and records a Ti-in-amphibole temperature that is comparable to the Zr-in-rutile temperatures for the other coherent amphibolite samples. A further confirmation of this result comes from amphibole major element compositions for four blocks in amphibolite mélange that were reported by Penniston-Dorland et al. (2018). Amphiboles in those samples with Ti contents that fall within the recommended calibration range report temperatures that overlap within one standard deviation (± 35 °C) of their Zr-in-rutile temperatures, based on geochemical data in Penniston-Dorland et al. (2018). The CA22-3 results in Figure 31 show that Ti may start to diffuse out of amphibole rims at higher temperatures, as they record a slightly lower temperature than the grain cores. Given that amphibole grain sizes are often quite large in amphibolite rocks, they are unlikely to be completely reset. So long as measurements are taken from grain cores, and those grains have sufficient Ti, then Ti-in-amphibole should give a good estimate of peak metamorphic temperatures.

Comparison with the mélange

The Zr-in-rutile temperature results, when combined with the quartz-in-garnet pressure results, indicates that the peak metamorphic conditions experienced by the coherent amphibolite broadly overlap with blocks in the amphibolite mélange (Figure 33). The blocks in mélange, originally analyzed by Harvey et al. (2021a), have been recalculated here using the most up to date equations of state for garnet (Angel et al., 2022). The recalculations lowered their previous P estimates by about 0.1 GPa. DV16-03B has higher P uncertainty than the other coherent amphibolite samples, but its isomekes were calculated on only a single quartz inclusion. Figure 33 also shows isomekes for DV22-12,

which had no available temperature estimate, and CA22-3, which only had Ti-in-amphibole temperature estimates available. The other coherent amphibolite samples have mostly overlapping P estimates, with the exception of DV16-04B, which plots separately from DV22-4B and CA22-2A-2. It is possible that the QuiG method practiced here underestimates uncertainty, but a more likely explanation is that the population of quartz inclusions in DV16-04B did not sample the peak pressures experienced by the rock, perhaps because that sample is heavily weathered and the garnets are fractured. Another possible effect on P_{incs} calculated from QuiG barometry is viscoelastic relaxation, a process by which the strain state of a rock reequilibrates at a different point on the P-T path (Zhong et al., 2020). We cannot rule out that such relaxation may have affected these rocks, but the expected deviation from a P_{inc} original value is only 10-20% (Zhong et al., 2020). Furthermore, viscoelastic relaxation is caused by tectonic-scale heating and cooling events and if it did occur, it would likely affect both the coherent amphibolite and the amphibolite mélange approximately equally. Overall, these coherent amphibolite samples represent a geothermal gradient of roughly 18 °C/km, which is higher than that predicted by most models of subduction zone thermal structure (Gerya et al., 2002; Syracuse et al., 2010) and higher than that recorded by most other paleosubduction terranes (Penniston-Dorland et al., 2015), but consistent with estimates for the Catalina amphibolite mélange (Harvey et al., 2021a; Penniston-Dorland et al., 2018).

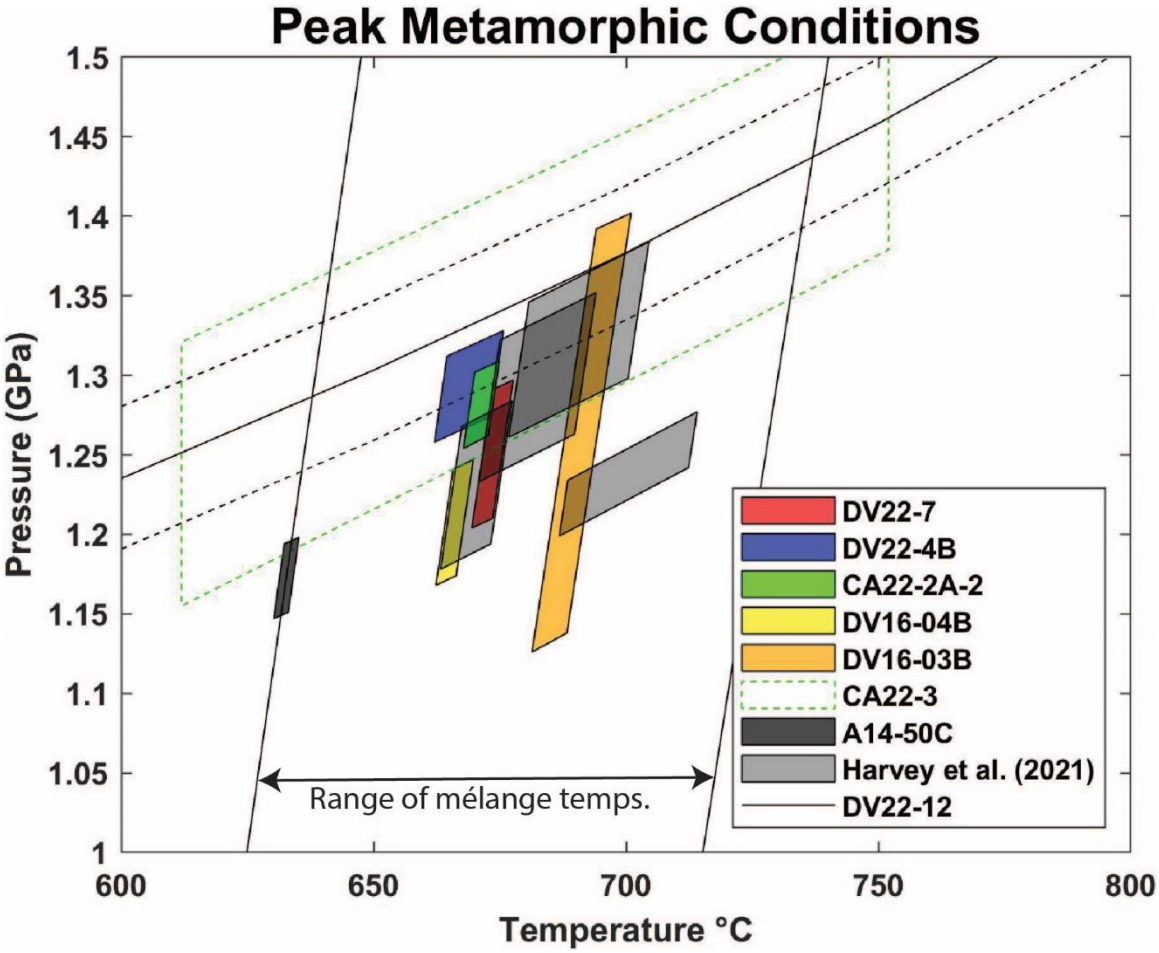


Figure 33. PT results based on QuiG and ZiR results for samples analyzed in this study and for those recalculated from Harvey et al. (2021). The colored polygons are samples of coherent amphibolite. The Harvey et al. (2021) samples (light gray) and A14-50C (dark gray) are blocks in amphibolite mélange. The isopleths for A14-50C were calculated from Zr concentrations reported in Penniston-Dorland et al., (2018). The isomeke for DV22-12, which lacks a temperature estimate, is the curving sub-horizontal black line, with its ± 2σ isomekes (dashed lines). The dashed green box is for CA22-3, which has only Ti-in-amphibole temperature estimates. Note that the pressure estimate for DV16-03B is based on a single QuiG inclusion. The full range of temperatures recorded by blocks in the amphibolite mélange are shown as vertical black isopleths (from Penniston-Dorland et al., 2018).

In determining whether the coherent amphibolite experienced a different metamorphic history than the amphibolite mélange, the question becomes: What is the appropriate benchmark for comparison? Blocks in mélange are interpreted to have been transported during metamorphism (Penniston-Dorland et al., 2018). Based on Figure 33, the coherent amphibolite samples overlap with the blocks in mélange reported by Harvey et al. (2021a). These samples, however, record temperatures from roughly the middle of the

range for mélange blocks and are not necessarily appropriate for comparison. We assume that each block records its peak metamorphic conditions, but that its current location does not reflect its position at the peak of metamorphism (Figure 34). Another way of saying this is that each block could have traveled only to shallower levels than its peak depth. With this assumption in mind, the best available benchmark for comparing the two units is the coldest and lowest-pressure block in mélange, because it is the best proxy for P-T conditions at the time the coherent amphibolite and mélange reached their final juxtaposition. This block (A14-50C) recorded conditions that reflect its maximum depth attained inside the subduction zone. All other blocks could have, and should be assumed to have, moved up the subduction interface from their maximum depths. The coherent amphibolite samples with available Zr-in-rutile data plot significantly hotter (>50 °C) than A14-50C, and with generally higher pressures. From this we can conclude that the coherent amphibolite was subducted deeper than A14-50C, but to approximately similar depths as many of the other blocks in amphibolite mélange.

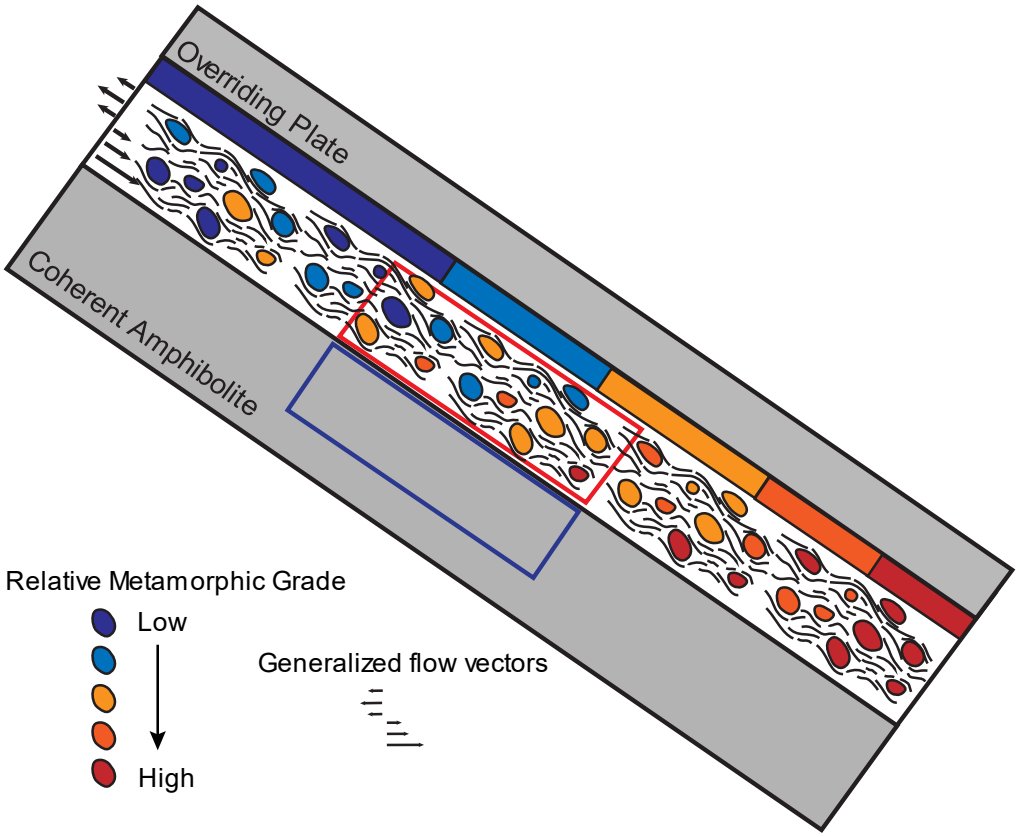


Figure 34. Schematic diagram of the Catalina Schist amphibolite mélange and coherent amphibolite, with red and blue rectangles indicating the current exposures of each. Color scale bar represents the greatest depths attained by mélange blocks from each of five hypothetical metamorphic grades. The lowest-grade block within the current exposure of mélange, here a dark blue, represents the best benchmark for comparison with the coherent amphibolite because all higher-grade blocks have circulated upward from their source regions.

Implications for Movement at the Subduction Interface

If we continue using the calculated geothermal gradient of ~18 °C/km, then a temperature difference of 50 °C represents a difference in maximum depth of around 3 km. This means that the coherent amphibolite and many of the blocks in mélange moved upwards from their maximum depths until they reached their current juxtaposition with A14-50C. If we assume a slab dip of 20°, then the coherent amphibolite may have moved along the subduction interface, relative to the mélange, by about 9 km. Previous models for the movement of material at the subduction interface have focused on mélange and relied on

either large-scale return flow driven by a wedge-shaped interface (Cloos, 1982; Gerya et al., 2002; see also Platt, 1993) or smaller-scale stress amplification and strain localization caused by rheological heterogeneities (Beall et al., 2019; Fagereng and Sibson, 2010; see also Angiboust et al., 2011). Neither modality explores the possibility for the movement of whole tectonic slices along with blocks in mélange.

We know from the proto-mélange in Dawn Valley that strain localization and mass movement may take place at multiple scales, and that this proto-mélange development may be simultaneous with movement on the larger megathrust mélange zone. We also know that in order for the coherent amphibolite to have underplated to the overriding plate, it first needed to detach from the downgoing slab (Agard et al., 2018). Lastly, we know from the infilling of the Cottonwood Canyon fault that mélange was actively deforming at the same time as the coherent amphibolite. In order to explain these observations, a new model for the emplacement of the coherent amphibolite is proposed (Figure 35). In the beginning, the coherent amphibolite was still attached to the downgoing slab. Then, a new basal fracture (or décollement) begins to open up, perhaps along an area of existing mechanical weakness such as a remnant ocean fracture zone or a layer of intensely metasomatized rock. The coherent amphibolite, which is now a raft unzipping from the downgoing slab, may begin to break apart. As it fractures, the mélange matrix fills in open spaces. Once the coherent amphibolite has completely broken free, mélange begins to flow beneath it. The opening of a new flow channel would disrupt the overall pattern of strain localization and the raft of coherent amphibolite may begin moving backwards up the interface with other blocks experiencing return flow. It may continue to break apart at its edges as it does so, just as

we see in the small fault in Cottonwood Canyon. Eventually the coherent amphibolite comes to a rest with its nearby entourage of blocks as the mélange stiffens and cools and a new subduction interface is fully activated beneath it. In this scenario, the current juxtaposition of the coherent amphibolite with the mélange reflects movement that occurred after peak metamorphism.

In some ways this model treats the coherent amphibolite like an extremely large block in matrix. Mélange blocks, however, are typically thought of as being fully encased in matrix material, and we know this is not the case for the coherent amphibolite. While the coherent amphibolite is directly juxtaposed against the underlying epidote blueschist today, however, this does not always have to have been the case. If the amphibolite mélange incorporated ultramafic material from the overriding plate (Bebout and Barton, 2002), then it follows that the new, lower grade mélange zone would strip material from the recently underplated unit above it. This, in addition to the possibility for fault reactivation during exhumation, means that the original boundaries between these units may be obscured. The Ollas thrust, for example, does not necessarily represent the original basal decollement that opened beneath the coherent amphibolite. It was active at around the peak metamorphic conditions (Harvey et al., 2021a), but it could just represent a metasomatized layer along the proto-mélange continuum. This could perhaps explain the disparity between field observations of subduction interface thickness (300 to 500 m; Agard et al., 2018) and geophysical observations of interface thickness (5-10 km or less; Calvert, 2004). The coherent amphibolite is roughly 1 km thick, so an interface of 5-10 km total thickness is more likely to accommodate the movement of such a large terrane.

Another possibility is that the coherent amphibolite detached from the downgoing slab but its encasement in the mélange was short lived. Its movement upwards may have been arrested by a narrowing of the mélange, effectively clogging the interface. Such an event would have forced a massive reorganization of strain between the plates, perhaps contributing to the downstepping of the main mélange interface. The underthrusting of higher-pressure tectonic slices beneath lower pressure ones has been observed in the Zagros blueschists in Iran (Angiboust et al., 2016). Those authors hypothesized that this underthrusting could have been facilitated by a geodynamic perturbation to the subduction system as a whole, or by the subduction of buoyant material into the interface. A known perturbation occurred at around 95-90 Ma, when the system transitioned to shallow-angle subduction (Jacobsen et al., 2011), but this would post-date the accretion of the lowest-grade units of the Catalina Schist, too late to affect the coherent amphibolite's juxtaposition with the mélange. As for the second possibility, serpentinite is known to be a more buoyant material than metamafic slabs (Guillot et al., 2015). It has been suggested for other mélange zones that exhumation was facilitated by serpentinite lowering the overall density of subducting rocks (Malatesta et al., 2012; Federico et al., 2007; see also Agard et al., 2009). The association of the coherent amphibolite with the Dawn Valley serpentinite body raises the possibility that its buoyancy played a role in the upward movement of the coherent amphibolite. Without knowing more about how and when the serpentinite was emplaced, however, this possibility is merely speculative.

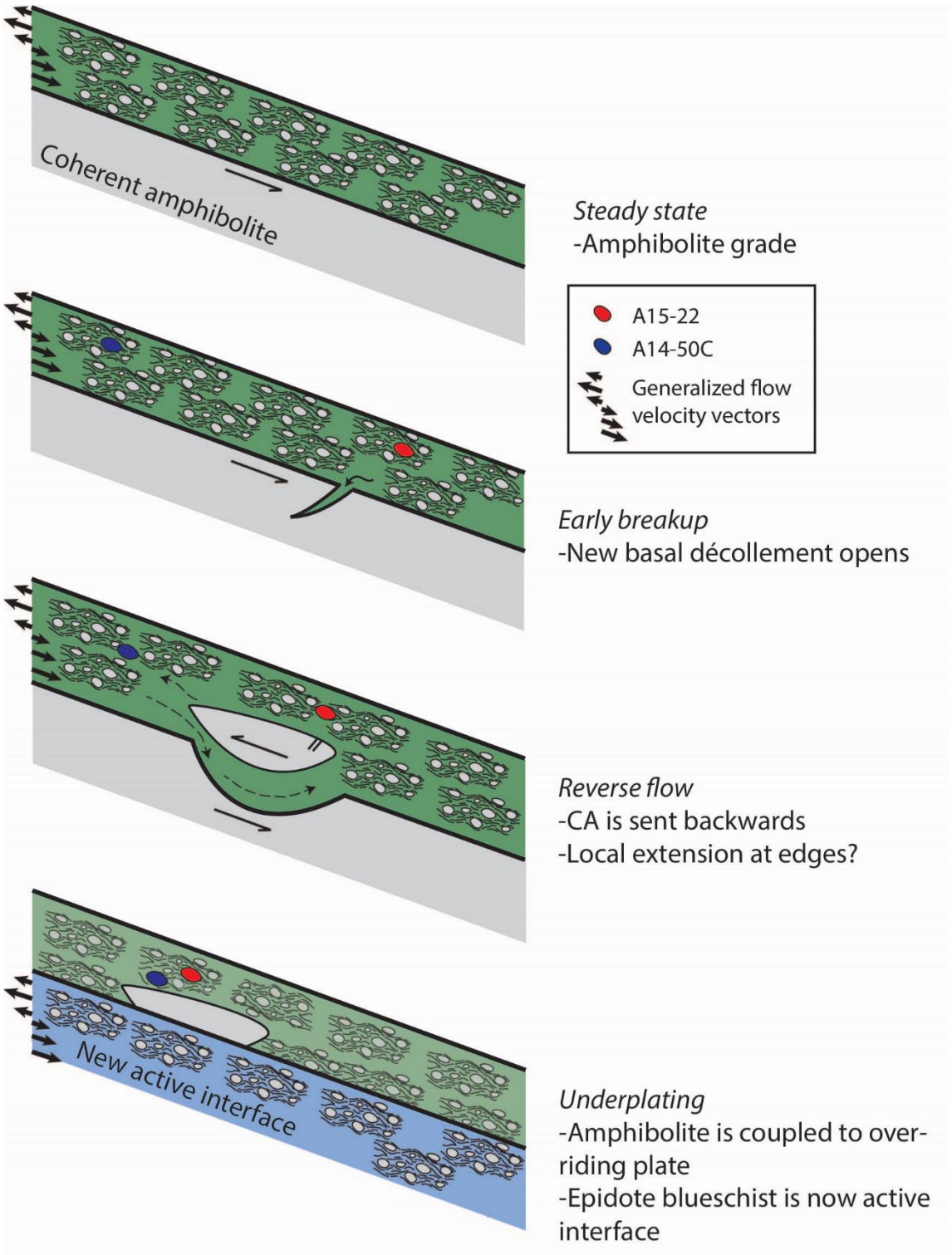


Figure 35. Conceptual model for emplacement of coherent amphibolite. Beginning with steady subduction, the coherent amphibolite is first shaved off the downgoing slab by the opening of a new basal décollement. It begins to break apart until it is fully liberated from the slab. Once this occurs, the sudden shift in mélange flow may allow for the coherent amphibolite and nearby blocks to flow backwards up the interface. It may continue to break apart through extension, as evidenced by the high angle normal fault

observed in Cottonwood Canyon. The coherent amphibolite along with the mélange is eventually underplated to the overriding plate, and a new subduction interface opens up beneath it. The movement of two reference blocks in mélange are shown in red (hot) and blue (cold).

Conclusion

The coherent amphibolite of the Catalina Schist records peak metamorphic conditions of 1.2 to 1.29 GPa and 665 to 691 °C. It broadly overlaps with some of the blocks in the amphibolite mélange, which have been recalculated here from Harvey et al. (2021a). The coherent amphibolite does, however, record hotter temperatures than the coldest block in mélange. This suggests that the coherent amphibolite, along with the hotter mélange blocks, experienced some degree of upwards movement along the subduction interface before reaching its current juxtaposition with the mélange.

The field and petrographic observations presented here paint a more holistic picture of the coherent amphibolite, and by extension, the subducting slab. These observations include:

1. A discordant boundary between the coherent amphibolite and the overlying mélange that seems to cut obliquely across the metasedimentary layers.
2. A thermal gradient across the coherent amphibolite, with higher temperatures recorded at the top, nearer its contact with the mélange.
3. Possible proto-mélanges within the coherent amphibolite that are hosted by metasomatic rocks and suggest that mass transport and strain localization occurred at smaller scales than the main megathrust shear zone.

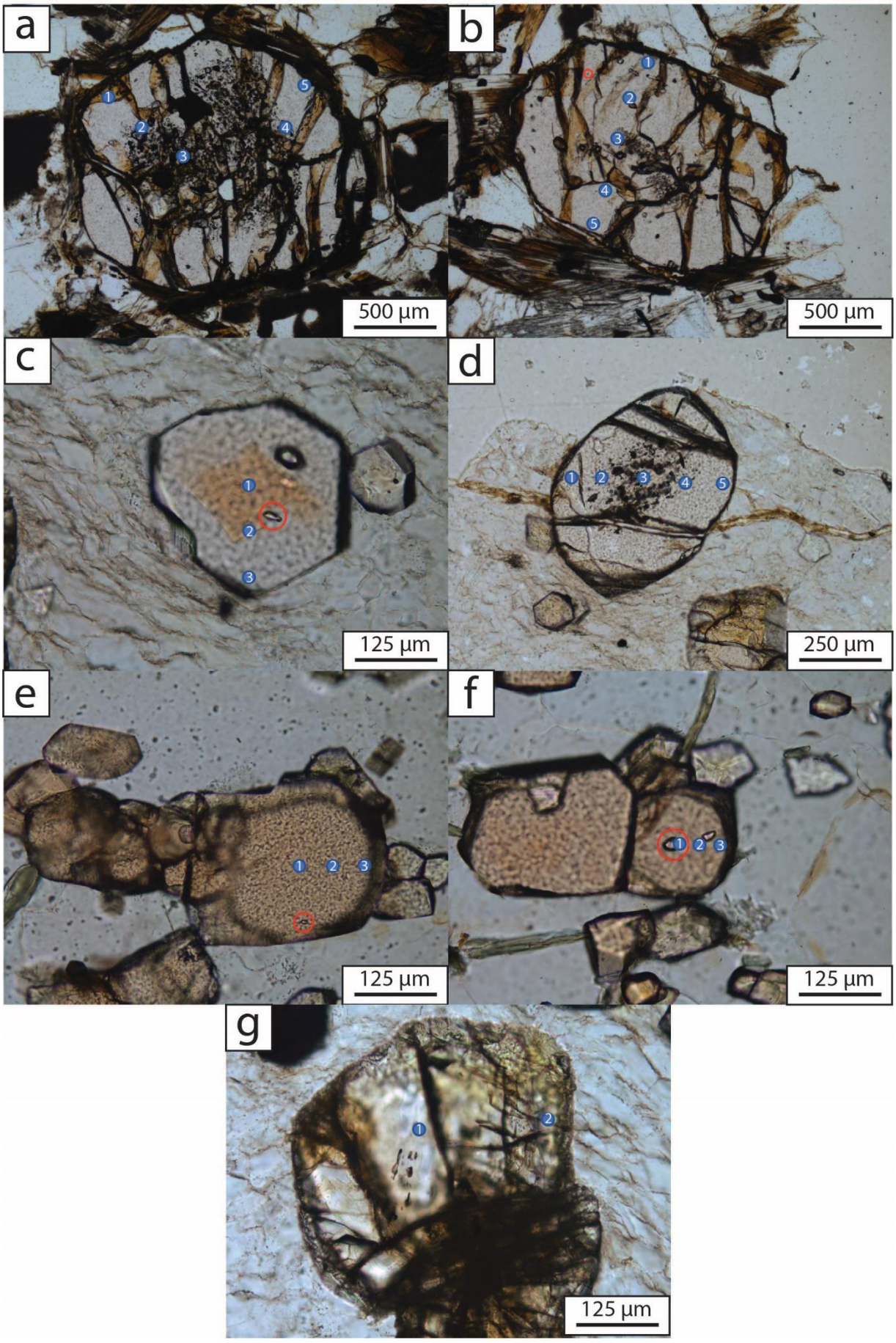
This work highlights the importance of looking to coherent terranes for learning more about subduction zone interfaces. The coherent amphibolite was not just a passive

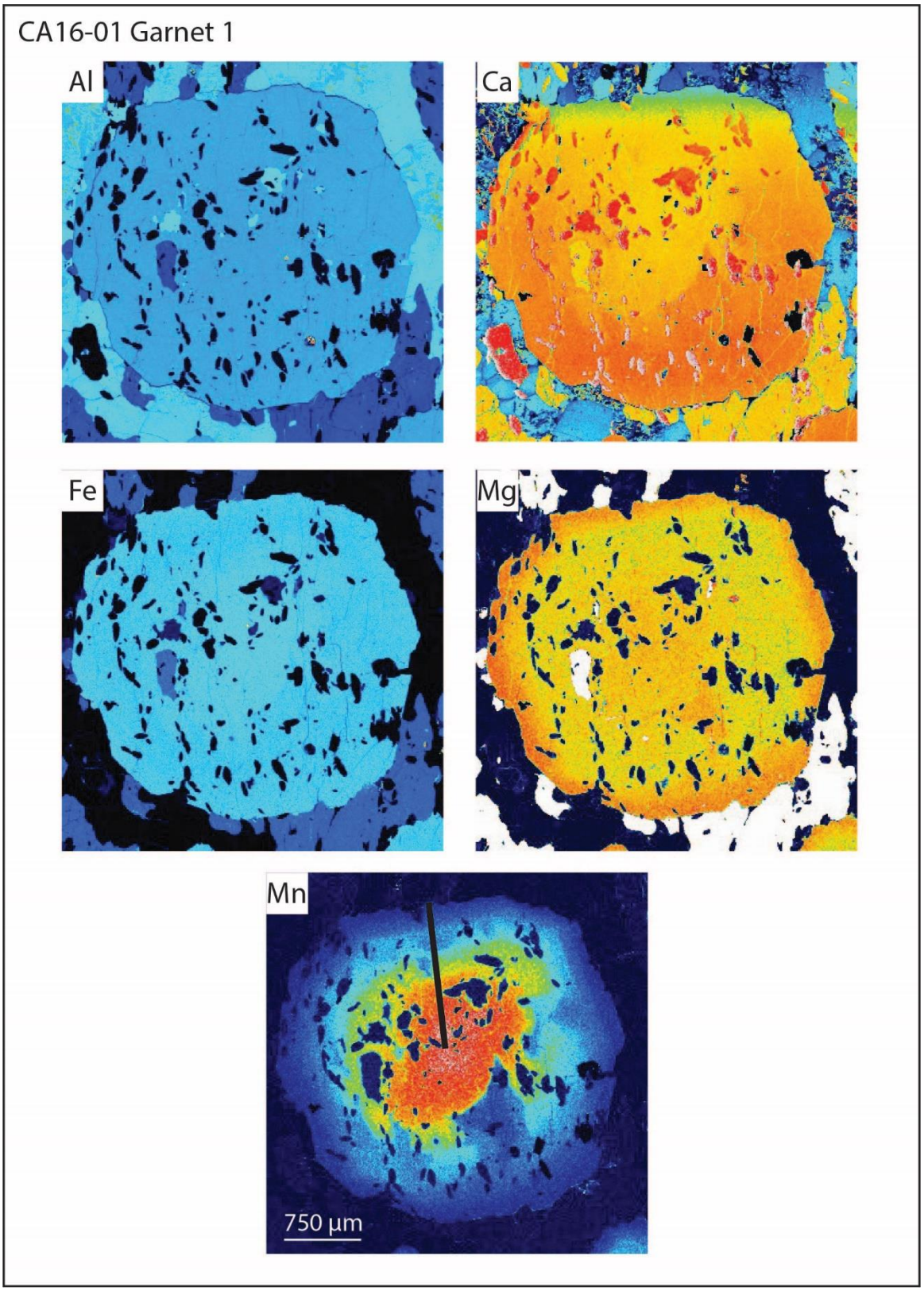
tectonic slice while mélange deformed around it, but rather an active participant in that deformation.

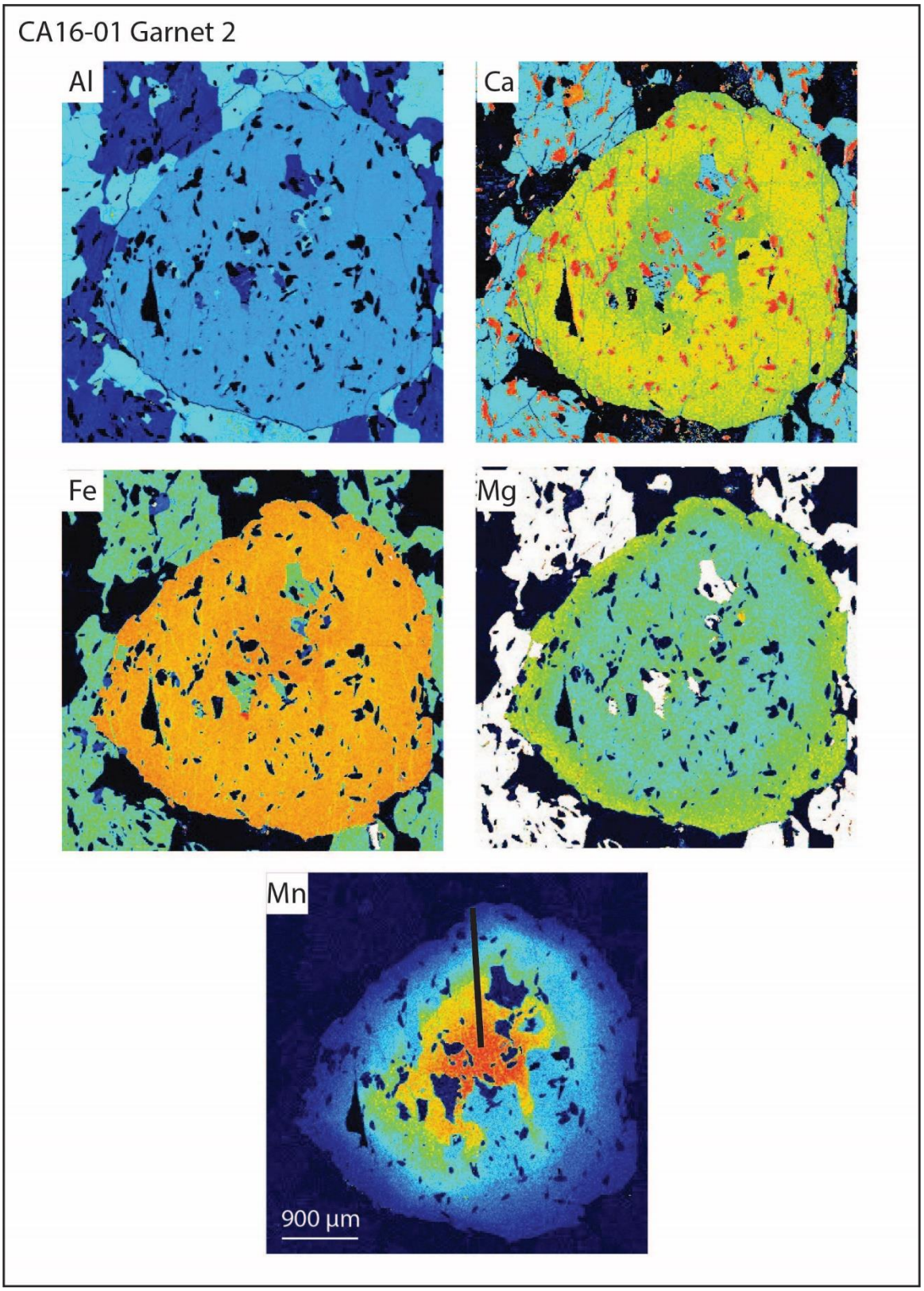
Appendix A: QuiG Results

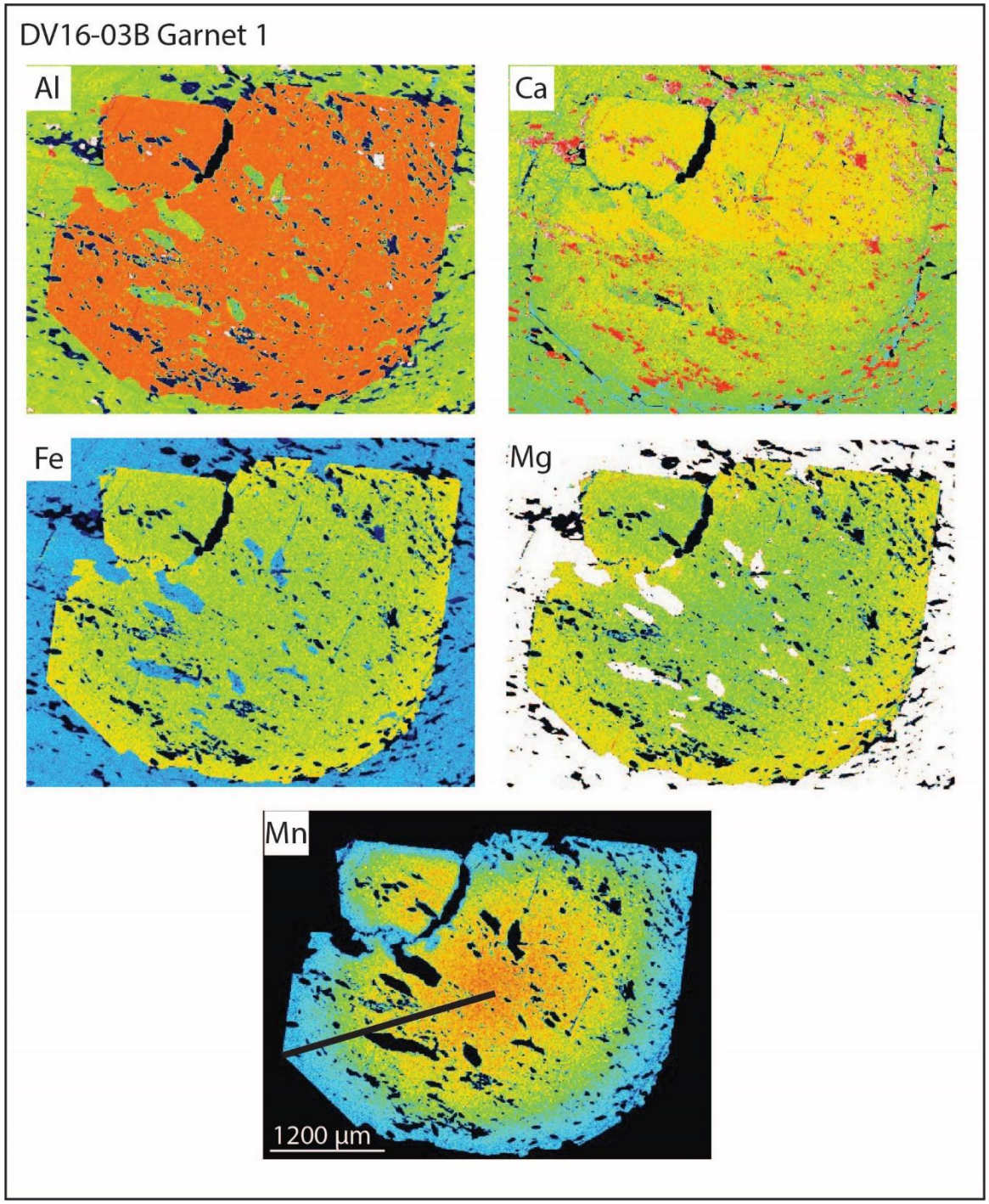
A.1: Garnet Chemistry

Figure A.1. Photomicrographs of garnets with the locations of WDS spots marked (see Table A.1). All images are in PPL. Red circles indicate quartz inclusions used for QuiG. **a.** Paragneiss DV22-4B Garnet 29 (5x). **b.** DV22-4B Garnet 25 (5x). **c.** Quartzite DV22-7 Q2 (20x). **d.** DV22-7 G1 (10x). **e.** Quartzite CA22-2A-2 Q10 (20x). **f.** CA22-2A-2 Q2 (20x). **g.** Quartzite DV22-7 Q8 (20x).


a
1
2
3
4
5
500 µm
b
1
2
3
4
5
500 µm
c
1
2
3
125 µm
d
1
2
3
4
5
250 µm
e
1
2
3
125 µm
f
1
2
3
125 µm
g
1
2
125 µm


CA16-01 Garnet 1
Al
Ca
Fe
Mg
Mn
750 µm


CA16-01 Garnet 2
Al
Ca
Fe
Mg
Mn
900 µm


DV16-03B Garnet 1
Al
Ca
Fe
Mg
Mn
1200 µm

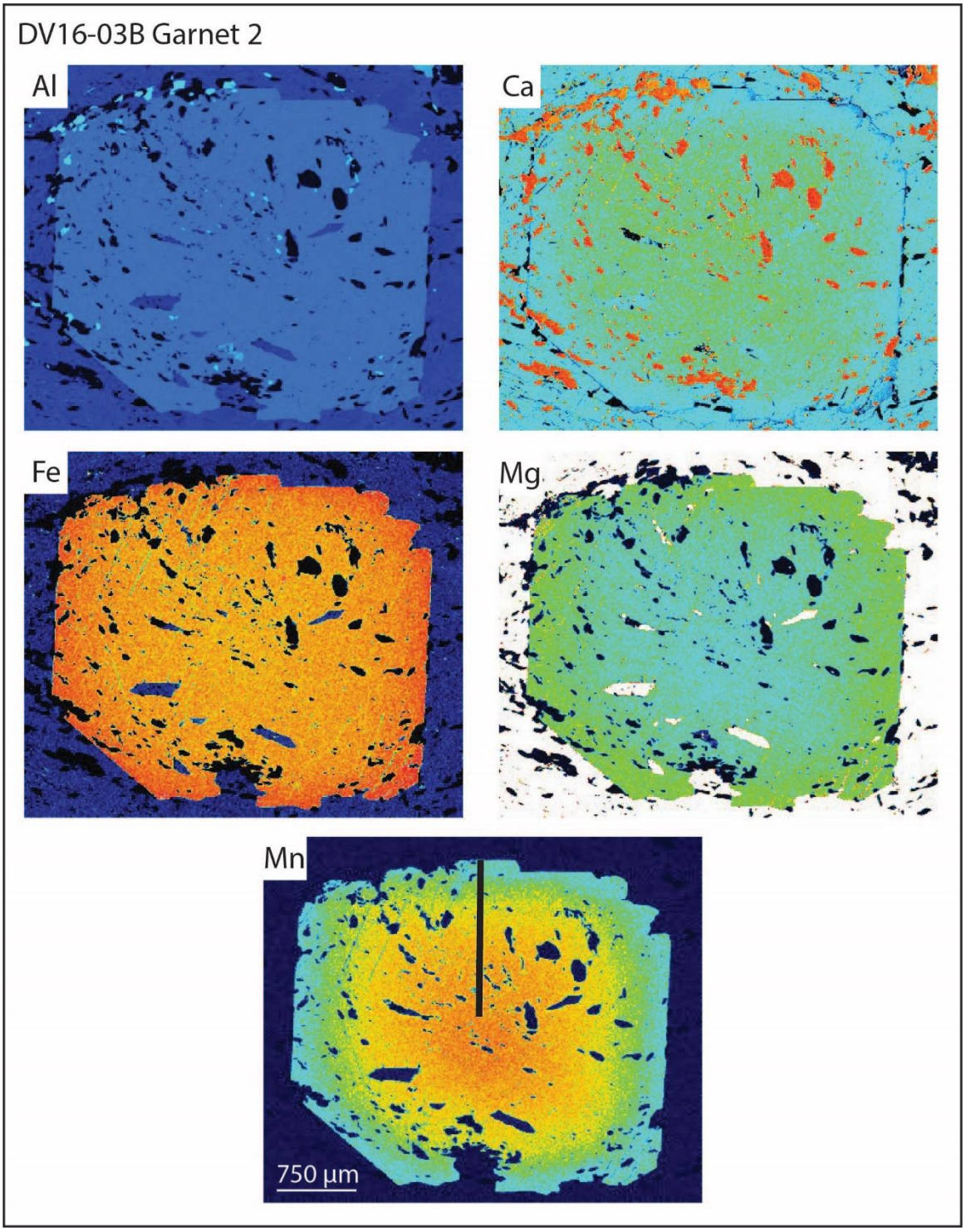


Figure A.2 Major element (Al, Ca, Fe, Mg, and Mn) X-ray maps of four mafic amphibolite garnets. Images were processed using ImageJ. Colors indicate only relative

concentrations of elements, with warmer colors indicating higher concentrations. The paths of core-to-rim WDS traverses are denoted by black lines on the Mn maps.

Table A.1. Garnet WDS Major Element Analyses

Quartzite			EPMA Results										% Endmembers					
Sample	**Grain #**	**Garnet zone**	**MgO**	**MnO**	**TiO_2**	**CaO**	**Al_2O_3**	**Na_2O**	**FeO**	**K_2O**	**SiO_2**	**Total**	**pyrope**	**almandine**	**spessartine**	**grossular**	**# on Figure A.1**	**Distance from center (µm)**
CA22-2A-2	Q2	core	4.25	7.96	0.06	4.95	20.73	0.04	23.82	0.00	36.97	98.78	17	52	18	14	1	0
CA22-2A-2	Q2	mantle	4.09	7.85	0.00	4.93	19.92	0.04	23.75	0.00	37.24	97.82	16	52	18	14	2	52
CA22-2A-2	Q2	rim	4.46	7.21	0.06	5.55	20.72	0.00	23.19	0.00	37.34	98.53	17	51	16	16	3	99
CA22-2A-2	Q10	core	4.89	7.13	0.07	4.82	20.80	0.00	23.63	0.00	37.26	98.60	19	52	16	13	1	0
CA22-2A-2	Q10	mantle	4.98	7.10	0.12	4.86	20.62	0.01	23.77	0.00	37.33	98.79	19	52	16	14	2	30
CA22-2A-2	Q10	rim	4.82	6.68	0.04	5.01	20.66	0.00	23.94	0.01	37.38	98.54	19	52	15	14	3	61
DV22-7	Q2	core	8.98	5.33	0.15	1.98	20.98	0.00	23.09	0.00	37.97	98.48	34	49	11	5	1	0
DV22-7	Q2	mantle	9.08	5.06	0.17	2.53	21.19	0.03	23.00	0.00	37.73	98.78	34	48	11	7	2	70
DV22-7	Q2	rim	8.60	4.67	0.00	3.17	21.15	0.08	22.14	0.00	38.18	97.99	33	48	10	9	3	141
DV22-7	Q8	core	8.76	5.18	0.25	2.74	20.94	0.04	22.83	0.00	38.24	98.98	33	48	11	7	1	0
DV22-7	Q8	rim	8.71	4.64	0.01	3.11	21.60	0.02	22.31	0.00	38.26	98.66	33	48	10	9	2	195
DV22-7	G1	rim	8.69	4.55	0.00	2.94	21.44	0.07	21.96	0.00	37.98	97.63	34	48	10	8	1	220
DV22-7	G1	mantle	8.31	4.64	0.00	3.60	21.22	0.10	22.03	0.00	38.03	97.93	32	48	10	10	2	125
DV22-7	G1	core	8.42	4.68	0.06	3.56	21.30	0.05	22.13	0.00	37.99	98.18	32	48	10	10	3	0
DV22-7	G1	mantle	8.78	4.40	0.05	3.50	21.16	0.00	21.89	0.02	37.67	97.47	34	47	10	10	4	129
DV22-7	G1	rim	8.63	4.39	0.00	3.19	21.51	0.06	21.79	0.01	37.85	97.43	34	48	10	9	5	240

Paragneiss			EPMA Results										% Endmembers					
Sample	**Grain #**	**Garnet zone**	**MgO**	**MnO**	**TiO_2**	**CaO**	**Al_2O_3**	**Na_2O**	**FeO**	**K_2O**	**SiO_2**	**Total**	**pyrope**	**almandine**	**spessartine**	**grossular**	**# on Figure A.1**	**Distance from center (µm)**
DV22-4B	G25	rim	7.62	0.40	0.08	4.26	21.46	0.00	26.92	0.00	37.92	98.66	29	58	1	12	1	498
DV22-4B	G25	mantle	7.65	0.54	0.03	2.93	21.39	0.03	28.50	0.01	37.47	98.56	29	61	1	8	2	254
DV22-4B	G25	core	7.48	0.55	0.02	2.69	21.45	0.03	28.40	0.01	37.38	98.01	29	62	1	8	3	0
DV22-4B	G25	mantle	7.35	0.61	0.04	2.28	21.37	0.01	28.99	0.02	37.48	98.15	29	64	1	6	4	326
DV22-4B	G25	rim	7.06	0.37	0.01	4.88	21.31	0.04	26.66	0.00	37.83	98.16	27	58	1	14	5	540
DV22-4B	G29	rim	7.38	0.45	0.05	4.29	21.50	0.02	27.00	0.00	37.93	98.62	29	59	1	12	1	838
DV22-4B	G29	mantle	7.45	0.53	0.00	2.77	20.47	0.00	28.35	0.04	37.01	96.63	29	62	1	8	2	567
DV22-4B	G29	core	7.70	0.66	0.12	2.84	21.54	0.02	28.03	0.00	37.79	98.69	30	61	1	8	3	267
DV22-4B	G29	mantle	7.90	0.65	0.01	2.80	21.70	0.02	28.45	0.00	37.55	99.07	30	61	1	8	4	463
DV22-4B	G29	rim	7.46	0.39	0.06	3.95	21.20	0.00	27.62	0.00	37.56	98.24	29	60	1	11	5	723

Mafic amphibolite			EPMA Results										% Endmembers				
Sample	**Grain #**	**Analysis #**	**MgO**	**MnO**	**TiO_2**	**CaO**	**Al_2O_3**	**Na_2O**	**FeO**	**K_2O**	**SiO_2**	**Total**	**pyrope**	**almandine**	**spessartine**	**grossular**	**Distance from center (µm)**
CA16-01	1	1	2.07	2.59	0.14	10.97	21.59	0.00	23.78	-0.01	37.90	99.03	8	54	6	32	0
CA16-01	1	2	2.12	2.55	0.25	11.44	21.40	0.04	23.64	-0.01	38.18	99.62	8	53	6	33	61.12
CA16-01	1	3	2.15	2.60	0.10	11.16	21.32	0.01	23.75	-0.01	38.12	99.21	9	53	6	32	122.24
CA16-01	1	4	2.13	2.54	0.17	11.47	21.44	0.01	23.72	0.00	37.95	99.42	8	53	6	33	183.36
CA16-01	1	5	2.13	2.55	0.21	11.49	21.04	0.05	23.56	0.00	37.85	98.90	9	53	6	33	244.48
CA16-01	1	6	2.17	2.41	0.08	11.43	21.41	0.04	23.68	0.00	36.79	98.01	9	53	5	33	305.6
CA16-01	1	7	2.03	2.35	0.08	11.56	21.43	0.00	23.75	-0.01	38.04	99.21	8	53	5	33	366.72

Mafic amphibolite			EPMA Results										% Endmembers				
Sample	**Grain #**	**Analysis #**	**MgO**	**MnO**	**TiO_2**	**CaO**	**Al_2O_3**	**Na_2O**	**FeO**	**K_2O**	**SiO_2**	**Total**	**pyrope**	**almandine**	**spessartine**	**grossular**	**Distance from center (µm)**
CA16-01	1	8	2.09	2.38	0.12	11.60	21.26	0.00	23.29	-0.01	37.91	98.65	8	53	5	34	427.84
CA16-01	1	9	2.06	2.30	0.11	11.49	21.31	0.00	23.07	0.01	37.99	98.33	8	53	5	34	488.96
CA16-01	1	10	2.23	1.85	0.09	11.81	21.08	-0.01	23.70	0.00	38.23	98.97	9	53	4	34	611.2
CA16-01	1	11	2.18	1.83	0.09	12.45	21.54	0.03	23.45	0.00	37.99	99.56	9	52	4	35	672.32
CA16-01	1	12	1.99	1.54	0.06	12.72	21.62	-0.01	23.57	0.01	38.28	99.78	8	52	3	36	733.44
CA16-01	1	13	2.02	1.36	0.03	13.06	21.45	0.04	22.88	0.01	38.22	99.06	8	51	3	38	794.56
CA16-01	1	14	1.93	1.26	0.05	13.48	21.37	0.00	22.84	0.00	38.33	99.28	8	51	3	39	855.68
CA16-01	1	15	2.00	1.13	0.09	13.82	21.56	0.02	22.77	0.00	38.11	99.50	8	50	3	39	916.8
CA16-01	1	16	1.94	0.82	0.06	14.18	21.74	0.01	22.44	0.00	37.97	99.15	8	50	2	40	977.92
CA16-01	1	17	1.91	0.59	0.06	14.83	21.50	0.01	22.01	0.01	38.49	99.40	8	49	1	42	1039.04
CA16-01	1	18	2.00	0.49	0.11	14.68	21.51	-0.01	22.02	-0.01	38.32	99.12	8	49	1	42	1100.16
CA16-01	1	19	1.91	0.61	0.10	14.80	21.33	0.03	21.77	0.02	38.29	98.86	8	49	1	42	1161.28
CA16-01	1	20	1.92	0.60	0.09	14.67	21.70	0.02	22.38	0.00	38.26	99.65	8	50	1	42	1222.4
CA16-01	1	21	2.03	0.40	0.13	14.14	21.46	0.01	22.46	0.01	38.08	98.72	8	50	1	41	1283.52
CA16-01	1	22	2.19	0.35	0.09	14.45	21.55	0.00	22.65	0.00	38.28	99.57	9	50	1	41	1344.64
CA16-01	1	23	2.29	0.23	0.11	14.21	21.50	0.06	22.42	0.01	38.50	99.32	9	50	1	41	1405.76
CA16-01	1	24	2.27	0.19	0.10	13.73	21.64	0.00	23.21	0.00	38.38	99.51	9	52	0	39	1466.88
CA16-01	2	1	2.08	2.44	0.23	12.06	21.46	0.01	23.14	0.02	38.46	99.91	8	52	6	34	0
CA16-01	2	2	1.94	2.43	0.12	12.44	21.36	0.02	23.15	0.01	38.22	99.69	8	51	5	35	73.33
CA16-01	2	3	2.07	2.29	0.06	12.39	21.66	0.01	23.06	0.00	38.23	99.77	8	51	5	35	146.66
CA16-01	2	4	2.09	2.40	0.10	12.68	21.54	0.02	22.79	0.00	38.35	99.96	8	50	5	36	219.99
CA16-01	2	5	2.07	2.32	0.04	12.70	21.65	-0.01	23.12	0.00	38.35	100.25	8	51	5	36	293.32

Mafic amphibolite			EPMA Results										% Endmembers				
Sample	**Grain #**	**Analysis #**	**MgO**	**MnO**	**TiO_2**	**CaO**	**Al_2O_3**	**Na_2O**	**FeO**	**K_2O**	**SiO_2**	**Total**	**pyrope**	**almandine**	**spessartine**	**grossular**	**Distance from center (µm)**
CA16-01	2	6	1.95	2.10	0.10	12.58	21.54	0.04	22.75	0.00	38.44	99.48	8	51	5	36	366.65
CA16-01	2	7	1.82	2.05	0.02	12.97	21.20	0.00	22.66	0.00	38.44	99.16	7	51	5	37	439.98
CA16-01	2	8	1.86	2.01	0.04	12.98	21.92	-0.01	22.82	-0.01	38.18	99.80	7	51	5	37	513.31
CA16-01	2	9	1.85	1.97	0.13	13.20	21.60	-0.01	22.40	-0.01	38.56	99.69	7	50	4	38	586.64
CA16-01	2	10	1.82	1.96	0.18	13.59	21.44	0.03	22.31	0.00	38.07	99.39	7	50	4	39	659.97
CA16-01	2	11	1.98	1.88	0.14	13.08	21.52	0.01	22.55	0.00	38.46	99.64	8	50	4	37	733.3
CA16-01	2	12	2.04	1.82	0.11	13.43	21.38	0.01	22.86	-0.01	38.31	99.95	8	50	4	38	806.63
CA16-01	2	13	2.01	1.72	0.10	13.48	21.78	-0.01	22.41	-0.01	38.29	99.77	8	50	4	38	879.96
CA16-01	2	14	1.99	1.37	0.05	13.79	21.77	0.02	22.45	0.01	38.31	99.75	8	50	3	39	953.29
CA16-01	2	15	2.15	0.97	0.07	14.10	21.56	0.03	22.53	0.00	38.37	99.80	8	50	2	40	1026.62
CA16-01	2	16	1.97	1.03	0.16	14.86	21.65	0.04	21.98	0.00	38.49	100.18	8	48	2	42	1099.95
CA16-01	2	17	1.99	1.03	0.11	14.49	21.72	0.02	21.73	0.00	38.76	99.84	8	48	2	41	1173.28
CA16-01	2	18	1.84	0.80	0.12	14.82	21.55	0.03	22.10	0.00	38.40	99.67	7	49	2	42	1246.61
CA16-01	2	19	1.99	0.64	0.16	14.87	21.34	0.05	22.34	0.00	38.23	99.62	8	49	1	42	1319.94
CA16-01	2	20	1.88	0.66	0.12	14.68	21.61	-0.01	22.16	-0.01	38.64	99.74	7	49	1	42	1393.27
CA16-01	2	21	2.15	0.51	0.12	14.69	21.59	0.03	22.44	-0.01	38.29	99.79	8	49	1	41	1466.6
CA16-01	2	22	2.16	0.35	0.08	14.27	21.73	0.01	22.58	0.01	38.77	99.96	9	50	1	41	1539.93
CA16-01	2	23	2.37	0.26	0.08	14.35	21.28	0.01	22.72	0.00	38.55	99.61	9	50	1	40	1613.26
CA16-01	2	24	2.37	0.23	0.08	13.84	21.57	0.01	22.99	-0.01	38.52	99.61	9	51	1	39	1686.59
CA16-01	2	25	2.21	0.21	0.04	13.24	21.87	0.01	22.78	0.01	38.55	98.90	9	52	0	39	1759.92
DV16-03B	1	1	3.53	2.85	0.12	12.10	21.91	0.05	20.72	0.01	38.86	100.16	14	46	6	34	0
DV16-03B	1	2	3.48	2.77	0.17	12.39	22.02	0.00	20.95	0.00	38.94	100.70	14	46	6	35	98.02

Mafic amphibolite			EPMA Results										% Endmembers				
Sample	**Grain #**	**Analysis #**	**MgO**	**MnO**	**TiO_2**	**CaO**	**Al_2O_3**	**Na_2O**	**FeO**	**K_2O**	**SiO_2**	**Total**	**pyrope**	**almandine**	**spessartine**	**grossular**	**Distance from center (µm)**
DV16-03B	1	3	3.58	2.65	0.29	12.08	21.97	-0.01	20.56	-0.01	38.76	99.85	14	46	6	34	196.04
DV16-03B	1	4	3.60	2.47	0.10	11.97	21.62	0.01	20.64	0.00	38.27	98.69	14	46	6	34	294.06
DV16-03B	1	5	3.60	2.51	0.22	11.94	21.81	0.02	20.53	0.01	38.01	98.64	14	46	6	34	392.08
DV16-03B	1	6	3.58	2.66	0.17	12.18	21.80	0.01	20.61	0.00	38.32	99.33	14	46	6	34	490.1
DV16-03B	1	7	3.41	2.54	0.16	12.33	21.86	0.00	20.54	0.00	38.32	99.16	14	46	6	35	588.12
DV16-03B	1	8	3.42	2.49	0.26	12.17	21.63	0.06	20.74	0.01	38.46	99.23	14	46	6	35	686.14
DV16-03B	1	9	3.59	2.46	0.16	12.40	21.78	0.00	20.65	0.00	38.51	99.54	14	45	5	35	784.16
DV16-03B	1	10	3.58	2.27	0.17	12.18	21.60	-0.01	20.47	0.00	38.46	98.73	14	46	5	35	882.18
DV16-03B	1	12	3.60	2.48	0.10	12.04	21.93	0.02	20.90	0.00	38.26	99.33	14	46	6	34	1078.22
DV16-03B	1	13	3.63	2.43	0.13	11.78	22.03	0.02	21.06	0.00	38.47	99.55	14	47	5	33	1176.24
DV16-03B	1	14	3.65	2.34	0.18	12.01	22.06	0.05	21.04	0.00	38.29	99.62	14	46	5	34	1274.26
DV16-03B	1	15	3.49	2.26	0.15	12.18	21.75	-0.01	20.62	0.00	37.95	98.39	14	46	5	35	1372.28
DV16-03B	1	16	3.70	2.25	0.08	11.70	22.16	0.00	21.32	0.00	38.73	99.94	15	47	5	33	1470.3
DV16-03B	1	17	3.56	2.16	0.13	12.33	22.17	-0.01	21.14	0.00	38.80	100.28	14	46	5	35	1568.32
DV16-03B	1	18	3.86	1.97	0.05	11.61	22.20	0.01	21.04	0.00	38.27	98.99	15	47	4	33	1666.34
DV16-03B	1	19	3.88	1.81	0.09	11.80	22.24	0.02	21.45	0.00	39.06	100.34	15	47	4	33	1764.36
DV16-03B	1	20	3.96	1.76	0.12	11.79	21.71	0.02	21.55	-0.01	38.60	99.50	16	47	4	33	1862.38
DV16-03B	1	22	3.96	1.53	0.10	11.24	22.18	0.00	22.36	0.00	38.86	100.22	16	49	3	32	2058.42
DV16-03B	1	23	4.01	1.50	0.11	11.34	21.88	0.06	22.53	0.00	38.64	100.06	16	49	3	32	2156.44
DV16-03B	1	24	4.12	1.41	-0.02	10.88	22.25	0.01	22.35	0.00	38.91	99.90	16	50	3	31	2254.46
DV16-03B	1	25	3.90	1.47	0.04	9.60	22.18	-0.01	24.18	-0.01	38.70	100.04	15	54	3	27	2352.48
DV16-03B	2	1	3.53	2.68	0.25	12.38	21.72	0.05	20.20	-0.01	38.85	99.64	14	45	6	35	0

Mafic amphibolite			EPMA Results										% Endmembers				
Sample	**Grain #**	**Analysis #**	**MgO**	**MnO**	**TiO_2**	**CaO**	**Al_2O_3**	**Na_2O**	**FeO**	**K_2O**	**SiO_2**	**Total**	**pyrope**	**almandine**	**spessartine**	**grossular**	**Distance from center (µm)**
DV16-03B	2	2	3.50	2.75	0.12	12.58	22.13	0.01	20.78	-0.01	38.81	100.65	14	45	6	35	59.35
DV16-03B	2	3	3.74	2.67	0.05	11.43	22.06	0.03	20.84	-0.01	38.71	99.52	15	46	6	33	118.7
DV16-03B	2	4	3.52	2.74	0.17	12.09	22.09	0.01	20.91	0.01	38.56	100.10	14	46	6	34	178.05
DV16-03B	2	6	3.68	2.56	0.09	12.17	21.75	0.00	21.16	-0.01	38.52	99.93	14	46	6	34	296.75
DV16-03B	2	7	3.59	2.53	0.21	12.36	22.25	0.02	20.64	0.01	38.73	100.34	14	45	6	35	356.1
DV16-03B	2	8	3.60	2.59	0.16	11.91	21.77	-0.01	20.91	0.00	38.59	99.52	14	46	6	34	415.45
DV16-03B	2	9	3.62	2.56	0.15	12.17	22.20	0.04	20.59	-0.01	38.34	99.66	14	46	6	34	474.8
DV16-03B	2	10	3.56	2.49	0.07	12.31	22.05	-0.01	20.95	0.01	38.91	100.35	14	46	6	35	534.15
DV16-03B	2	11	3.61	2.51	0.09	12.31	22.06	0.04	20.90	0.00	39.00	100.51	14	46	6	35	593.5
DV16-03B	2	12	3.68	2.46	0.13	11.78	21.86	0.00	21.30	-0.01	38.83	100.04	14	47	5	33	652.85
DV16-03B	2	13	3.47	2.41	0.10	12.31	22.08	0.01	20.26	0.01	38.74	99.38	14	45	5	35	712.2
DV16-03B	2	14	3.70	2.42	0.09	11.21	22.04	0.00	21.14	0.00	38.38	98.97	15	47	6	32	771.55
DV16-03B	2	15	3.48	2.29	0.07	12.18	21.84	0.01	21.29	0.01	39.04	100.21	14	47	5	34	830.9
DV16-03B	2	16	3.59	2.25	0.19	11.70	21.88	0.02	20.90	0.00	38.88	99.42	14	47	5	34	890.25
DV16-03B	2	17	3.66	2.22	0.10	12.16	22.03	0.01	21.14	0.02	38.87	100.21	14	46	5	34	949.6
DV16-03B	2	18	3.75	2.14	0.06	11.52	21.72	0.00	21.25	0.00	38.43	98.86	15	47	5	33	1008.95
DV16-03B	2	19	3.45	2.02	0.11	12.00	21.75	0.04	20.60	0.01	39.05	99.02	14	47	5	35	1068.3
DV16-03B	2	20	3.89	1.95	0.18	11.80	22.06	0.02	21.65	-0.02	38.82	100.35	15	47	4	33	1127.65
DV16-03B	2	22	3.99	1.71	0.06	11.59	22.22	0.01	22.01	-0.01	38.79	100.37	16	48	4	32	1246.35
DV16-03B	2	23	4.12	1.53	0.05	11.26	22.30	0.05	22.59	-0.01	38.88	100.76	16	49	3	31	1305.7
DV16-03B	2	24	4.22	1.52	0.00	11.01	22.35	0.00	22.54	0.01	38.51	100.17	16	49	3	31	1365.05
DV16-03B	2	25	4.13	1.43	0.06	10.78	22.10	0.00	22.70	0.00	38.26	99.46	16	50	3	30	1424.4

A.2: Raman Peaks

DV16-04B											
Analysis	**Type**	**Garnet zone**	**128**	**RSD (%)**	**R^2**	**206**	**RSD (%)**	**R^2**	**464**	**RSD (%)**	**R^2**
Std1_0830_012022_1	Standard	-	128.5	3.49	0.97351	207	3.461	0.98775	465.4	0.886	0.99762
Gt12_Q1_DV16-04B_0853_012022_1	Sample	rim	130.1	2.31	0.98709	214	3.767	0.98525	467.6	1.018	0.9971
Std2_0911_012022_1	Standard	-	128.2	3.973	0.97387	206.9	3.253	0.98881	465.2	0.871	0.9978
Gt6_Q1_0950_DV16-04B_012022_1	Sample	rim	129.8	2.933	0.98529	213.4	4.302	0.97748	467.3	1.078	0.99701
Std3_1025_012022_1	Standard	-	128.2	3.195	0.98179	206.9	3.47	0.98776	465.1	0.832	0.99765
Gt7_Q4_1049_DV16-04B_012022_1	Sample	mantle	130	1.771	0.99237	214.9	2.831	0.98898	468	1.105	0.99732
Std4_1106_012022_1	Standard	-	128.1	3.207	0.98198	206.9	3.217	0.98874	465.1	0.824	0.99762
Gt5_Q1_DV16-04B_1122_012022_1	Sample	mantle	129.8	1.523	0.99385	215.1	3.351	0.98694	468.2	1.242	0.99666
Std1_0802_110322_1	Standard	-	127.4	3.994	0.97373	206	3.35	0.98878	464.5	0.794	0.99772
Gt8_Q1_DV16-04B_0935_110322_1	Sample	rim	129.3	3.215	0.98619	212.3	3.205	0.98842	466.8	1.335	0.99597

DV16-03B											
Analysis	**Type**	**Garnet zone**	**128**	**RSD (%)**	**R^2**	**206**	**RSD (%)**	**R^2**	**464**	**RSD (%)**	**R^2**
Std3_1039_110322_1	Standard	-	127.6	3.821	0.97768	206.2	3.303	0.98883	464.7	0.84	0.99730
Gt9_Q1_DV16-03B_1114_110322_1	Sample	rim	129.8	1.723	0.99341	213.8	3.007	0.99044	467.2	1.228	0.99543

DV22-12											
Analysis	**Type**	**Garnet zone**	**128**	**RSD (%)**	**R^2**	**206**	**RSD (%)**	**R^2**	**464**	**RSD (%)**	**R^2**
Std1_1544_031223_1	Standard	-	128	3.355	0.98019	206.7	3.177	0.9896	464.9	0.82	0.99761

Q1_DV22-12_1821_031223_1	Sample	core	130.8	1.52	0.99371	216.6	4.029	0.98394	469.1	1.659	0.99532
Std3_2337_031223_1	Standard	-	128.1	3.38	0.9823	206.7	3.274	0.98906	465	0.823	0.99767
Q3_DV22-12_2402_031223_1	Sample	core	130.7	4.31	0.97449	215.7	4.122	0.98264	468.1	1.342	0.99636

CA22-2A-2											
Analysis	**Type**	**Garnet zone**	**128**	**RSD (%)**	**R^2**	**206**	**RSD (%)**	**R^2**	**464**	**RSD (%)**	**R^2**
Std1_1003_080222_1	Standard	-	127.8	3.869	0.97696	206.5	3.387	0.98826	464.8	0.826	0.99797
Q1_CA22-2A-2_1025_080222_2	Sample	core	130.2	1.28	0.99634	215.9	3.404	0.98826	468.3	1.016	0.99736
Std2_1036_080222_1	Standard	-	127.8	3.801	0.97624	206.8	2.834	0.9889	464.9	0.811	0.99784
Q2_CA22-2A-2_1123_080222_1	Sample	rim	130	1.868	0.99272	214.9	2.635	0.99056	468	1.753	0.99424
Std3_1132_080222_1	Standard	-	128	3.537	0.97738	207	2.995	0.98828	465	0.818	0.99775
Q3_CA22-2A-2_1225_080222_1	Sample	core	130.4	4.476	0.97498	216.2	2.187	0.99284	468.3	0.964	0.99746
Std4_1234_080222_1	Standard	-	127.9	3.488	0.97846	206.7	3.195	0.98946	464.9	0.833	0.99766
Q4_CA22-2A-2_1246_080222_1	Sample	core	131.2	2.426	0.99073	218	3.626	0.98713	469.2	1.662	0.99487
Std5_1257_080222_1	Standard	-	127.9	3.345	0.9821	206.7	3.674	0.98666	464.9	0.832	0.99766
Q5_CA22-2A-2_1304_080222_1	Sample	core	130.2	1.559	0.99487	215.8	3.229	0.9858	468.2	0.955	0.9978
Std6_1311_080222_1	Standard	-	127.8	3.423	0.9821	206.6	3.142	0.98827	464.9	0.831	0.99769
Q6_CA22-2A-2_1323_080222_2	Sample	mantle	130.5	1.595	0.99434	216.1	3.62	0.9864	468.3	1.008	0.99765
Std8_1401_080222_1	Standard	-	127.8	3.382	0.98259	206.5	3.256	0.98937	464.8	0.834	0.99785
Q8_CA22-2A-2_1417_080222_1	Sample	rim	129.7	1.284	0.99563	214.9	2.77	0.99061	467.9	1.089	0.99732
Std9_1424_080222_1	Standard	-	127.8	3.511	0.98077	206.6	3.339	0.98874	464.8	0.823	0.99766
Q9_CA22-2A-2_1433_0802088_1	Sample	rim	129.9	2.774	0.98855	214.3	3.189	0.98682	467.8	1.339	0.99654
Std10_1441_080222_1	Standard	-	127.9	3.416	0.98109	206.7	3.225	0.98949	464.9	0.823	0.99768

Q10_CA22-2A-2_1450_080222_1	Sample	core	130.1	1.43	0.99535	215.3	3.295	0.98877	468.1	0.869	0.99742

CA22-3											
Analysis	**Type**	**Garnet zone**	**128**	**RSD (%)**	**R^2**	**206**	**RSD (%)**	**R^2**	**464**	**RSD (%)**	**R^2**
Std1_1704_021223_1	Standard	-	127.8	2.62	0.99064	206.6	2.293	0.99467	464.9	0.963	0.99666
Gt31_Q1_CA22-3_1746_021223_1	Sample	mantle	129	2.038	0.99068	214.8	3.272	0.98858	468	1.164	0.99584
Std2_1802_021223_1	Standard	-	127.5	3.492	0.9797	206.3	3.32	0.98881	464.5	0.821	0.99769
Gt29_Q1_CA22-3_1825_021223_2	Sample	rim	128.4	4.662	0.97	211.4	4.394	0.9818	466.3	1.4	0.99606
Std3_1831_021223_1	Standard	-	127.6	3.385	0.98345	206.3	3.299	0.9888	464.5	0.825	0.99769
Gt22_Q1_CA22-3_1902_021223_1	Sample	mantle	130.8	4.499	0.95493	216.6	4.388	0.98106	468	2.347	0.99200
Std4_1908_021223_1	Standard	-	127.6	3.578	0.97458	206.4	3.261	0.98933	464.6	0.822	0.99767
Gt21_Q1_CA22-3_1944_021223_2	Sample	rim	130.2	2.93	0.98805	215.4	4.602	0.97801	467.6	2.584	0.99094

DV22-4B											
Analysis	**Type**	**Garnet zone**	**128**	**RSD (%)**	**R^2**	**206**	**RSD (%)**	**R^2**	**464**	**RSD (%)**	**R^2**
Std1_1147_080822_1	Standard	-	124.5	3.597	0.97782	203.3	3.373	0.98856	461.7	0.864	0.99753
Gt8_Q1_DV22-4B_1240_080822_1	Sample	rim	126.9	1.657	0.99370	211.8	3.432	0.98770	465	1.197	0.99689
Std2_1250_080822_1	Standard	-	124.6	3.41	0.98088	203.4	3.248	0.98941	461.8	0.934	0.99708
Gt10_Q1_DV22-4B_1326_080822_1	Sample	rim	127.1	1.337	0.99551	212.7	3.578	0.98706	465.2	1.524	0.99564
Std3_1336_080822_1	Standard	-	124.5	3.691	0.98043	203.3	3.28	0.98915	461.7	0.796	0.99786
Gt13_Q1_DV22-4B_1357_080822_1	Sample	rim	126.8	1.858	0.99276	212.9	3.095	0.98959	465.3	1.107	0.99736
Std1_1016_080922_1	Standard	-	127.4	3.445	0.98211	206.1	3.24	0.98911	464.5	0.794	0.99763

Gt25_Q1_DV22-4B_1038_080922_1	Sample	rim	130	1.404	0.99570	215.8	1.897	0.99550	468	0.975	0.99755
Std2_1100_080922_1	Standard	-	127.4	3.589	0.98108	206.2	3.226	0.98936	464.5	0.812	0.99778
Gt27_Q1_DV22-4B_1110_080922_1	Sample	mantle	129.4	1.759	0.99281	214.6	3.887	0.98490	467.7	1.446	0.99599
Std3_1136_080922_2	Standard	-	127.4	3.258	0.98521	206.1	3.225	0.98939	464.5	0.806	0.99777
Gt27_Q2_DV22-4B_1148_080922_1	Sample	rim	129.6	1.579	0.99421	214.9	3.441	0.98110	467.6	1.128	0.99718
Std4_1158_080922_1	Standard	-	127.4	3.386	0.98341	206.1	3.324	0.98906	464.5	0.808	0.99773
Gt27_Q3_DV22-4B_1206_080922_1	Sample	rim	129.7	1.406	0.99556	215.2	3.524	0.98673	467.8	1.388	0.99626

DV22-7											
Analysis	**Type**	**Garnet zone**	**128**	**RSD (%)**	**R^2**	**206**	**RSD (%)**	**R^2**	**464**	**RSD (%)**	**R^2**
Std5_1300_080922_1	Standard	-	127.6	3.35	0.98352	206.4	3.279	0.98903	464.6	0.809	0.99772
Q1_DV22-7_1309_080922_1	Sample	mantle	129.5	1.596	0.99409	214.5	3.387	0.98800	467.5	0.944	0.99803
Std6_1352_080922_1	Standard	-	127.5	3.341	0.98363	206.3	3.312	0.98894	464.6	0.821	0.99765
Q2_DV22-7_1405_080922_2	Sample	core	129.9	1.127	0.99692	215.3	2.4	0.99268	467.8	1.378	0.99639
Std7_1429_080922_1	Standard	-	127.5	3.378	0.98194	206.3	3.208	0.98964	464.6	0.821	0.99770
Q3_DV22-7_1438_080922_1	Sample	core	129.1	2.698	0.98862	211.7	3.273	0.98916	466.3	1.059	0.99732
Std9_1548_080922_1	Standard	-	127.5	3.481	0.98005	206.3	3.292	0.98918	464.5	0.814	0.99770
Q5_DV22-7_1553_080922_1	Sample	rim	129.3	1.387	0.99575	214.2	3.186	0.98958	467.4	1.134	0.99728

A14-50C											
Analysis	**Type**	**Garnet zone**	**128**	**RSD (%)**	**R^2**	**206**	**RSD (%)**	**R^2**	**464**	**RSD (%)**	**R^2**
Std1_1727_030523_4	Standard	-	127.7	3.204	0.98328	206.5	3.227	0.98923	464.7	0.862	0.99751

Q1_A14-50C_1904_030523_1	Sample	mantle	130	2.193	0.98865	214.5	3.679	0.9858	467.9	1.514	0.99572
Std2_1929_030523_1	Standard	-	127.7	3.017	0.98573	206.4	3.219	0.98928	464.7	0.804	0.99776
Q2_A14-50C_2000_030523_3	Sample	core	129.3	5.263	0.95786	213.4	4.202	0.98276	467.3	1.456	0.99434
Std3_2010_030523_2	Standard	-	127.6	3.257	0.9849	206.5	3.373	0.98863	464.6	0.84	0.99757
Q3_A14-50C_2054_030523_1	Sample	core	129.6	1.866	0.99288	214.6	4.598	0.97902	467.7	2.071	0.99188
Std4_2106_030523_1	Standard	-	127.6	3.238	0.985	206.3	3.199	0.98917	464.6	0.792	0.99763
Q4_A14-50C_2134_030523_1	Sample	core	129	2.383	0.98348	211.8	2.876	0.98918	466.4	2.398	0.98293
Std7_2231_030523_1	Standard	-	127.5	3.389	0.97953	206.2	3.202	0.98943	464.5	0.816	0.99770
Q7_A14-50C_2248_030523_1	Sample	core	129.6	1.372	0.99543	214.2	3.986	0.98368	467.3	1.583	0.99513
Std8_2255_030523_1	Standard	-	127.5	3.314	0.98283	206.2	3.26	0.98899	464.5	0.825	0.99764
Q8_A14-50C_2309_030523_1	Sample	core	129.6	1.236	0.99641	214.2	2.19	0.99415	467.5	1.047	0.99744
Std9_2313_030523_1	Standard	-	127.6	3.565	0.97736	206.3	3.253	0.98905	464.5	0.815	0.99764
Q9_A14-50C_2337_030523_1	Sample	rim	129.3	1.88	0.98041	213.6	3.572	0.98558	467.1	1.765	0.99409

Table A.3. QuiG peak shifts and calculated strains, stresses, and inclusion pressures

DV16-04B																							
Analysis Number	**d464**	**esd**	**misfit**	**d206**	**esd**	**misfit**	**d128**	**esd**	**misfit**	**e1+e2**	**esd**	**e3**	**esd**	**Vs**	**esd**	**10E6cv**	**corr %**	**chi2**	**Sigma 1**	**Sigma 2**	**Sigma 3**	**Pinc**	**Unc**
Gt12_Q1	2.267	0.240	-0.148	7.000	0.180	0.009	1.533	0.270	0.233	-108.820	21.605	11.216	14.374	-97.605	7.496	-308.600	-99.400	1.130	-0.495	-0.495	-0.008	0.333	0.016
Gt6_Q1	2.167	0.240	-0.194	6.600	0.180	0.012	1.600	0.270	0.306	-94.376	28.376	4.904	18.879	-89.472	9.846	-532.340	-99.400	1.940	-0.435	-0.435	-0.058	0.309	0.021
Gt7_Q4	2.233	0.240	-0.214	6.600	0.180	0.014	1.700	0.270	0.337	-86.079	31.228	-0.837	20.776	-86.916	10.835	-644.710	-99.400	2.350	-0.403	-0.403	-0.109	0.305	0.023
Gt5_Q1	3.067	0.240	-0.005	8.100	0.180	0.000	1.733	0.270	0.007	-99.917	20.351	-5.148	13.540	-105.070	7.061	-273.820	-99.400	0.000	-0.472	-0.472	-0.171	0.372	0.015

Gt8_Q1	2.300	0.240	-0.264	6.300	0.180	0.017	1.900	0.270	0.416	-60.200	38.535	-15.994	25.638	-76.194	13.371	-981.730	-99.400	3.590	-0.299	-0.299	-0.239	0.279	0.028

DV16-03B																							
Analysis Number	**d464**	**esd**	**misfit**	**d206**	**esd**	**misfit**	**d128**	**esd**	**misfit**	**e1+e2**	**esd**	**e3**	**esd**	**Vs**	**esd**	**10E6cv**	**corr%**	**chi2**	**Sigma 1**	**Sigma 2**	**Sigma 3**	**Pinc**	**Unc**
Gt9_Q1	2.500	0.240	-0.372	7.600	0.180	0.024	2.200	0.270	0.586	-93.568	54.346	-4.740	36.156	-98.308	18.857	-1952.600	-99.400	7.130	-0.442	-0.442	-0.159	0.348	0.040

DV22-12																							
Analysis Number	**d464**	**esd**	**misfit**	**d206**	**esd**	**misfit**	**d128**	**esd**	**misfit**	**e1+e2**	**esd**	**e3**	**esd**	**Vs**	**esd**	**10E6cv**	**corr%**	**chi2**	**Sigma 1**	**Sigma 2**	**Sigma 3**	**Pinc**	**Unc**
Q1	4.200	0.240	-0.139	9.900	0.180	0.009	2.800	0.270	0.220	-65.728	20.372	-45.313	13.554	-111.040	7.069	-274.370	-99.400	1.000	-0.359	-0.359	-0.555	0.425	0.015
Q3	3.100	0.240	-0.391	9.000	0.180	0.025	2.600	0.270	0.617	-102.320	57.176	-11.527	38.040	-113.840	19.839	-2161.300	-99.400	7.890	-0.491	-0.491	-0.241	0.407	0.042

CA22-2A-2																							
Analysis Number	**d464**	**esd**	**misfit**	**d206**	**esd**	**misfit**	**d128**	**esd**	**misfit**	**e1+e2**	**esd**	**e3**	**esd**	**Vs**	**esd**	**10E6cv**	**corr%**	**chi2**	**Sigma 1**	**Sigma 2**	**Sigma 3**	**Pinc**	**Unc**
Q1	3.500	0.240	-0.188	9.400	0.180	0.012	2.400	0.270	0.297	-103.550	27.481	-14.464	18.283	-118.020	9.535	-499.290	-99.400	1.820	-0.500	-0.500	-0.273	0.424	0.020
Q2	3.100	0.240	-0.189	8.100	0.180	0.012	2.200	0.270	0.298	-78.531	27.634	-19.868	18.385	-98.399	9.588	-504.870	-99.400	1.840	-0.389	-0.389	-0.301	0.360	0.020
Q3	3.300	0.240	-0.248	9.200	0.180	0.016	2.400	0.270	0.391	-107.070	36.199	-10.151	24.083	-117.220	12.560	-866.310	-99.400	3.160	-0.511	-0.511	-0.232	0.418	0.026
Q4	4.300	0.240	-0.369	11.300	0.180	0.023	3.300	0.270	0.582	-101.550	53.917	-33.209	35.871	-134.750	18.708	-1921.900	-99.400	7.020	-0.512	-0.512	-0.469	0.498	0.039
Q5	3.300	0.240	-0.202	9.100	0.180	0.013	2.300	0.270	0.318	-106.730	29.511	-9.499	19.634	-116.230	10.240	-575.780	-99.400	2.100	-0.509	-0.509	-0.225	0.414	0.022

Q6	3.400	0.240	-0.351	9.500	0.180	0.022	2.700	0.270	0.554	-101.870	51.345	-16.457	34.160	-118.320	17.816	-1742.900	-99.400	6.370	-0.494	-0.494	-0.292	0.427	0.038
Q8	3.100	0.240	-0.075	8.400	0.180	0.005	1.900	0.270	0.118	-104.390	20.351	-4.765	13.540	-109.150	7.061	-273.820	-99.400	0.290	-0.493	-0.493	-0.172	0.386	0.015
Q9	3.000	0.240	-0.165	7.700	0.180	0.011	2.100	0.270	0.261	-70.983	24.189	-21.440	16.093	-92.422	8.393	-386.830	-99.400	1.410	-0.356	-0.356	-0.309	0.340	0.018
Q10	3.200	0.240	-0.175	8.600	0.180	0.011	2.200	0.270	0.275	-94.697	25.508	-13.262	16.971	-107.960	8.851	-430.160	-99.400	1.570	-0.457	-0.457	-0.250	0.388	0.019

CA22-3

Analysis Number	d464	esd	misfit	d206	esd	misfit	d128	esd	misfit	e1+e2	esd	e3	esd	Vs	esd	10E6cv	corr %	chi2	Sigma 1	Sigma 2	Sigma 3	Pinc	Unc
Gt31_Q1	3.500	0.240	0.361	8.200	0.180	-0.023	1.200	0.270	-0.569	-99.417	52.772	-6.628	35.110	-106.050	18.311	-1841.200	-99.400	6.720	-0.472	-0.472	-0.186	0.376	0.039
Gt29_Q1	1.800	0.240	0.033	5.100	0.180	-0.002	0.900	0.270	-0.053	-78.993	20.351	7.888	13.540	-71.105	7.061	-273.820	-99.400	0.060	-0.359	-0.359	-0.009	0.243	0.015
Gt22_Q1	3.500	0.240	-0.558	10.300	0.180	0.036	3.200	0.270	0.880	-110.790	81.542	-17.498	54.250	-128.290	28.293	-4395.800	-99.400	16.100	-0.537	-0.537	-0.314	0.463	0.060
Gt21_Q1	3.000	0.240	-0.425	9.000	0.180	0.027	2.600	0.270	0.670	-108.560	62.093	-7.180	41.311	-115.740	21.545	-2549.000	-99.400	9.310	-0.515	-0.515	-0.203	0.411	0.045

DV22-4B

Analysis Number	d464	esd	misfit	d206	esd	misfit	d128	esd	misfit	e1+e2	esd	e3	esd	Vs	esd	10E6cv	corr %	chi2	Sigma 1	Sigma 2	Sigma 3	Pinc	Unc
Gt8_Q1	3.300	0.240	-0.221	8.500	0.180	0.014	2.400	0.270	0.348	-75.701	32.292	-25.486	21.484	-101.190	11.205	-689.410	-99.400	2.520	-0.383	-0.383	-0.357	0.374	0.024
Gt10_Q1	3.500	0.240	-0.272	9.400	0.180	0.017	2.600	0.270	0.429	-95.280	39.741	-20.151	26.440	-115.430	13.789	-1044.100	-99.400	3.810	-0.468	-0.468	-0.324	0.420	0.029
Gt13_Q1	3.600	0.240	-0.120	9.600	0.180	0.008	2.300	0.270	0.189	-110.410	20.351	-11.586	13.540	-122.000	7.061	-273.820	-99.400	0.740	-0.529	-0.529	-0.251	0.436	0.015
Gt25_Q1	3.500	0.240	-0.283	9.700	0.180	0.018	2.600	0.270	0.447	-108.720	41.415	-13.580	27.554	-122.300	14.370	-1134.000	-99.400	4.140	-0.523	-0.523	-0.270	0.439	0.030

Gt27_Q1	3.200	0.240	-0.083	8.400	0.180	0.005	2.000	0.270	0.131	-94.008	20.351	-11.955	13.540	-105.960	7.061	-273.820	-99.400	0.360	-0.452	-0.452	-0.236	0.380	0.015
Gt27_Q2	3.100	0.240	-0.216	8.800	0.180	0.014	2.200	0.270	0.340	-109.900	31.541	-4.534	20.984	-114.440	10.944	-657.710	-99.400	2.400	-0.518	-0.518	-0.176	0.404	0.023
Gt27_Q3	3.300	0.240	-0.202	9.100	0.180	0.013	2.300	0.270	0.318	-106.730	29.511	-9.499	19.634	-116.230	10.240	-575.780	-99.400	2.100	-0.509	-0.509	-0.225	0.414	0.022

DV22-7																							
Analysis Number	**d464**	**esd**	**misfit**	**d206**	**esd**	**misfit**	**d128**	**esd**	**misfit**	**e1+e2**	**esd**	**e3**	**esd**	**Vs**	**esd**	**10E6cv**	**corr %**	**chi2**	**Sigma 1**	**Sigma 2**	**Sigma 3**	**Pinc**	**Unc**
Q1	2.900	0.150	-0.102	8.100	0.320	0.052	1.900	0.200	0.225	-104.040	25.161	-1.807	14.711	-105.850	10.951	-364.790	-98.600	1.750	-0.486	-0.486	-0.149	0.372	0.028
Q2	3.200	0.150	-0.213	9.000	0.320	0.110	2.400	0.200	0.472	-105.650	52.750	-8.433	30.843	-114.090	22.958	-1603.400	-98.600	7.700	-0.499	-0.499	-0.230	0.406	0.058
Q3	1.700	0.150	-0.238	5.400	0.320	0.123	1.600	0.200	0.526	-71.175	58.849	0.857	34.409	-70.317	25.612	-1995.600	-98.600	9.580	-0.327	-0.327	-0.093	0.245	0.065
Q5	2.900	0.150	-0.063	7.900	0.320	0.033	1.800	0.200	0.140	-98.981	19.014	-3.663	11.117	-102.640	8.275	-208.320	-98.600	0.670	-0.465	-0.465	-0.160	0.362	0.021

A14-50C																							
Analysis Number	**d464**	**esd**	**misfit**	**d206**	**esd**	**misfit**	**d128**	**esd**	**misfit**	**e1+e2**	**esd**	**e3**	**esd**	**Vs**	**esd**	**10E6cv**	**corr %**	**chi2**	**Sigma 1**	**Sigma 2**	**Sigma 3**	**Pinc**	**Unc**
Q1	3.200	0.240	-0.194	8.000	0.180	0.012	2.300	0.270	0.305	-63.671	28.289	-29.249	18.821	-92.921	9.816	-529.070	-99.400	1.930	-0.331	-0.331	-0.383	0.348	0.021
Q2	2.600	0.240	-0.064	7.000	0.180	0.004	1.600	0.270	0.100	-85.260	20.351	-5.169	13.540	-90.429	7.061	-273.820	-99.400	0.210	-0.404	-0.404	-0.154	0.320	0.015
Q3	3.100	0.240	-0.105	8.100	0.180	0.007	2.000	0.270	0.166	-86.805	20.351	-14.181	13.540	-100.990	7.061	-273.820	-99.400	0.570	-0.421	-0.421	-0.251	0.365	0.015
Q4	1.800	0.240	-0.192	5.500	0.180	0.012	1.400	0.270	0.302	-76.236	28.006	2.432	18.633	-73.803	9.717	-518.560	-99.400	1.890	-0.353	-0.353	-0.063	0.256	0.020
Q7	2.800	0.240	-0.244	8.000	0.180	0.016	2.100	0.270	0.385	-96.909	35.697	-6.174	23.750	-103.080	12.386	-842.470	-99.400	3.080	-0.459	-0.459	-0.178	0.366	0.026

Q8	3.000	0.240	-0.177	8.000	0.180	0.011	2.100	0.270	0.279	-84.427	25.864	-14.868	17.207	-99.295	8.974	-442.240	-99.400	1.620	-0.411	-0.411	-0.255	0.359	0.019
Q9	2.600	0.240	-0.117	7.300	0.180	0.007	1.700	0.270	0.185	-94.568	20.351	-1.441	13.540	-96.008	7.061	-273.820	-99.400	0.710	-0.443	-0.443	-0.125	0.337	0.015

Appendix B: Rutile Geochemistry

DV16-04B														
Grain[a]	**Analysis**	**TiO_2**	**ZrO_2**	**Al_2O_3**	**FeO**	**Nb_2O_5**	**SiO_2**	**MnO**	**Ta_2O_5**	**Total**	**Zr Unc (%)**	**Zr (ppm)**	**Zr Unc (ppm, 2σ)**	**Si (ppm)**
14	1	99.57	0.0368	0.15	0.06	0.28	0.00	0.00	0.00	100.03	6.59	272	36	[b]B.D.
14	2	99.36	0.0521	0.17	0.05	0.33	0.00	0.04	0.01	100.01	4.64	386	36	B.D.
13	1	99.52	0.0561	0.15	0.06	0.37	0.00	0.00	0.05	100.18	4.67	415	39	B.D.
13	2	99.80	0.0575	0.16	0.08	0.33	0.00	0.00	0.01	100.43	4.65	426	40	B.D.
12	1	99.50	0.0400	0.15	0.25	0.29	0.00	0.00	0.00	100.16	6.48	296	38	B.D.
12	2	99.25	0.0456	0.17	0.12	0.35	0.00	0.00	0.01	99.92	5.24	338	35	B.D.
28 (grt)	1	98.83	0.0300	0.15	0.77	0.21	0.01	0.02	0.00	99.91	9.21	222	41	B.D.
28 (grt)	2	97.82	0.0333	0.15	0.66	0.21	0.00	0.00	0.07	98.94	7.58	247	37	B.D.
29 (grt)	1	98.37	0.0519	0.15	0.86	0.69	0.00	0.00	0.01	100.11	4.77	384	37	B.D.
29 (grt)	2	98.72	0.0463	0.16	0.83	0.72	0.01	0.02	0.02	100.52	5.5	343	38	B.D.
10	1	99.57	0.0488	0.14	0.20	0.35	0.00	0.02	0.00	100.29	5.3	361	38	B.D.
10	2	99.66	0.0441	0.16	0.16	0.29	0.00	0.02	0.00	100.20	5.7	326	37	B.D.
8	1	98.88	0.0501	0.16	0.13	0.36	0.00	0.00	0.06	99.61	5.29	371	39	B.D.
8	2	98.92	0.0510	0.17	0.10	0.37	0.00	0.02	0.00	99.56	5.22	378	39	B.D.
15	1	100.00	0.0466	0.16	0.17	0.35	0.00	0.03	0.00	100.68	5.32	345	37	B.D.
15	2	99.68	0.0525	0.15	0.18	0.41	0.00	0.01	0.02	100.48	4.27	389	33	B.D.
30 (grt)	1	98.88	0.0442	0.18	0.71	0.31	0.00	0.03	0.00	100.09	5.17	327	34	B.D.
30 (grt)	2	99.26	0.0467	0.18	0.58	0.26	0.00	0.00	0.00	100.31	5.5	346	38	B.D.
31 (grt)	1	98.50	0.0607	0.18	0.89	0.72	0.01	0.00	0.07	100.41	4.22	449	38	B.D.
31 (grt)	2	98.54	0.0546	0.16	0.96	0.72	0.00	0.02	0.03	100.48	5.07	404	41	B.D.
17	1	98.52	0.0578	0.15	0.21	0.50	0.00	0.00	0.00	99.39	4.54	428	39	B.D.
17	2	99.84	0.0590	0.16	0.19	0.44	0.00	0.00	0.00	100.65	4.49	437	39	B.D.
32 (grt)	1	99.31	0.0325	0.14	0.34	0.27	0.00	0.02	0.00	100.05	7.94	241	38	B.D.
32 (grt)	2	99.50	0.0359	0.16	0.33	0.28	0.00	0.00	0.01	100.28	6.69	266	36	B.D.

19	1	100.17	0.0400	0.17	0.19	0.41	0.00	0.02	0.03	101.00	5.79	296	34	B.D.
19	2	98.23	0.0455	0.16	0.20	0.48	0.00	0.00	0.15	99.24	6.12	337	41	B.D.
18	1	99.96	0.0487	0.15	0.13	0.34	0.00	0.02	0.05	100.68	5.29	361	38	B.D.
18	2	99.88	0.0471	0.17	0.16	0.30	0.00	0.00	0.00	100.48	5.34	349	37	B.D.
20	1	99.45	0.0371	0.17	0.11	0.28	0.00	0.00	0.00	100.02	7.32	275	40	B.D.
20	2	98.94	0.0266	0.16	0.15	0.24	0.00	0.00	0.00	99.45	10.74	197	42	B.D.
21	1	100.08	0.0423	0.15	0.12	0.33	0.00	0.01	0.02	100.76	6.1	313	38	B.D.
21	2	99.09	0.0528	0.15	0.13	0.40	0.00	0.00	0.00	99.75	4.54	391	35	B.D.
32 (grt)	1	99.43	0.0522	0.16	0.72	0.22	0.00	0.00	0.00	100.51	5.28	386	41	B.D.
7	1	99.24	0.0264	0.18	0.16	0.36	0.00	0.00	0.04	99.97	10.43	195	41	B.D.
7	2	100.02	0.0480	0.18	0.17	0.35	0.00	0.04	0.00	100.78	5.22	355	37	B.D.
33	1	98.90	0.0318	0.15	0.20	0.35	0.00	0.00	0.05	99.66	9.27	235	44	B.D.
33	2	98.75	0.0458	0.16	0.24	0.40	0.00	0.01	0.03	99.61	5.81	339	39	B.D.
34	1	99.96	0.0401	0.15	0.19	0.42	0.00	0.06	0.00	100.79	6.58	297	39	B.D.
34	2	97.96	0.0394	0.15	0.22	0.40	0.00	0.00	0.00	98.66	6.13	292	36	B.D.
23	1	99.47	0.0536	0.15	0.23	0.40	0.00	0.04	0.03	100.37	4.57	397	36	B.D.
23	2	99.21	0.0499	0.17	0.14	0.38	0.00	0.01	0.00	99.88	5.12	369	38	B.D.
35	2	98.76	0.0489	0.14	0.16	0.34	0.00	0.00	0.01	99.40	5.43	362	39	B.D.
36 (grt)	1	98.22	0.0548	0.16	0.90	0.82	0.00	0.00	0.03	100.17	4.79	406	39	B.D.
6	1	99.89	0.0416	0.14	0.13	0.27	0.00	0.00	0.00	100.38	6.53	308	40	B.D.
6	2	99.56	0.0404	0.15	0.14	0.28	0.00	0.00	0.00	100.11	6.37	299	38	B.D.
2	1	99.13	0.0431	0.15	0.14	0.36	0.00	0.01	0.00	99.80	5.86	319	37	B.D.
2	2	99.25	0.0446	0.14	0.11	0.32	0.00	0.00	0.03	99.86	6.06	330	40	B.D.
37 (grt)	1	97.57	0.0491	0.20	0.98	0.71	0.04	0.00	0.12	99.68	5.9	363	43	208
25	1	99.63	0.0370	0.17	0.12	0.25	0.00	0.00	0.00	100.11	7.21	274	39	B.D.
25	1	99.81	0.0387	0.16	0.13	0.21	0.00	0.02	0.00	100.30	7.72	286	44	B.D.

[a] (grt) indicates grain was an inclusion in garnet.

[b] B.D. indicates below EPMA detection limit (same for all tables in section).

DV16-03B														
Grain	**Analysis**	**TiO_2**	**ZrO_2**	**Al_2O_3**	**FeO**	**Nb_2O_5**	**SiO_2**	**MnO**	**Ta_2O_5**	**Total**	**Zr Unc (%)**	**Zr (ppm)**	**Zr Unc (ppm, 2σ)**	**Si (ppm)**
6	1	98.54	0.0674	0.27	0.39	0.43	0.00	0.00	0.00	99.61	3.97	499	40	B.D.
6	2	99.34	0.0648	0.23	0.51	0.38	0.00	0.03	0.04	100.58	3.98	480	38	B.D.
7	1	99.26	0.0666	0.22	0.45	0.53	0.00	0.00	0.07	100.54	3.81	493	38	B.D.
7	2	98.53	0.0607	0.30	0.33	0.54	0.00	0.00	0.01	99.76	4.35	449	39	B.D.
10	1	99.20	0.0635	0.17	0.49	0.52	0.00	0.00	0.06	100.45	4.13	470	39	B.D.
10	2	99.37	0.0689	0.16	0.52	0.50	0.00	0.00	0.09	100.67	3.74	510	38	B.D.
2	1	98.67	0.0571	0.78	0.50	0.50	0.00	0.04	0.00	100.50	4.4	423	37	B.D.
2	2	99.27	0.0545	0.20	0.47	0.49	0.00	0.00	0.03	100.49	4.71	403	38	B.D.
18	1	99.64	0.0197	0.17	0.35	0.53	0.06	0.00	0.08	100.84	14.32	146	42	258
12	2	98.98	0.0732	0.19	0.53	0.47	0.00	0.00	0.00	100.22	3.48	542	38	B.D.
13	1	98.74	0.0677	0.18	0.61	0.48	0.00	0.00	0.00	100.03	3.64	501	36	B.D.
15	1	99.13	0.0226	0.21	0.40	0.65	0.00	0.00	0.00	100.40	10.26	167	34	B.D.
15	2	98.94	0.0227	0.21	0.39	0.64	0.00	0.00	0.08	100.28	11.83	168	40	B.D.
17	1	99.56	0.0188	0.19	0.43	0.40	0.01	0.00	0.00	100.57	13.06	139	36	B.D.
17	2	99.65	0.0231	0.19	0.43	0.40	0.00	0.00	0.00	100.68	12.01	171	41	B.D.
16	1	99.26	0.0485	0.20	0.41	0.69	0.01	0.00	0.05	100.65	5.03	359	36	B.D.

DV22-4B															
Grain[a]	**Analysis**	**TiO_2**	**ZrO_2**	**Al_2O_3**	**FeO**	**Nb_2O_5**	**SiO_2**	**MnO**	**Ta_2O_5**	**V_2O_3**	**Total**	**Zr Unc (%)**	**Zr (ppm)**	**Zr Unc (ppm, 2σ)**	**Si (ppm)**
1	1	97.43	0.0569	0.08	0.12	0.19	0.00	0.02	0.11	0.59	98.59	10.76	421	91	B.D.
1	2	97.94	0.0566	0.10	0.21	0.28	0.00	0.02	0.07	0.72	99.37	8.91	419	75	B.D.
2 (grt)	1	98.34	0.0532	0.18	0.73	0.34	0.00	0.00	0.01	0.46	100.08	10.82	394	85	B.D.
3	1	98.47	0.0595	0.13	0.02	0.20	0.00	0.00	0.00	0.70	99.45	9.5	440	84	B.D.

3	2	98.41	0.0517	0.10	0.13	0.13	0.00	0.14	0.01	0.63	99.60	9.41	383	72	B.D.
5 (grt)	1	97.55	0.0490	0.12	0.92	0.13	0.00	0.02	0.00	0.58	99.30	12.24	363	89	B.D.
6	1	99.68	0.0475	0.10	0.04	0.26	0.00	0.00	0.15	0.57	100.79	10.02	352	70	B.D.
6	2	98.01	0.0621	0.10	0.12	0.20	0.00	0.00	0.01	0.55	98.96	8.89	460	82	B.D.
7	1	97.79	0.0379	0.11	0.09	0.27	0.00	0.00	0.00	0.65	98.75	15.19	281	85	B.D.
7	2	97.93	0.0464	0.09	0.16	0.23	0.00	0.00	0.02	0.51	98.94	10.62	344	73	B.D.
9	1	98.63	0.0495	0.12	0.12	0.32	0.02	0.02	0.00	0.59	99.78	11.92	366	87	95
9	2	97.09	0.0525	0.13	0.10	0.32	0.00	0.00	0.00	0.66	98.28	11.73	389	91	B.D.
11 (grt)	1	98.18	0.0554	0.13	0.55	0.31	0.00	0.00	0.04	0.64	99.86	9.55	410	78	B.D.
11 (grt)	2	98.40	0.0539	0.13	0.64	0.26	0.00	0.01	0.00	0.62	100.09	10.07	399	80	B.D.
12	1	98.57	0.0462	0.11	0.08	0.23	0.00	0.01	0.06	0.65	99.74	11.69	342	80	B.D.
12	2	98.41	0.0290	0.08	0.11	0.31	0.00	0.00	0.00	0.63	99.40	13.33	215	57	B.D.
13 (grt)	1	98.16	0.0655	0.18	1.11	0.62	0.00	0.09	0.04	0.52	100.77	8.25	485	80	B.D.
14	1 (rim)	98.71	0.0374	0.13	0.00	0.15	0.00	0.05	0.03	0.63	99.71	11.99	277	66	B.D.
14	2 (core)	99.53	0.0574	0.13	0.07	0.21	0.00	0.00	0.01	0.59	100.56	9.83	425	84	B.D.
14	3 (rim)	99.24	0.0458	0.09	0.18	0.24	0.00	0.04	0.00	0.61	100.43	14.05	339	95	B.D.
15	1	98.54	0.0331	0.13	0.07	0.22	0.00	0.05	0.00	0.73	99.74	15.8	245	77	B.D.
19 (grt)	1	96.77	0.0600	0.09	0.20	0.39	0.00	0.01	0.04	0.75	98.31	10.83	444	96	B.D.
19 (grt)	2	98.54	0.0471	0.12	0.16	0.31	0.00	0.00	0.00	0.76	99.82	10.79	349	75	B.D.
16 (grt)	1	96.43	0.0364	0.27	1.47	1.63	0.01	0.00	0.04	0.32	100.16	15.28	269	82	B.D.
17	1	98.81	0.0509	0.12	0.00	0.21	0.00	0.07	0.03	0.76	99.99	8.8	377	66	B.D.
18	1	98.53	0.0463	0.11	0.17	0.19	0.01	0.00	0.22	0.69	99.96	12.95	343	89	B.D.

[a] (grt) indicates grain was an inclusion in garnet.

DV22-7															
Grain[a]	**Analysis**	**TiO_2**	**ZrO_2**	**Al_2O_3**	**FeO**	**Nb_2O_5**	**SiO_2**	**MnO**	**Ta_2O_5**	**V_2O_3**	**Total**	**Zr Unc (%)**	**Zr (ppm)**	**Zr Unc (ppm, 2σ)**	**Si (ppm)**
1 (grt)	1	96.95	0.0500	0.15	0.70	0.11	0.00	0.08	0.00	0.29	98.31	4.96	370	37	B.D.
2	1	98.83	0.0567	0.15	0.10	0.34	0.00	0.03	0.04	0.81	100.34	4.32	420	36	B.D.

2	2	99.59	0.0592	0.14	0.05	0.35	0.00	0.02	0.00	0.80	100.97	4.17	438	37	B.D.
3	1	98.25	0.0503	0.14	0.09	0.38	0.00	0.02	0.00	0.91	99.81	5.08	372	38	B.D.
3	2	98.36	0.0458	0.14	0.12	0.54	0.00	0.01	0.03	0.83	100.06	5.45	339	37	B.D.
4	1	98.77	0.0559	0.13	0.12	0.33	0.00	0.00	0.05	0.87	100.31	4.71	414	39	B.D.
4	2	98.45	0.0606	0.14	0.09	0.33	0.00	0.00	0.04	0.79	99.85	4.11	449	37	B.D.
5	1	98.18	0.0604	0.14	0.13	0.36	0.00	0.00	0.06	0.74	99.65	4.51	447	40	B.D.
7	1	98.42	0.0598	0.14	0.08	0.40	0.00	0.00	0.03	0.91	100.03	3.99	443	35	B.D.
7	2	98.86	0.0588	0.15	0.12	0.35	0.00	0.00	0.05	0.93	100.49	4.19	435	36	B.D.
8 (grt)	1	98.90	0.0591	0.14	0.23	0.38	0.00	0.03	0.07	0.74	100.55	4.32	438	38	B.D.
8 (grt)	2	99.60	0.0604	0.15	0.25	0.40	0.00	0.02	0.00	0.71	101.15	4.28	447	38	B.D.
9 (grt)	1	98.12	0.0569	0.13	0.15	0.44	0.00	0.01	0.00	0.82	99.71	4.19	421	35	B.D.
9 (grt)	2	98.96	0.0589	0.14	0.21	0.41	0.00	0.04	0.02	0.84	100.65	4.28	436	37	B.D.
10 (grt)	1	98.35	0.0572	0.15	0.32	0.42	0.00	0.03	0.00	0.83	100.05	4.66	423	39	B.D.
10 (grt)	2	98.33	0.0585	0.14	0.29	0.38	0.00	0.03	0.00	0.79	99.97	4.47	433	39	B.D.
11 (grt)	1	98.77	0.0622	0.15	0.50	0.26	0.00	0.07	0.00	0.73	100.54	4.33	460	40	B.D.
11 (grt)	2	98.90	0.0571	0.15	0.47	0.21	0.00	0.05	0.00	0.72	100.47	4.39	423	37	B.D.
12 (grt)	1	98.98	0.0609	0.13	0.40	0.22	0.00	0.03	0.00	0.55	100.30	3.86	451	35	B.D.
12 (grt)	2	99.13	0.0579	0.16	0.36	0.21	0.00	0.05	0.04	0.55	100.53	4.26	429	37	B.D.
13	1	99.12	0.0586	0.15	0.08	0.36	0.00	0.00	0.00	0.83	100.58	4.54	434	39	B.D.
13	2	98.22	0.0521	0.14	0.13	0.35	0.00	0.01	0.02	0.78	99.68	5	386	39	B.D.
14 (grt)	1	97.86	0.0519	0.17	0.38	0.24	0.00	0.05	0.00	0.77	99.48	4.64	384	36	B.D.
14 (grt)	2	97.22	0.0503	0.18	0.34	0.26	0.00	0.03	0.00	0.73	98.74	5.03	372	37	B.D.
15	1	98.10	0.0567	0.14	0.10	0.33	0.00	0.00	0.03	0.86	99.58	4.48	420	38	B.D.
15	2	96.92	0.0546	0.16	0.15	0.37	0.00	0.01	0.00	0.85	98.50	5.14	404	42	B.D.
16	1	97.48	0.0567	0.15	0.19	0.50	0.00	0.00	0.00	0.85	99.14	4.53	420	38	B.D.
16	2	97.12	0.0611	0.14	0.19	0.97	0.00	0.00	0.00	0.96	99.41	4.23	452	38	B.D.
16	3	99.53	0.0594	0.14	0.16	0.49	0.00	0.01	0.00	0.88	101.21	4.27	440	38	B.D.
17	1	98.92	0.0492	0.16	0.15	0.38	0.00	0.00	0.08	0.81	100.51	5.2	364	38	B.D.
17	2	98.30	0.0578	0.15	0.13	0.39	0.00	0.01	0.04	0.83	99.90	4.37	428	37	B.D.
18	1	97.61	0.0461	0.14	0.05	0.37	0.00	0.01	0.00	0.89	99.07	5.12	341	35	B.D.
18	2	98.63	0.0571	0.15	0.09	0.34	0.00	0.00	0.00	0.84	100.09	4.62	423	39	B.D.

[a] (grt) indicates grain was an inclusion in garnet.

CA22-2A-2															
Grain	**Analysis**	**TiO_2**	**ZrO_2**	**Al_2O_3**	**FeO**	**Nb_2O_5**	**SiO_2**	**MnO**	**Ta_2O_5**	**V_2O_3**	**Total**	**Zr Unc (%)**	**Zr (ppm)**	**Zr Unc (ppm, 2σ)**	**Si (ppm)**
1	1	97.50	0.0550	0.11	0.59	0.64	0.00	0.01	0.00	0.46	99.34	4.78	407	39	B.D.
2	1	98.09	0.0540	0.10	0.56	0.74	0.00	0.02	0.00	0.65	100.20	4.62	400	37	B.D.
2	2	98.20	0.0495	0.10	0.53	0.70	0.00	0.02	0.13	0.66	100.38	5.36	366	39	B.D.
3	1	98.58	0.0590	0.11	0.50	0.19	0.00	0.02	0.01	0.32	99.76	4.49	437	39	B.D.
4	1	98.06	0.0479	0.12	0.59	0.57	0.00	0.04	0.00	0.42	99.81	5.16	355	37	B.D.
4	2	96.78	0.0418	0.13	0.57	0.56	0.00	0.03	0.06	0.45	98.61	5.38	309	33	B.D.
5	1	97.05	0.0607	0.12	0.56	0.23	0.00	0.06	0.00	0.31	98.34	3.96	449	36	B.D.
5	2	98.67	0.0515	0.11	0.54	0.21	0.00	0.02	0.04	0.32	99.95	4.67	381	36	B.D.
6	1	98.55	0.0597	0.13	0.59	0.27	0.00	0.00	0.07	0.35	100.01	4.34	442	38	B.D.
6	2	98.38	0.0527	0.13	0.49	0.28	0.00	0.02	0.00	0.36	99.67	4.33	390	34	B.D.
7	1	97.38	0.0531	0.12	0.54	0.39	0.02	0.00	0.00	0.30	98.75	4.83	393	38	79
7	2	98.84	0.0505	0.12	0.52	0.40	0.01	0.01	0.03	0.29	100.28	4.77	374	36	B.D.
8	1	98.87	0.0486	0.13	0.44	0.42	0.00	0.00	0.03	0.38	100.29	5.17	360	37	B.D.
8	2	96.56	0.0577	0.13	0.47	0.44	0.00	0.02	0.02	0.37	98.05	4.26	427	36	B.D.
9	1	98.85	0.0444	0.13	0.57	0.48	0.00	0.03	0.00	0.33	100.40	5.55	329	36	B.D.
9	2	97.37	0.0504	0.12	0.60	0.48	0.00	0.02	0.00	0.33	98.85	5.14	373	38	B.D.
10	1	98.43	0.0605	0.11	0.57	0.61	0.00	0.01	0.00	0.60	100.34	4.31	448	39	B.D.
10	2	98.24	0.0493	0.12	0.54	0.59	0.00	0.01	0.04	0.65	100.20	4.85	365	35	B.D.
11	1	98.03	0.0481	0.11	0.44	0.21	0.00	0.02	0.07	0.32	99.25	5.07	356	36	B.D.
11	2	98.65	0.0552	0.13	0.51	0.23	0.00	0.00	0.07	0.34	99.93	4.58	409	37	B.D.
12	1	98.98	0.0547	0.11	0.48	0.23	0.00	0.02	0.05	0.32	100.24	4.32	405	35	B.D.
12	2	98.96	0.0569	0.11	0.44	0.21	0.00	0.02	0.06	0.36	100.20	4.43	421	37	B.D.
13	2	98.75	0.0552	0.14	0.57	0.57	0.00	0.04	0.00	0.48	100.59	4.63	409	38	B.D.
14	1	97.11	0.0488	0.14	0.62	0.52	0.00	0.04	0.00	0.55	99.01	5.45	361	39	B.D.

15	1	98.66	0.0434	0.15	0.65	0.51	0.02	0.04	0.00	0.45	100.50	5.55	321	36	113
15	2	98.83	0.0508	0.16	0.56	0.53	0.02	0.06	0.02	0.49	100.72	4.67	376	35	116

Rutile traverse of matrix grain #23 in DV16-04B

Analysis	**Distance from rim (µm)**	**TiO_2**	**ZrO_2**	**Al_2O_3**	**FeO**	**Nb_2O_5**	**SiO_2**	**MnO**	**Ta_2O_5**	**Total**	**Zr Unc (%)**	**Zr (ppm)**	**Zr Unc (ppm, 2σ)**	**Si (ppm)**
1	0.00	99.20	0.0503	0.15	0.18	0.34	0.00	0.00	0.00	99.86	5.61	372	42	B.D.
2	10.30	99.55	0.0529	0.19	0.19	0.35	0.00	0.00	0.00	100.26	5.07	392	40	B.D.
3	20.59	97.92	0.0473	0.15	0.17	0.34	0.00	0.04	0.04	98.67	5.95	350	42	B.D.
4	30.89	98.48	0.0518	0.15	0.19	0.35	0.00	0.00	0.00	99.17	5.16	383	40	B.D.
5	41.18	99.52	0.0529	0.16	0.19	0.33	0.00	0.00	0.04	100.25	4.83	392	38	B.D.
6	51.48	99.37	0.0570	0.17	0.16	0.36	0.00	0.03	0.00	100.12	4.2	422	35	B.D.
7	61.77	99.11	0.0512	0.17	0.17	0.36	0.00	0.00	0.07	99.90	4.71	379	36	B.D.
8	72.07	98.47	0.0518	0.16	0.18	0.32	0.00	0.00	0.00	99.15	4.93	383	38	B.D.
9	82.36	99.49	0.0474	0.16	0.22	0.28	0.00	0.00	0.00	100.16	5.65	351	40	B.D.
10	92.66	99.08	0.0205	0.17	0.31	0.24	0.01	0.00	0.00	99.80	11.71	152	36	B.D.

Appendix C: Amphibole Geochemistry

Table C.1. Amphibole EPMA analyses (in wt. %), with uncertainty in counting statistics.

Sample	Grain	Position	Na_2O	MnO	TiO_2	Cl	F	MgO	FeO	CaO	Al_2O_3	K_2O	SiO_2	Total	Ti Unc (%)	Ti (apfu)	Ti Unc (apfu, 2σ)
CA15-02B	01	core	0.96	0.13	0.23	0.00	0.00	17.77	6.87	12.77	7.69	0.02	51.18	97.66	17.55	0.024	0.008
CA15-02B	01	rim	0.57	0.13	0.18	0.01	0.02	15.02	7.06	12.65	9.01	0.05	49.17	93.88	21.99	0.019	0.009
CA15-02B	02	core	1.09	0.17	0.25	0.00	0.00	17.81	6.66	12.42	6.60	0.01	51.70	96.76	15.12	0.027	0.008
CA15-02B	02	rim	0.95	0.19	0.12	0.00	0.00	17.47	6.88	12.39	6.37	0.04	52.51	96.94	32.7	0.013	0.009
CA15-02B	03	core	0.89	0.15	0.19	0.00	0.00	17.83	6.52	12.68	7.08	0.00	51.48	96.85	21.48	0.020	0.009
CA15-02B	03	rim	0.57	0.15	0.11	0.00	0.02	19.69	5.88	12.64	2.90	0.05	55.24	97.27	30.91	0.012	0.007
CA15-02B	04	core	1.02	0.18	0.27	0.02	0.11	17.19	6.74	12.45	7.39	0.02	50.92	96.36	14.81	0.029	0.009
CA15-02B	04	rim	0.18	0.20	0.06	0.00	0.00	19.80	6.32	13.07	1.10	0.02	56.45	97.21	61	0.006	0.007
CA15-02B	05	core	0.60	0.19	0.05	0.01	0.00	18.86	7.22	12.73	3.23	0.01	54.08	96.98	79.04	0.005	0.008
CA15-02B	05	rim	1.06	0.12	0.28	0.02	0.09	16.37	6.77	12.05	8.97	0.05	49.11	94.94	13.11	0.031	0.008
CA15-02B	07	core	1.06	0.15	0.19	0.00	0.10	17.12	6.76	12.30	6.99	0.01	50.04	94.75	22.42	0.020	0.009
CA15-02B	07	rim	1.03	0.20	0.24	0.00	0.00	17.34	6.91	12.58	7.21	0.00	51.74	97.29	15.9	0.025	0.008
CA15-02B	08	core	0.95	0.17	0.26	0.00	0.00	17.82	6.60	12.49	7.35	0.02	51.34	97.04	14.82	0.028	0.008
CA15-02B	08	rim	1.06	0.17	0.27	0.01	0.08	17.57	6.89	12.51	7.24	0.04	51.37	97.26	14.86	0.029	0.009
CA15-02B	09	core	0.84	0.20	0.20	0.00	0.00	18.57	6.70	12.73	4.81	0.02	53.41	97.51	18.93	0.021	0.008

Sample	Grain	Position	Na_2O	MnO	TiO_2	Cl	F	MgO	FeO	CaO	Al_2O_3	K_2O	SiO_2	Total	Ti Unc (%)	Ti (apfu)	Ti Unc (apfu, 2σ)
CA15-02B	09	rim	0.79	0.17	0.18	0.00	0.08	17.80	6.90	12.33	6.80	0.04	51.76	96.87	21.4	0.019	0.008
CA15-02B	10	core	1.00	0.23	0.21	0.01	0.00	17.96	6.79	12.30	6.74	0.01	51.68	96.96	18.58	0.022	0.008
CA15-02B	10	rim	0.99	0.20	0.32	0.01	0.00	17.47	6.93	12.51	7.18	0.04	51.24	96.94	11.73	0.034	0.008
CA15-02B	11	core	1.02	0.14	0.26	0.00	0.00	17.76	6.88	12.49	7.11	0.04	50.91	96.65	14.68	0.027	0.008
CA15-02B	11	rim	0.83	0.18	0.18	0.00	0.00	17.71	6.76	12.45	7.33	0.03	51.34	96.83	23.28	0.019	0.009
CA15-02B	12	core	0.92	0.15	0.22	0.00	0.01	18.28	6.32	12.44	7.01	0.03	52.00	97.42	17.53	0.023	0.008
CA15-02B	12	rim	1.07	0.15	0.26	0.00	0.00	17.11	6.65	12.28	7.61	0.04	51.32	96.53	15.3	0.027	0.008
CA15-02B	13	core	1.07	0.14	0.23	0.00	0.11	17.63	6.66	12.60	7.28	0.02	50.66	96.46	17.22	0.025	0.009
CA15-02B	13	rim	1.03	0.22	0.20	0.00	0.00	17.55	6.92	12.33	6.80	0.03	51.65	96.76	18.89	0.021	0.008
CA15-02B	14	core	0.89	0.19	0.26	0.00	0.08	17.89	6.44	12.66	7.18	0.02	50.92	96.58	15.25	0.028	0.008
CA15-02B	14	rim	1.22	0.17	0.31	0.01	0.00	16.91	6.91	12.49	7.58	0.05	50.97	96.67	12.78	0.033	0.009
CA15-02B	15	core	0.91	0.15	0.26	0.01	0.07	17.98	6.54	12.39	7.24	0.02	51.11	96.71	14.64	0.027	0.008
CA15-02B	15	rim	0.88	0.17	0.19	0.00	0.00	17.96	7.06	11.69	6.00	0.04	52.35	96.37	20.11	0.020	0.008
CA15-02B	16	core	1.22	0.15	0.23	0.02	0.00	17.63	6.64	12.33	6.98	0.03	51.32	96.59	16.32	0.025	0.008
CA15-02B	16	rim	1.21	0.20	0.27	0.03	0.00	17.55	6.86	12.10	6.90	0.05	51.26	96.48	14.95	0.028	0.008
CA15-02B	17	core	0.90	0.12	0.28	0.00	0.01	17.59	6.73	12.63	7.22	0.03	51.59	97.16	13.27	0.030	0.008
CA15-02B	17	rim	0.21	0.18	0.00	0.00	0.00	18.87	7.12	13.15	1.05	0.00	55.66	96.24	100	0.000	0.000
CA15-03B	01	core	1.02	0.17	0.28	0.02	0.09	17.75	6.56	12.66	7.47	0.04	51.43	97.54	14.36	0.029	0.008

Sample	Grain	Position	Na_2O	MnO	TiO_2	Cl	F	MgO	FeO	CaO	Al_2O_3	K_2O	SiO_2	Total	Ti Unc (%)	Ti (apfu)	Ti Unc (apfu, 2σ)
CA15-03B	01	rim	0.91	0.15	0.20	0.00	0.10	18.11	6.43	12.43	6.76	0.03	52.32	97.47	18.92	0.021	0.008
CA15-03B	02	core	1.00	0.12	0.17	0.01	0.00	17.82	6.18	12.65	6.43	0.03	53.06	97.49	23.13	0.018	0.008
CA15-03B	02	rim	1.12	0.12	0.29	0.00	0.26	18.20	6.52	12.28	6.93	0.04	52.74	98.56	12.86	0.030	0.008
CA15-03B	03	core	0.92	0.17	0.23	0.00	0.10	18.25	6.59	12.24	7.19	0.02	52.05	97.82	16.33	0.024	0.008
CA15-03B	03	rim	0.91	0.15	0.27	0.00	0.06	18.34	6.43	12.71	7.04	0.02	51.83	97.80	13.66	0.028	0.008
CA15-03B	04	core	1.02	0.12	0.16	0.00	0.00	17.77	6.53	12.55	6.45	0.04	52.55	97.22	24.85	0.017	0.008
CA15-03B	04	rim	0.97	0.13	0.19	0.01	0.00	18.41	6.39	12.51	6.73	0.03	52.61	98.02	19.81	0.020	0.008
CA15-03B	05	core	0.74	0.15	0.23	0.02	0.00	18.28	6.33	12.92	6.40	0.03	52.37	97.50	16.1	0.024	0.008
CA15-03B	05	rim	0.85	0.16	0.19	0.00	0.19	18.44	6.17	12.34	6.67	0.00	52.44	97.49	19.81	0.020	0.008
CA15-03B	06	core	0.90	0.15	0.15	0.03	0.00	18.34	6.42	12.80	6.59	0.03	52.79	98.21	26.08	0.015	0.008
CA15-03B	06	rim	0.84	0.17	0.25	0.00	0.00	18.32	6.45	12.95	6.63	0.03	52.30	97.97	15.09	0.026	0.008
CA15-03B	07	core	0.94	0.15	0.22	0.00	0.07	18.18	6.55	12.69	7.06	0.03	51.92	97.85	17.74	0.023	0.008
CA15-03B	07	rim	0.97	0.12	0.24	0.01	0.23	18.45	6.25	12.77	6.81	0.02	51.97	97.88	16.45	0.025	0.008
CA15-03B	08	core	0.84	0.12	0.21	0.00	0.00	17.98	6.56	12.62	6.61	0.03	52.52	97.53	17.78	0.022	0.008
CA15-03B	08	rim	1.07	0.11	0.21	0.00	0.21	18.28	6.59	12.74	7.12	0.03	52.20	98.58	18.82	0.022	0.008
CA15-03B	09	core	0.93	0.12	0.25	0.00	0.00	18.35	6.23	11.62	6.29	0.03	52.58	96.44	14.69	0.027	0.008
CA15-03B	09	rim	0.97	0.13	0.23	0.00	0.01	18.33	6.46	12.18	7.20	0.04	52.08	97.66	17.93	0.024	0.009
CA15-03B	10	core	0.91	0.11	0.25	0.00	0.00	17.92	6.39	12.92	7.07	0.03	51.02	96.66	15.31	0.026	0.008

Sample	Grain	Position	Na_2O	MnO	TiO_2	Cl	F	MgO	FeO	CaO	Al_2O_3	K_2O	SiO_2	Total	Ti Unc (%)	Ti (apfu)	Ti Unc (apfu, 2σ)
CA15-03B	10	rim	1.00	0.17	0.20	0.01	0.00	17.92	6.63	11.68	7.27	0.03	51.93	96.88	19.27	0.021	0.008
CA15-03B	11	core	0.81	0.16	0.16	0.00	0.15	17.95	6.23	12.64	6.84	0.04	52.64	97.65	24.22	0.017	0.008
CA15-03B	11	rim	0.80	0.14	0.28	0.00	0.00	17.95	6.38	12.75	7.24	0.03	52.07	97.70	13.32	0.030	0.008
CA15-03B	12	core	0.86	0.11	0.27	0.00	0.00	17.86	6.61	12.75	6.17	0.02	52.35	97.06	12.88	0.029	0.007
CA15-03B	12	rim	0.87	0.12	0.23	0.01	0.00	18.30	6.36	12.91	7.21	0.03	52.29	98.37	17.23	0.024	0.008
CA15-03B	13	core	0.83	0.09	0.17	0.00	0.00	18.35	6.42	12.50	6.59	0.01	52.24	97.24	22.67	0.018	0.008
CA15-03B	13	rim	0.86	0.13	0.18	0.00	0.01	18.06	6.36	12.79	7.19	0.05	50.99	96.64	22.93	0.019	0.009
CA15-03B	14	core	0.97	0.12	0.22	0.00	0.00	18.13	6.51	12.42	7.24	0.03	52.31	98.00	16.71	0.023	0.008
CA15-03B	14	rim	0.83	0.14	0.17	0.00	0.05	18.50	6.20	12.58	6.45	0.01	52.69	97.64	22.8	0.017	0.008
CA15-03B	15	core	0.77	0.13	0.19	0.01	0.00	18.56	6.26	12.90	5.79	0.03	53.22	97.89	19.58	0.020	0.008
CA15-03B	15	rim	0.99	0.15	0.15	0.01	0.00	18.22	6.84	11.59	6.79	0.02	52.20	96.99	25.6	0.016	0.008
CA15-03B	16	core	0.92	0.18	0.20	0.00	0.10	18.35	6.44	12.29	7.11	0.03	52.72	98.38	17.96	0.021	0.008
CA15-03B	16	rim	0.96	0.13	0.12	0.00	0.09	18.25	6.44	12.45	7.33	0.03	52.62	98.43	33.7	0.012	0.008
CA15-03B	17	core	0.87	0.13	0.18	0.00	0.02	17.71	6.47	12.54	7.23	0.03	52.32	97.54	21.3	0.019	0.008
CA15-03B	17	rim	0.93	0.15	0.25	0.00	0.00	18.05	6.47	12.62	6.97	0.01	52.49	97.99	14.15	0.026	0.007
CA22-3	01	core	1.49	0.06	0.89	0.01	0.00	12.46	11.44	11.55	14.39	0.53	45.55	98.52	5.45	0.095	0.010
CA22-3	01	rim	1.67	0.14	0.97	0.01	0.00	11.39	11.54	11.78	16.52	0.60	44.59	99.38	4.45	0.104	0.009
CA22-3	02	core	1.14	0.04	0.70	0.07	0.00	10.04	10.11	8.56	16.39	2.07	46.43	95.68	6.15	0.077	0.009
CA22-3	02	rim	1.64	0.07	0.84	0.02	0.00	11.56	11.75	11.52	15.02	0.58	44.71	97.86	5.55	0.091	0.010

Sample	Grain	Position	Na_2O	MnO	TiO_2	Cl	F	MgO	FeO	CaO	Al_2O_3	K_2O	SiO_2	Total	Ti Unc (%)	Ti (apfu)	Ti Unc (apfu, 2σ)
CA22-3	03	core	1.69	0.08	1.05	0.02	0.00	12.05	12.20	11.63	14.86	0.55	45.30	99.61	4.57	0.113	0.010
CA22-3	03	rim	1.74	0.10	0.53	0.02	0.00	10.85	12.17	11.46	17.64	0.55	43.49	98.64	7.76	0.057	0.009
CA22-3	04	core	1.65	0.08	0.99	0.01	0.03	11.41	11.96	11.63	16.71	0.71	43.48	98.84	4.45	0.107	0.010
CA22-3	04	rim	1.61	0.07	0.88	0.03	0.16	11.23	11.94	11.57	16.97	0.72	43.71	99.03	5	0.095	0.009
CA22-3	05	core	1.61	0.10	1.00	0.01	0.08	12.56	11.72	11.44	14.36	0.52	44.83	98.40	4.66	0.108	0.010
CA22-3	05	rim	1.72	0.11	0.60	0.01	0.10	12.68	11.13	10.69	14.52	0.46	46.25	98.38	7.42	0.065	0.010
CA22-3	06	core	1.68	0.01	0.63	0.02	0.00	10.96	12.23	11.44	17.90	0.64	43.17	98.80	7.11	0.068	0.010
CA22-3	06	rim	1.72	0.08	0.70	0.03	0.09	10.66	12.36	11.34	17.81	0.62	43.19	98.73	5.99	0.076	0.009
CA22-3	07	core	1.66	0.09	0.95	0.02	0.02	11.43	11.87	11.59	15.84	0.57	44.33	98.53	4.85	0.103	0.010
CA22-3	07	rim	1.50	0.09	0.93	0.01	0.17	11.06	11.83	11.56	16.53	0.65	43.72	98.22	5.05	0.102	0.010
CA22-3	08	core	1.45	0.06	0.92	0.01	0.00	12.19	11.60	11.59	15.06	0.54	45.03	98.61	5.12	0.099	0.010
CA22-3	08	rim	1.28	0.06	0.83	0.02	0.16	10.03	10.61	13.75	18.32	0.54	43.12	98.88	5.31	0.092	0.010
CA22-3	09	core	1.33	0.09	0.82	0.00	0.00	12.92	11.95	11.71	12.58	0.36	46.82	98.73	5.7	0.089	0.010
CA22-3	09	rim	1.67	0.10	0.85	0.01	0.17	11.01	11.95	11.19	16.91	0.61	44.22	98.84	5.2	0.092	0.010
CA22-3	10	core	1.60	0.07	0.92	0.02	0.00	11.69	12.05	11.74	16.52	0.62	44.15	99.53	5.01	0.099	0.010
CA22-3	10	rim	1.93	0.05	0.57	0.01	0.00	10.56	12.38	11.61	17.50	0.62	43.79	99.12	7.49	0.062	0.009
CA22-3	11	core	1.64	0.12	0.83	0.01	0.00	11.45	12.02	11.72	16.35	0.64	44.37	99.29	5.5	0.089	0.010
CA22-3	11	rim	1.66	0.09	0.85	0.02	0.09	11.17	12.34	11.46	15.48	0.69	43.94	97.93	5.24	0.093	0.010
CA22-3	12	core	1.69	0.08	0.83	0.02	0.00	11.14	12.12	11.37	16.60	0.62	44.12	98.75	5.38	0.090	0.010
CA22-3	12	rim	1.69	0.09	0.72	0.03	0.00	11.05	12.65	11.41	17.08	0.73	43.07	98.65	6.18	0.078	0.010
CA22-3	13	core	1.58	0.14	1.23	0.00	0.00	12.18	11.80	11.68	14.28	0.57	45.27	98.94	3.87	0.132	0.010
CA22-3	13	rim	1.89	0.09	0.66	0.01	0.11	10.69	12.02	11.31	17.48	0.59	43.76	98.73	6.43	0.071	0.009
CA22-3	14	core	1.59	0.07	0.88	0.02	0.19	11.69	12.06	11.75	15.40	0.61	44.10	98.53	5.24	0.096	0.010
CA22-3	14	rim	1.52	0.11	0.63	0.02	0.06	11.07	11.99	11.76	17.80	0.72	43.47	99.25	6.93	0.068	0.009
CA22-3	15	core	1.54	0.10	0.87	0.02	0.00	12.04	11.86	11.49	15.12	0.54	44.89	98.62	5.15	0.093	0.010
CA22-3	15	rim	1.57	0.09	0.64	0.03	0.17	11.16	12.36	11.54	16.78	0.54	44.52	99.50	6.35	0.068	0.009
CA22-3	16	core	1.70	0.12	0.71	0.02	0.07	11.24	12.26	11.15	16.90	0.65	44.20	99.15	6.32	0.076	0.010
CA22-3	16	rim	1.67	0.10	0.51	0.01	0.18	10.62	12.36	11.35	18.18	0.62	43.26	98.95	8.23	0.055	0.009

Sample	Grain	Position	Na_2O	MnO	TiO_2	Cl	F	MgO	FeO	CaO	Al_2O_3	K_2O	SiO_2	Total	Ti Unc (%)	Ti (apfu)	Ti Unc (apfu, 2σ)
CA22-3	17	core	1.56	0.11	0.79	0.03	0.06	11.48	12.17	11.45	16.42	0.71	43.94	98.85	5.72	0.085	0.010
CA22-3	17	rim	1.51	0.10	0.83	0.01	0.00	11.31	12.37	11.59	16.82	0.67	44.23	99.59	5.42	0.090	0.010
CA22-1	01	core	1.67	0.25	0.50	0.01	0.06	13.49	11.91	11.28	11.08	0.00	47.02	97.35	8.33	0.054	0.009
CA22-1	01	rim	1.69	0.24	0.57	0.00	0.00	12.87	11.85	10.83	12.71	0.04	46.50	97.39	7.48	0.062	0.009
CA22-1	03	core	1.54	0.20	0.57	0.01	0.05	13.43	12.06	11.84	12.20	0.04	46.13	98.17	7.65	0.062	0.009
CA22-1	03	rim	1.63	0.20	0.56	0.01	0.00	13.58	11.94	11.03	12.27	0.05	46.22	97.58	7.84	0.060	0.009
CA22-1	04	core	1.50	0.19	0.58	0.02	0.02	13.77	11.87	11.73	12.16	0.04	46.78	98.75	7.22	0.062	0.009
CA22-1	04	rim	1.72	0.20	0.64	0.01	0.00	13.03	11.85	11.56	12.57	0.03	45.95	97.67	6.7	0.069	0.009
CA22-1	05	core	1.83	0.24	0.54	0.00	0.00	13.31	12.29	11.61	11.84	0.04	46.59	98.38	7.75	0.058	0.009
CA22-1	05	rim	1.98	0.16	0.62	0.00	0.00	12.48	12.48	10.84	13.42	0.06	45.64	97.79	6.99	0.067	0.009
CA22-1	06	core	1.56	0.26	0.43	0.01	0.09	12.84	12.08	11.40	11.38	0.03	46.14	96.29	9.87	0.047	0.009
CA22-1	06	rim	1.80	0.24	0.59	0.00	0.00	12.44	12.69	11.26	13.32	0.07	45.97	98.48	7.21	0.064	0.009
CA22-1	07	core	1.74	0.20	0.54	0.01	0.06	13.49	12.17	11.71	11.53	0.03	47.03	98.61	7.75	0.058	0.009
CA22-1	07	rim	2.01	0.26	0.50	0.02	0.00	11.94	12.58	11.43	14.74	0.05	44.57	98.17	8.65	0.054	0.009
CA22-1	08	core	1.84	0.28	0.61	0.00	0.09	12.97	12.75	10.62	12.72	0.05	46.32	98.36	6.91	0.066	0.009
CA22-1	08	rim	1.89	0.26	0.56	0.00	0.00	12.97	12.38	11.37	12.95	0.03	46.24	98.74	7.97	0.060	0.010
CA22-1	09	core	1.84	0.19	0.69	0.00	0.09	12.56	13.20	10.98	12.81	0.05	45.83	98.35	5.87	0.074	0.009
CA22-1	09	rim	1.92	0.24	0.65	0.00	0.16	12.99	12.45	11.42	13.24	0.06	45.75	98.98	6.56	0.070	0.009
CA22-1	10	core	1.82	0.21	0.63	0.01	0.00	11.86	13.23	11.65	13.16	0.05	45.53	98.25	6.71	0.069	0.009
CA22-1	10	rim	1.63	0.20	0.68	0.00	0.11	12.61	13.33	10.70	13.62	0.06	45.26	98.32	6.29	0.074	0.009
CA22-1	11	core	1.85	0.21	0.60	0.01	0.10	12.18	13.43	11.27	13.42	0.05	45.49	98.72	7.11	0.065	0.009
CA22-1	11	rim	1.76	0.21	0.55	0.00	0.00	13.00	12.72	11.17	12.85	0.04	45.93	98.33	7.7	0.060	0.009
CA22-1	12	core	1.94	0.28	0.59	0.01	0.00	12.21	12.99	11.33	13.68	0.04	45.38	98.55	7.58	0.063	0.010
CA22-1	12	rim	1.72	0.24	0.69	0.01	0.00	12.35	13.13	10.82	13.22	0.04	44.53	96.87	5.9	0.076	0.009
CA22-1	13	core	1.68	0.19	0.42	0.01	0.16	13.36	12.31	11.60	11.88	0.04	47.17	98.89	9.98	0.045	0.009
CA22-1	13	rim	1.75	0.18	0.59	0.01	0.00	12.95	12.11	11.59	13.45	0.07	46.13	98.93	7.5	0.063	0.009
CA22-1	14	core	1.69	0.21	0.60	0.00	0.00	12.99	12.50	11.21	13.10	0.07	45.47	97.95	6.93	0.065	0.009
CA22-1	14	rim	1.77	0.23	0.60	0.00	0.13	13.18	12.26	11.47	12.73	0.05	46.29	98.82	6.91	0.065	0.009

Sample	Grain	Position	Na_2O	MnO	TiO_2	Cl	F	MgO	FeO	CaO	Al_2O_3	K_2O	SiO_2	Total	Ti Unc (%)	Ti (apfu)	Ti Unc (apfu, 2σ)
CA22-1	15	core	1.42	0.20	0.49	0.00	0.09	13.67	11.92	11.75	11.49	0.01	47.44	98.56	8.58	0.053	0.009
CA22-1	15	rim	1.68	0.19	1.12	0.02	0.11	12.91	11.70	11.91	12.25	0.04	45.68	97.81	4.28	0.122	0.010

Table C.2. Amphibole formulae (in apfu) calculated using AMFORM (Ridolfi et al., 2018), normalized to 22 O.

			Tetrahedral Site		*C Site*						*B Site*		*A Site*			*W Site*			
Sample	**Grain**	**Position**	**Si**	**Al**	**Al**	**Ti**	**Fe^{3+}**	**Mg**	**Fe^{2+}**	**Mn**	**Ca**	**Na**	**Ca**	**Na**	**K**	**OH**	**F**	**Cl**	**O**
CA15-02B	01	core	7.173	0.827	0.443	0.024	0.238	3.713	0.567	0.016	1.917	0.083	0.000	0.177	0.004	2.000	0.000	0.000	0.000
CA15-02B	01	rim	7.237	0.763	0.800	0.019	0.000	3.296	0.869	0.016	1.995	0.005	0.000	0.157	0.008	1.751	0.011	0.001	0.237
CA15-02B	02	core	7.311	0.689	0.411	0.027	0.161	3.754	0.627	0.020	1.882	0.118	0.000	0.180	0.002	2.000	0.000	0.000	0.000
CA15-02B	02	rim	7.415	0.585	0.475	0.013	0.069	3.677	0.743	0.022	1.875	0.125	0.000	0.134	0.006	2.000	0.000	0.000	0.000
CA15-02B	03	core	7.264	0.736	0.442	0.020	0.177	3.751	0.592	0.018	1.917	0.083	0.000	0.159	0.000	2.000	0.000	0.000	0.000
CA15-02B	03	rim	7.711	0.289	0.188	0.012	0.134	4.097	0.553	0.017	1.890	0.110	0.000	0.045	0.009	1.990	0.010	0.000	0.000
CA15-02B	04	core	7.255	0.745	0.495	0.029	0.106	3.651	0.697	0.021	1.900	0.100	0.000	0.181	0.004	1.945	0.051	0.004	0.000
CA15-02B	04	rim	7.911	0.089	0.093	0.006	0.006	4.137	0.735	0.024	1.963	0.037	0.000	0.013	0.003	2.000	0.000	0.000	0.000
CA15-02B	05	core	7.622	0.378	0.159	0.005	0.199	3.963	0.652	0.022	1.922	0.078	0.000	0.085	0.002	1.998	0.000	0.002	0.000
CA15-02B	05	rim	7.089	0.911	0.615	0.031	0.202	3.523	0.615	0.015	1.864	0.136	0.000	0.160	0.009	1.955	0.042	0.004	0.000
CA15-02B	07	core	7.250	0.750	0.444	0.020	0.146	3.698	0.673	0.018	1.909	0.091	0.000	0.207	0.002	1.953	0.047	0.000	0.000
CA15-02B	07	rim	7.294	0.706	0.492	0.025	0.081	3.644	0.733	0.024	1.900	0.100	0.000	0.182	0.000	2.000	0.000	0.000	0.000
CA15-02B	08	core	7.221	0.779	0.440	0.028	0.258	3.736	0.518	0.020	1.882	0.118	0.000	0.141	0.003	2.000	0.000	0.000	0.000
CA15-02B	08	rim	7.243	0.757	0.446	0.029	0.177	3.693	0.636	0.020	1.890	0.110	0.000	0.181	0.007	1.962	0.036	0.002	0.000
CA15-02B	09	core	7.491	0.509	0.287	0.021	0.123	3.883	0.663	0.024	1.913	0.087	0.000	0.140	0.003	2.000	0.000	0.000	0.000

			Tetrahedral Site		*C Site*						*B Site*		*A Site*			*W Site*			
Sample	**Grain**	**Position**	**Si**	**Al**	**Al**	**Ti**	**Fe^{3+}**	**Mg**	**Fe^{2+}**	**Mn**	**Ca**	**Na**	**Ca**	**Na**	**K**	**OH**	**F**	**Cl**	**O**
CA15-02B	09	rim	7.293	0.707	0.422	0.019	0.279	3.739	0.534	0.020	1.861	0.126	0.000	0.089	0.006	1.964	0.036	0.000	0.000
CA15-02B	10	core	7.275	0.725	0.393	0.022	0.280	3.769	0.519	0.027	1.855	0.133	0.000	0.139	0.002	1.998	0.000	0.002	0.000
CA15-02B	10	rim	7.244	0.756	0.441	0.034	0.179	3.682	0.640	0.024	1.895	0.105	0.000	0.166	0.006	1.998	0.000	0.002	0.000
CA15-02B	11	core	7.207	0.793	0.393	0.027	0.269	3.748	0.545	0.016	1.894	0.106	0.000	0.173	0.007	2.000	0.000	0.000	0.000
CA15-02B	11	rim	7.234	0.766	0.451	0.019	0.274	3.720	0.523	0.021	1.879	0.114	0.000	0.113	0.005	2.000	0.000	0.000	0.000
CA15-02B	12	core	7.270	0.730	0.425	0.023	0.247	3.810	0.492	0.018	1.863	0.121	0.000	0.128	0.005	1.995	0.005	0.000	0.000
CA15-02B	12	rim	7.277	0.723	0.549	0.027	0.086	3.617	0.703	0.018	1.866	0.134	0.000	0.161	0.006	2.000	0.000	0.000	0.000
CA15-02B	13	core	7.206	0.794	0.427	0.025	0.177	3.739	0.616	0.017	1.920	0.080	0.000	0.216	0.004	1.949	0.051	0.000	0.000
CA15-02B	13	rim	7.303	0.697	0.436	0.021	0.196	3.699	0.622	0.026	1.868	0.132	0.000	0.150	0.005	2.000	0.000	0.000	0.000
CA15-02B	14	core	7.211	0.789	0.410	0.028	0.232	3.777	0.530	0.023	1.921	0.079	0.000	0.166	0.004	1.964	0.036	0.000	0.000
CA15-02B	14	rim	7.260	0.740	0.532	0.033	0.000	3.590	0.823	0.021	1.906	0.094	0.000	0.242	0.009	1.983	0.000	0.002	0.015
CA15-02B	15	core	7.213	0.787	0.417	0.027	0.285	3.783	0.487	0.018	1.873	0.110	0.000	0.138	0.004	1.966	0.031	0.003	0.000
CA15-02B	15	rim	7.393	0.607	0.391	0.020	0.298	3.781	0.536	0.020	1.769	0.185	0.000	0.056	0.007	2.000	0.000	0.000	0.000
CA15-02B	16	core	7.277	0.723	0.443	0.025	0.146	3.727	0.642	0.018	1.873	0.127	0.000	0.208	0.005	1.995	0.000	0.005	0.000
CA15-02B	16	rim	7.270	0.730	0.423	0.028	0.231	3.711	0.583	0.024	1.839	0.161	0.000	0.172	0.009	1.992	0.000	0.008	0.000
CA15-02B	17	core	7.269	0.731	0.468	0.030	0.138	3.695	0.655	0.015	1.907	0.093	0.000	0.153	0.005	1.995	0.005	0.000	0.000
CA15-02B	17	rim	7.940	0.060	0.116	0.000	0.000	4.013	0.849	0.021	2.000	0.000	0.010	0.058	0.000	1.866	0.000	0.000	0.134
CA15-03B	01	core	7.225	0.775	0.462	0.029	0.158	3.717	0.613	0.021	1.906	0.094	0.000	0.183	0.007	1.956	0.041	0.004	0.000
CA15-03B	01	rim	7.318	0.682	0.433	0.021	0.229	3.776	0.523	0.018	1.863	0.137	0.000	0.110	0.005	1.954	0.046	0.000	0.000
CA15-03B	02	core	7.449	0.551	0.513	0.018	0.000	3.729	0.726	0.014	1.903	0.097	0.000	0.175	0.004	1.918	0.000	0.002	0.080
CA15-03B	02	rim	7.309	0.691	0.441	0.030	0.231	3.760	0.525	0.015	1.823	0.175	0.000	0.127	0.006	1.885	0.115	0.000	0.000
CA15-03B	03	core	7.260	0.740	0.443	0.024	0.234	3.795	0.535	0.021	1.829	0.119	0.000	0.130	0.004	1.955	0.045	0.000	0.000

			Tetrahedral Site		*C Site*						*B Site*		*A Site*			*W Site*			
Sample	**Grain**	**Position**	**Si**	**Al**	**Al**	**Ti**	**Fe^{3+}**	**Mg**	**Fe^{2+}**	**Mn**	**Ca**	**Na**	**Ca**	**Na**	**K**	**OH**	**F**	**Cl**	**O**
CA15-03B	03	rim	7.236	0.764	0.394	0.028	0.248	3.817	0.503	0.018	1.901	0.092	0.000	0.155	0.003	1.975	0.025	0.000	0.000
CA15-03B	04	core	7.399	0.601	0.470	0.017	0.025	3.730	0.744	0.014	1.893	0.107	0.000	0.173	0.006	2.000	0.000	0.000	0.000
CA15-03B	04	rim	7.308	0.692	0.410	0.020	0.250	3.812	0.492	0.015	1.862	0.138	0.000	0.123	0.006	1.998	0.000	0.002	0.000
CA15-03B	05	core	7.340	0.660	0.397	0.024	0.128	3.819	0.614	0.017	1.940	0.060	0.000	0.141	0.006	1.996	0.000	0.004	0.000
CA15-03B	05	rim	7.325	0.675	0.423	0.020	0.243	3.840	0.478	0.018	1.847	0.131	0.000	0.099	0.000	1.914	0.086	0.000	0.000
CA15-03B	06	core	7.340	0.660	0.420	0.015	0.149	3.801	0.598	0.017	1.907	0.093	0.000	0.149	0.005	1.994	0.000	0.006	0.000
CA15-03B	06	rim	7.299	0.701	0.390	0.026	0.155	3.812	0.598	0.020	1.936	0.064	0.000	0.163	0.004	2.000	0.000	0.000	0.000
CA15-03B	07	core	7.249	0.751	0.410	0.023	0.239	3.784	0.525	0.018	1.898	0.102	0.000	0.152	0.006	1.970	0.030	0.000	0.000
CA15-03B	07	rim	7.264	0.736	0.386	0.025	0.209	3.844	0.521	0.014	1.912	0.088	0.000	0.175	0.004	1.897	0.101	0.002	0.000
CA15-03B	08	core	7.352	0.648	0.443	0.022	0.141	3.752	0.627	0.015	1.893	0.107	0.000	0.122	0.005	2.000	0.000	0.000	0.000
CA15-03B	08	rim	7.250	0.750	0.415	0.022	0.207	3.785	0.559	0.013	1.896	0.104	0.000	0.185	0.004	1.910	0.090	0.000	0.000
CA15-03B	09	core	7.391	0.609	0.433	0.027	0.265	3.845	0.468	0.014	1.750	0.199	0.000	0.053	0.005	2.000	0.000	0.000	0.000
CA15-03B	09	rim	7.263	0.737	0.446	0.024	0.237	3.811	0.517	0.015	1.820	0.131	0.000	0.131	0.007	1.995	0.005	0.000	0.000
CA15-03B	10	core	7.234	0.766	0.415	0.026	0.119	3.788	0.639	0.013	1.963	0.037	0.000	0.213	0.005	2.000	0.000	0.000	0.000
CA15-03B	10	rim	7.291	0.709	0.494	0.021	0.251	3.751	0.528	0.021	1.757	0.178	0.000	0.095	0.005	1.998	0.000	0.002	0.000
CA15-03B	11	core	7.364	0.636	0.492	0.017	0.095	3.743	0.634	0.019	1.895	0.105	0.000	0.114	0.007	1.934	0.066	0.000	0.000
CA15-03B	11	rim	7.276	0.724	0.469	0.030	0.155	3.739	0.590	0.017	1.909	0.091	0.000	0.127	0.005	2.000	0.000	0.000	0.000
CA15-03B	12	core	7.391	0.609	0.418	0.029	0.036	3.759	0.745	0.014	1.929	0.071	0.000	0.164	0.004	2.000	0.000	0.000	0.000
CA15-03B	12	rim	7.258	0.742	0.437	0.024	0.179	3.787	0.560	0.014	1.920	0.080	0.000	0.153	0.005	1.998	0.000	0.002	0.000
CA15-03B	13	core	7.311	0.689	0.398	0.018	0.265	3.828	0.486	0.011	1.874	0.119	0.000	0.107	0.002	2.000	0.000	0.000	0.000
CA15-03B	13	rim	7.209	0.791	0.407	0.019	0.227	3.807	0.525	0.015	1.938	0.062	0.000	0.172	0.009	1.995	0.005	0.000	0.000
CA15-03B	14	core	7.272	0.728	0.458	0.023	0.237	3.757	0.519	0.015	1.850	0.140	0.000	0.121	0.005	2.000	0.000	0.000	0.000

			Tetrahedral Site		*C Site*						*B Site*		*A Site*			*W Site*			
Sample	**Grain**	**Position**	**Si**	**Al**	**Al**	**Ti**	**Fe^{3+}**	**Mg**	**Fe^{2+}**	**Mn**	**Ca**	**Na**	**Ca**	**Na**	**K**	**OH**	**F**	**Cl**	**O**
CA15-03B	14	rim	7.342	0.658	0.401	0.017	0.240	3.843	0.483	0.016	1.878	0.122	0.000	0.103	0.002	1.980	0.020	0.000	0.000
CA15-03B	15	core	7.423	0.577	0.375	0.020	0.093	3.859	0.638	0.016	1.928	0.072	0.000	0.137	0.005	1.998	0.000	0.002	0.000
CA15-03B	15	rim	7.322	0.678	0.445	0.016	0.263	3.810	0.539	0.018	1.742	0.167	0.000	0.102	0.003	1.998	0.000	0.002	0.000
CA15-03B	16	core	7.301	0.699	0.462	0.021	0.219	3.788	0.527	0.021	1.824	0.138	0.000	0.108	0.006	1.955	0.045	0.000	0.000
CA15-03B	16	rim	7.281	0.719	0.476	0.012	0.239	3.765	0.506	0.015	1.846	0.141	0.000	0.117	0.004	1.960	0.040	0.000	0.000
CA15-03B	17	core	7.321	0.679	0.514	0.019	0.126	3.694	0.632	0.016	1.880	0.120	0.000	0.117	0.005	1.990	0.010	0.000	0.000
CA15-03B	17	rim	7.311	0.689	0.455	0.026	0.161	3.748	0.592	0.018	1.883	0.117	0.000	0.136	0.002	2.000	0.000	0.000	0.000
CA22-3	01	core	6.522	1.478	0.951	0.095	0.295	2.660	1.075	0.008	1.772	0.145	0.000	0.269	0.096	1.819	0.000	0.002	0.178
CA22-3	01	rim	6.353	1.647	1.127	0.104	0.266	2.419	1.109	0.016	1.798	0.160	0.000	0.301	0.110	1.794	0.000	0.001	0.205
CA22-3	02	core	6.749	1.251	1.556	0.077	0.334	2.175	0.895	0.005	1.333	0.322	0.000	0.000	0.384	1.734	0.000	0.016	0.249
CA22-3	02	rim	6.460	1.540	1.018	0.091	0.322	2.490	1.098	0.008	1.783	0.190	0.000	0.269	0.107	1.826	0.000	0.006	0.168
CA22-3	03	core	6.452	1.548	0.947	0.113	0.302	2.559	1.152	0.009	1.775	0.144	0.000	0.323	0.099	1.791	0.000	0.004	0.204
CA22-3	03	rim	6.244	1.756	1.229	0.057	0.331	2.322	1.130	0.013	1.763	0.156	0.000	0.329	0.101	1.805	0.000	0.004	0.191
CA22-3	04	core	6.258	1.742	1.092	0.107	0.335	2.448	1.105	0.010	1.793	0.110	0.000	0.350	0.131	1.713	0.015	0.003	0.269
CA22-3	04	rim	6.276	1.724	1.147	0.095	0.344	2.404	1.090	0.008	1.780	0.133	0.000	0.315	0.131	1.653	0.071	0.007	0.269
CA22-3	05	core	6.457	1.543	0.894	0.108	0.323	2.697	1.089	0.012	1.765	0.112	0.000	0.338	0.096	1.750	0.036	0.002	0.212
CA22-3	05	rim	6.595	1.405	1.035	0.065	0.273	2.695	1.054	0.013	1.633	0.232	0.000	0.244	0.084	1.824	0.045	0.003	0.128
CA22-3	06	core	6.199	1.801	1.228	0.068	0.366	2.346	1.103	0.001	1.760	0.128	0.000	0.339	0.118	1.737	0.000	0.005	0.258
CA22-3	06	rim	6.217	1.783	1.238	0.076	0.352	2.287	1.135	0.010	1.749	0.152	0.000	0.328	0.114	1.703	0.041	0.007	0.250
CA22-3	07	core	6.378	1.622	1.063	0.103	0.312	2.451	1.116	0.011	1.787	0.157	0.000	0.306	0.104	1.775	0.010	0.004	0.211
CA22-3	07	rim	6.323	1.677	1.141	0.102	0.329	2.385	1.101	0.011	1.791	0.139	0.000	0.281	0.121	1.662	0.076	0.002	0.259
CA22-3	08	core	6.454	1.546	0.998	0.099	0.302	2.604	1.088	0.008	1.780	0.121	0.000	0.282	0.098	1.787	0.000	0.002	0.211
CA22-3	08	rim	6.283	1.717	1.429	0.092	0.000	2.179	1.293	0.008	2.000	0.000	0.147	0.362	0.101	1.270	0.073	0.005	0.652
CA22-3	09	core	6.685	1.315	0.802	0.089	0.273	2.750	1.154	0.011	1.791	0.130	0.000	0.238	0.066	1.888	0.000	0.000	0.112
CA22-3	09	rim	6.343	1.657	1.202	0.092	0.309	2.355	1.125	0.012	1.720	0.186	0.000	0.279	0.112	1.679	0.076	0.003	0.242
CA22-3	10	core	6.298	1.702	1.075	0.099	0.326	2.486	1.111	0.008	1.794	0.101	0.000	0.342	0.112	1.746	0.000	0.005	0.250

			Tetrahedral Site		*C Site*						*B Site*		*A Site*			*W Site*			
Sample	**Grain**	**Position**	**Si**	**Al**	**Al**	**Ti**	**Fe^{3+}**	**Mg**	**Fe^{2+}**	**Mn**	**Ca**	**Na**	**Ca**	**Na**	**K**	**OH**	**F**	**Cl**	**O**
CA22-3	10	rim	6.265	1.735	1.215	0.062	0.332	2.252	1.150	0.006	1.780	0.204	0.000	0.331	0.113	1.822	0.000	0.003	0.175
CA22-3	11	core	6.338	1.662	1.091	0.089	0.302	2.438	1.134	0.014	1.794	0.139	0.000	0.316	0.117	1.796	0.000	0.002	0.202
CA22-3	11	rim	6.380	1.620	1.029	0.093	0.350	2.418	1.149	0.012	1.783	0.167	0.000	0.300	0.127	1.751	0.041	0.004	0.204
CA22-3	12	core	6.334	1.666	1.142	0.090	0.317	2.384	1.138	0.010	1.749	0.169	0.000	0.301	0.114	1.776	0.000	0.005	0.220
CA22-3	12	rim	6.218	1.782	1.124	0.078	0.369	2.378	1.158	0.011	1.765	0.116	0.000	0.357	0.135	1.750	0.000	0.006	0.244
CA22-3	13	core	6.491	1.509	0.904	0.132	0.270	2.604	1.145	0.017	1.794	0.134	0.000	0.306	0.104	1.794	0.000	0.000	0.206
CA22-3	13	rim	6.282	1.718	1.239	0.071	0.321	2.288	1.122	0.011	1.739	0.209	0.000	0.317	0.108	1.747	0.050	0.003	0.200
CA22-3	14	core	6.367	1.633	0.988	0.096	0.357	2.516	1.099	0.009	1.818	0.117	0.000	0.328	0.113	1.681	0.086	0.005	0.227
CA22-3	14	rim	6.216	1.784	1.216	0.068	0.331	2.360	1.103	0.013	1.802	0.107	0.000	0.314	0.132	1.733	0.025	0.004	0.238
CA22-3	15	core	6.440	1.560	0.997	0.093	0.308	2.575	1.115	0.012	1.766	0.133	0.000	0.296	0.099	1.802	0.000	0.004	0.194
CA22-3	15	rim	6.346	1.654	1.165	0.068	0.329	2.371	1.144	0.010	1.762	0.149	0.000	0.285	0.098	1.708	0.075	0.007	0.211
CA22-3	16	core	6.322	1.678	1.170	0.076	0.318	2.397	1.148	0.015	1.709	0.167	0.000	0.304	0.119	1.745	0.030	0.005	0.220
CA22-3	16	rim	6.209	1.791	1.284	0.055	0.348	2.272	1.136	0.012	1.745	0.147	0.000	0.318	0.113	1.680	0.080	0.003	0.236
CA22-3	17	core	6.313	1.687	1.094	0.085	0.340	2.459	1.122	0.013	1.763	0.124	0.000	0.311	0.129	1.731	0.025	0.008	0.235
CA22-3	17	rim	6.307	1.693	1.134	0.090	0.315	2.404	1.160	0.012	1.771	0.115	0.000	0.302	0.123	1.754	0.000	0.002	0.244
CA22-1	01	core	6.785	1.215	0.669	0.054	0.296	2.902	1.141	0.031	1.744	0.163	0.000	0.304	0.000	1.973	0.026	0.001	0.000
CA22-1	01	rim	6.698	1.302	0.855	0.062	0.257	2.763	1.170	0.029	1.671	0.192	0.000	0.280	0.007	1.971	0.000	0.000	0.029
CA22-1	03	core	6.628	1.372	0.694	0.062	0.302	2.877	1.147	0.024	1.823	0.072	0.000	0.357	0.008	1.936	0.020	0.002	0.041
CA22-1	03	rim	6.659	1.341	0.743	0.060	0.296	2.917	1.143	0.024	1.703	0.114	0.000	0.341	0.009	1.945	0.000	0.001	0.054
CA22-1	04	core	6.666	1.334	0.708	0.062	0.280	2.925	1.135	0.023	1.791	0.077	0.000	0.338	0.006	1.941	0.010	0.004	0.045
CA22-1	04	rim	6.624	1.376	0.760	0.069	0.289	2.800	1.140	0.024	1.786	0.131	0.000	0.349	0.005	1.963	0.000	0.002	0.035
CA22-1	05	core	6.677	1.323	0.677	0.058	0.286	2.844	1.187	0.029	1.783	0.136	0.000	0.372	0.008	2.000	0.000	0.000	0.000
CA22-1	05	rim	6.581	1.419	0.862	0.067	0.302	2.683	1.203	0.020	1.675	0.188	0.000	0.365	0.011	1.933	0.000	0.000	0.067
CA22-1	06	core	6.739	1.261	0.698	0.047	0.360	2.796	1.115	0.032	1.784	0.169	0.000	0.273	0.005	1.955	0.041	0.003	0.000
CA22-1	06	rim	6.592	1.408	0.843	0.064	0.273	2.659	1.248	0.029	1.730	0.153	0.000	0.348	0.012	1.957	0.000	0.000	0.043
CA22-1	07	core	6.720	1.280	0.661	0.058	0.288	2.873	1.166	0.024	1.793	0.137	0.000	0.345	0.006	1.972	0.025	0.003	0.000
CA22-1	07	rim	6.423	1.577	0.926	0.054	0.308	2.565	1.208	0.032	1.765	0.142	0.000	0.419	0.008	1.946	0.000	0.004	0.050
CA22-1	08	core	6.649	1.351	0.801	0.066	0.276	2.775	1.255	0.034	1.633	0.160	0.000	0.352	0.009	1.902	0.040	0.000	0.058

			Tetrahedral Site		*C Site*						*B Site*		*A Site*			*W Site*			
Sample	**Grain**	**Position**	**Si**	**Al**	**Al**	**Ti**	**Fe^{3+}**	**Mg**	**Fe^{2+}**	**Mn**	**Ca**	**Na**	**Ca**	**Na**	**K**	**OH**	**F**	**Cl**	**O**
CA22-1	08	rim	6.605	1.395	0.785	0.060	0.265	2.762	1.214	0.031	1.740	0.143	0.000	0.380	0.006	1.982	0.000	0.000	0.018
CA22-1	09	core	6.603	1.397	0.778	0.074	0.317	2.698	1.274	0.023	1.695	0.141	0.000	0.373	0.009	1.873	0.040	0.000	0.087
CA22-1	09	rim	6.545	1.455	0.777	0.070	0.294	2.770	1.196	0.029	1.750	0.114	0.000	0.419	0.010	1.858	0.070	0.000	0.071
CA22-1	10	core	6.569	1.431	0.807	0.069	0.308	2.551	1.288	0.025	1.801	0.151	0.000	0.358	0.008	1.961	0.000	0.002	0.037
CA22-1	10	rim	6.529	1.471	0.845	0.074	0.333	2.712	1.275	0.024	1.654	0.083	0.000	0.373	0.011	1.793	0.050	0.000	0.156
CA22-1	11	core	6.542	1.458	0.817	0.065	0.320	2.611	1.295	0.026	1.737	0.129	0.000	0.387	0.010	1.876	0.045	0.002	0.077
CA22-1	11	rim	6.596	1.404	0.771	0.060	0.300	2.783	1.227	0.026	1.719	0.114	0.000	0.376	0.006	1.943	0.000	0.000	0.057
CA22-1	12	core	6.522	1.478	0.839	0.063	0.290	2.616	1.271	0.034	1.745	0.142	0.000	0.398	0.007	1.957	0.000	0.003	0.041
CA22-1	12	rim	6.516	1.484	0.796	0.076	0.352	2.694	1.254	0.030	1.696	0.101	0.000	0.387	0.007	1.889	0.000	0.002	0.109
CA22-1	13	core	6.721	1.279	0.715	0.045	0.285	2.838	1.182	0.022	1.771	0.142	0.000	0.322	0.007	1.928	0.070	0.002	0.000
CA22-1	13	rim	6.572	1.428	0.830	0.063	0.280	2.750	1.163	0.022	1.769	0.123	0.000	0.361	0.012	1.939	0.000	0.003	0.058
CA22-1	14	core	6.557	1.443	0.784	0.065	0.310	2.793	1.197	0.025	1.732	0.093	0.000	0.380	0.013	1.917	0.000	0.000	0.083
CA22-1	14	rim	6.616	1.384	0.760	0.065	0.281	2.808	1.184	0.028	1.756	0.117	0.000	0.373	0.008	1.889	0.060	0.000	0.051
CA22-1	15	core	6.763	1.237	0.694	0.053	0.262	2.905	1.159	0.024	1.795	0.108	0.000	0.284	0.002	1.956	0.041	0.000	0.004
CA22-1	15	rim	6.611	1.389	0.700	0.122	0.289	2.785	1.127	0.023	1.847	0.107	0.000	0.364	0.008	1.836	0.051	0.004	0.109

References

Abrajevitch, A. (2020). Diagenetic formation of bedded chert: Implications from a rock magnetic study of siliceous precursor sediments. Earth and Planetary Science Letters, 553. 116039. https://doi.org/10.1016/j.epsl.2019.116039

Agard, P., Yamato, P., Jolivet, L., Burov, E. (2009). Exhumation of oceanic blueschists and eclogites in subduction zones: Timing and mechanisms. *Earth-Science Reviews*, 92. 53-79.

Agard, P., Plunder, A., Angiboust, A., Bonnet, G., and Ruh, J. (2018). The subduction plate interface: rock record and mechanical coupling (from long to short timescales). *Lithos*, 320-321. 537-566.

Ague, J.J. and Eckert Jr., J. O. (2012). Precipitation of rutile and ilmenite needles in garnet: Implications for extreme metamorphic conditions in the Acadian Orogen, U.S.A. *American Mineralogist*, 97. 840-855.

Allmendinger, R.W., Cardozo, N., and Fisher, D. (2012). *Structural Geology Algorithms: Vectors and Tensors*. Cambridge University Press.

Allmendinger, R.W., Siron, C.R., and Scott, C.P. (2017). Structural data collection with mobile devices: Accuracy, redundancy, and best practices. *Journal of Structural Geology*, 102. 98-112.

Alvaro, M., Mazzucchelli, M.L., Angel., R.J., Murri, M., Campomenosi, N., Scambelluri, M., Nestola, F., Korsakov, A., Tomilenko, A.A., Marone, F., and Morana, M. (2020). Fossil subduction recorded by quartz from the coesite stability field. *Geology*, 48 (1). 24-28. https://doi.org/10.1130/G46617.1

Angel, R.J., Mazzucchelli, M.L., Alvaro, M., Nimis, P., and Nestola, F. (2014). Geobarometry from host-inclusion systems: The role of elastic relaxation. American Mineralogist, 99. 2146-2149. DOI: http://dx.doi.org/10.2138/am-2014-5047

Angel, R.J., Alvaro, M., Miletich, R., and Nestola, F. (2017a). A simple and generalized P-T-V EoS for continuous phase transitions, implemented in EosFit and applied to quartz. *Contributions to Mineralogy and Petrology*, 172 (5). 29.

Angel, R.J., Mazzucchelli, M.L., Alvaro, M., and Nestola, F. (2017b). EosFit-Pinc: A simple GUI for host-inclusion elastic thermobarometry. *American Mineralogist*, 102 (9). 1957-1960.

Angel, R.J., Murri, M., Mihailova, B., and Alvaro, M. (2019). Stress, strain and Raman shifts. *Zeitschrift für Kristallographie*, 234 (2). 129-140.

Angel, R.J., Gilio, M., Mazzucchelli, M., and Alvaro, M. (2022). Garnet EoS: a critical review and synthesis. *Contributions to Mineralogy and Petrology*, 177. 54.

Angiboust, S., Agard, P., Raimbourg, H., Yamato, P., and Huet, B. (2011). Subduction interface processes recorded by eclogite-facies shear zones (Monviso, W. Alps). *Lithos*, 127. 222-238.

Angiboust, S., Glodny, J., Oncken, O., and Choping, C. (2014). In search of transient subduction interfaces in the Dent Blanche-Sesia Tectonic System (W. Alps). *Lithos*, 205. 298-321.

Angiboust, S., Agard, P., Glodny, J., Omrani, J., and Oncken, O. (2016). Zagros blueschists: Episodic underplating and long-lived cooling of a subduction zone. *Earth and Planetary Science Letters*, 443. 48-58.

Angiboust, S., Cambeses, A., Hyppolito, T., Glodny, J., Monié, P., Calderón, M., and Juliani, C. (2018). A 100 m.y.-long window onto mass-flow processes in the Patagonian Mesozoic subduction zone (Diego de Almagro Island, Chile). *GSA Bulletin*, 130 (9-10). 1439-1456.

Anczkiewicz, R., Platt, J.P., Thirlwall, M.F., and Wakabayashi, J. (2004). Franciscan subduction off to a slow start: evidence from high-precision Lu-Hf garnet ages on high grade-blocks. *Earth and Planetary Science Letters*, 225. 147-161.

Armstrong, J.T. (1988). Quantitative analysis of silicate and oxide minerals: Comparison of Monte Carlo, ZAF and phi-rho-z procedures. In D.E. Newbury (ed.), *Microbeam Analysis*, San Francisco Press. 239-246.

Atwater, T.M. (1998). Plate tectonic history of southern California with emphasis on the Western Transverse Ranges and Northern Channel Islands, in *Contributions to the geology of the Northern Channel Islands, Southern California*. Weigand, P.W., ed. American Association of Petroleum Geologists, Pacific Section, MP 45, p. 1-8.

Barnes, P.M., Wallace, L.M., et al. (2020). Slow slip source characterized by lithological and geometric heterogeneity. *Science Advances*, 6 (13). DOI: 10.1126/sciadv.aay3314

Beall, A., Fagereng, Å., and Ellis, S. (2019). Strength of strained two-phase mixtures: Application to rapid creep and stress amplification in subduction zone mélange. *Geophysical Research Letters*, 46 (1). 169-178. https://doi.org/10.1029/2018GL081252

Bebout, G.E., Ryan, J.G., Leeman, W.P., and Bebout, A.E. (1999). Fractionation of trace elements by subduction-zone metamorphism – effect of convergent-margin thermal evolution. *Earth and Planetary Science Letters*, 171. 63-81.

Bebout, G.E. and Barton, M.D. (2002). Tectonic and metasomatic mixing in a high-*T*, subduction-zone mélange – insights into the geochemical evolution of the slab-mantle interface. *Chemical Geology*, 187. 79-106.

Bebout, G.E. and Penniston-Dorland, S.C. (2016). Fluid and mass transfer at subduction interfaces – The field metamorphic record. *Lithos*, 240-243. 228-258.

Behr, W.M., Kotowski, A.J., and Ashley, K.T. (2018). Dehydration-induced rheological heterogeneity and the deep tremor source in warm subduction zones. *Geology*, 46 (5). 475-478. https://doi.org/10.1130/G40105.1

Bilek, S.L. (2010). Invited review paper: Seismicity along the South American subduction zone: Review of large earthquakes, tsunamis, and subduction zone complexity. *Tectonophysics*, 495. 2-14.

Bonazzi, M., Tumiati, S., Thomas, J.B., Angel, R.J., and Alvaro, M. (2019). Assessment of the reliability of elastic geobarometry with quartz inclusions. Lithos, 350-351. 105201.

Bürgmann, R. (2018). The geophysics, geology and mechanics of slow fault slip. *Earth and Planetary Science Letters*, 495. 112-134.

Calvert, A.J. (2004). Seismic reflection imaging of two megathrust shear zones in the northern Cascadia subduction zone. *Nature*, 428 (6979). 163-167. https://doi.org/10.1038/natur e02372

Campomenosi, N., Mazzucchelli, M.L., Mihailova, B., Scambelluri, M., Angel, R.J., Nestola, F., Reali, A., and Alvaro, M. (2018). How geometry and anisotropy affect residual strain in host-inclusion systems: Coupling experimental and numerical approaches. *American Mineralogist*, 103. 2032-2035.

Cardozo, N. and Allmendinger, R.W. (2013). Spherical projections with OSXStereonet. *Computers & Geosciences*, 51. 193-205. doi:10.1016/j.cageo.2012.07.021.

Chaussard, E. and Amelung, F. (2014). Regional controls on magma ascent and storage in volcanic arcs. *Geochemistry, Geophysics, Geosystems*, 15. 1407-1418.

Cherniak, D.J., Manchester, J., and Watson, E.B. (2007). Zr and Hf diffusion in rutile. *Earth and Planetary Science Letters*, 261. 267-279.

Cisneros, M., Behr, W.M., Platt, J.P., and Anczkiewicz, R. (2022). Quartz-in-garnet barometry constraints on formation pressures of eclogites from the Franciscan Complex, California. *Contributions to Mineralogy and Petrology*, 117 (12).

Clift, P. and Vannucchi, P. (2004). Controls on tectonic accretion versus erosion in subduction zones: Implications for the origin and recycling of the continental crust. *Review of Geophysics*, 42.

Cloos, M. (1982). Flow melanges: Numerical modeling and geologic constraints on their origin in the Franciscan subduction complex, California. *Geological Society of America Bulletin*, 93. 330-345.

Condit, C.B., Guevara, V.E., Delph, J.R., and French, M.E. (2020). Slab dehydration in warm subduction zones at depths of episodic slip and tremor. *Earth and Planetary Science Letters*, 552. 116601. https://doi.org/10.1016/j.epsl.2020.116601

Condit, C.B. and French, M.E. (2022). Geologic evidence of lithostatic pore fluid pressures at the base of the subduction seismogenic zone. *Geophysical Research Letters*, 49. e2022GL098862. https://doi.org/10.1029/2022GL098862

Corvò, S., Maino, M., Piazolo, S., Seno, S., and Langone, A. (2022). Role of inherited compositional and structural heterogeneity in shear zone development at mid-low levels of the continental crust (the Anzola shear zone; Ivrea-Verbano Zone, Southern Alps). *Lithos*, 422-423. 106745. https://doi.org/10.1016/j.lithos.2022.106745

Cruz-Uribe, A.M., Feineman, M.D., Zack, T., and Barth, M. (2014). Metamorphic reaction rates at ~650-800 °C from diffusion of niobium in rutile. *Geochimica et Cosmochimica Acta*, 130. 63-77.

Dohmen, R., Marschall, H.R., Ludwig, T., and Polednia, J. (2019). Diffusion of Zr, Hf, Nb and Ta in rutile: effects of temperature, oxygen fugacity, and doping level, and relation to rutile point defect chemistry. *Physics and Chemistry of Minerals*, 46. 311-332.

Dong, J. and Wei, C. (2021). Multi-stage metamorphism of the South Altyn ultrahigh-pressure metamorphic belt, West China: Insights into tectonic evolution from continental subduction to arc-backarc extension. *Journal of Petrology*, 62 (11). 1-20. https://doi.org/10.1093/petrology/egab082

Dong, J., Grove, M., Wei, C., Han, B-F., Yin, A., Chen, J., Li, A., and Zhang, Z. (2022). Trench retreat recorded by a subduction zone metamorphic history. Geology, 50 (11). 1281-1286. https://doi.org/10.1130/G50385.1

Dragovic, B., Samanta, L.M., Baxter, E.F., and Selverstone, J. (2012). Using garnet to constrain the duration and rate of water-releasing metamorphic reactions during subduction: An example from Sifnos, Greece. *Chemical Geology*, 314-317. 9-22.

Dumitru, T.A., Wakabayashi, J., Wright, J.E., and Wooden, J.L. (2010). Early Cretaceous transition from nonaccretionary behavior to strongly accretionary behavior within the Franciscan subduction complex. *Tectonics*, 29 (5). http://dx.doi.org/10.1029/2009TC002542

Dunkel, K.G., Zhong, X., Arnestad, P.F., Valen, L.V., and Jamtveit, B. (2020). High transient stress in the lower crust: Evidence from dry pseudotachylytes in granulites,

Lofoten Archipelago, northern Norway. *Geology*, 49 (2). 135-139. https://doi.org/10.1130/G48002.1

Ellis, S., Beaumont, C., and Pfiffner, O.A. (1999). Geodynamic models of crustal-scale episodic tectonic accretion and underplating in subduction zones. Journal of Geophysical Research, 104 (B7). 15,169-15,190.

Enami, M., Nishiyama, T., and Mouri, T. (2007). Laser Raman microspectrometry of metamorphic quartz: A simple method for comparison of metamorphic pressures. *American Mineralogist*, 92 (8-9). 1303-1315.

Ernst, W.G. and Liu, J. (1998). Experimental phase-equilibrium study of Al- and Ti-contents of calcic amphibole in MORB – A semiquantitative thermobarometer. *American Mineralogist*, 83. 952-969.

Fagereng, Å. And Sibson, R.H. (2010). Mélange rheology and seismic cycle. *Geology*, 38 (8). 751-754. https://doi.org/10.1130/G30868.1

Federico, L., Crispini, L., Scambelluri, M., Capponi, G. (2007). Ophiolite mélange zone records exhumation in a fossil subduction channel. *Geology*, 35 (6). 499-502.

Ferry, J.M. and Watson, E.B. (2007). New thermodynamic models and revised calibrations for the Ti-in-zircon and Zr-in-rutile thermometers. *Contributions to Mineralogy and Petrology*, 154. 429-437.

Franz, G. and Liebscher, A. (2004). Physical and chemical properties of the epidote minerals: An introduction. *Reviews in Mineralogy and Geochemistry*, 56. 1-82.

French, M.E. and Condit, C.B. (2019). Slip partitioning along an idealized subduction plate boundary at deep slow slip conditions. Earth and Planetary Science Letters, 528. 115828. https://doi.org/10.1016/j.epsl.2019.115828

Gerya, T.V., Stöckhert, B., and Perchuk, A.L. (2002). Exhumation of high-pressure metamorphic rocks in a subduction channel: A numerical simulation. *Tectonics*, 21 (6). 1056.

Gilbert, M.C., Helz, R.T., Popp, R.K., and Spear, F.S. (1982). Experimental studies of amphibole stability. *Reviews in Mineralogy and Geochemistry*, 9B. 229-353.

Gilio, M., Scambelluri, M., Angel, R.J., and Alvaro, M. (2022). The contribution of elastic geothermobarometry to the debate on HP versus UHP metamorphism. *Journal of Metamorphic Geology*, 40. 229-242. DOI: 10.1111/jmg.12625

Godet, A., Raimondo, T., and Guilmette, C. (2022). Atoll garnet: insights from LA-ICP-MS trace element mapping. *Contributions to Mineralogy and Petrology*, 177. 57.

Gonzalez, J.P., Thomas, J.B., Baldwin, S.L., and Alvaro, M. (2019). Quartz-in-garnet and Ti-in-quartz thermobarometry: Methodology and first application to a quartzofeldspathic gneiss from eastern Papua New Guinea. *Journal of Metamorphic Geology*, 37. 1193-1208. DOI: 10.1111/jmg.12508

Grabiec, J.G. (2017). Insights into the formation of the Cottonwood Canyon fault in the Catalina Schist. Unpublished bachelor thesis, University of Maryland. https://www.geol.umd.edu/undergraduate/paper/grabiec.pdf

Grove, M. and Bebout, G.E. (1995). Cretaceous tectonic evolution of coastal southern California: Insights from the Catalina Schist. *Tectonics,* 14 (5). 1290-1308.

Grove, M., Bebout, G.E., Jacobson, C.E., Barth, A.P., Kimbrough, D.L., King, R.L., Zou, H., Lovera, O.M., Mahoney, B.J., and Gehrels, G.E. (2008). The Catalina Schist: Evidence for middle Cretaceous subduction erosion of southwestern North America. In Draut, A.E., et al. eds., *Formation and Applications of the Sedimentary Record in Arc Collision Zones: GSA Special Paper 436*. 335-361. doi: 10.1130/2008.2436(15)

Grove, T.L., Chatterjee, N., Parman, S.W., Médard, E. (2006). The influence of H2O on mantle wedge melting. *Earth and Planetary Science Letters*, 249. 74-89.

Grüneisen, E. (1926). Zustand des festen Körpers. *Handbuch der Physik*. Julius Springer (Berlin), pp. 1-52.

Guillot, S., Schwartz, S., Reynard, B., Agard, P., and Prigent, C. (2015). Tectonic significance of serpentinites. *Tectonophysics*, 646. 1-19.

Harvey, K.M., Penniston-Dorland, S.C., Kohn, M.J., and Piccoli, P.M. (2021a). Assessing *P-T* variability in mélange blocks from the Catalina Schist: Is there differential movement at the subduction interface? *Journal of Metamorphic Geology*, 39 (3). 271-295. https://doi.org/10.1111/jmg.12571

Harvey, K.M., Walker, S., Starr, P.G., Penniston-Dorland, S.C., Kohn, M.J., and Baxter, E.F. (2021b). A mélange of subduction ages: Constraints on the timescale of shear zone development and underplating at the subduction interface, Catalina Schist (CA, USA). *Geochemistry, Geophysics, Geosystems*, 22 (9). e2021GC009790. https://doi.org/10.1029/2021GC009790

Hoover, W.F., Penniston-Dorland, S., Baumgartner, L., Bouvier, A-S., Dragovic, B., Locatelli, M., Angiboust, S., and Agard, P. (2022a). Episodic fluid flow in an eclogite-facies shear zone: Insights from Li isotope zoning in garnet. Geology, 50 (6). 746-750.

Hoover, W.F., Condit, C.B., Lindquist, P.C., Moser, A.C., and Guevara, V.E. (2022b). Episodic slow slip hosted by talc-bearing metasomatic rocks: High strain rates and stress

amplification in a chemically reacting shear zone. Geophysical Research Letters, 49. e2022GL101083. https://doi.org/10.1029/2022GL101083

Jacobson, C.E., Grove, M., Pedrick, J.N., Barth, A.P., Marsaglia, K.M., Gehrels, G.E., and Nourse, J.A. (2011). Late Cretaceous-early Cenozoic tectonic evolution of the southern California margin inferred from provenance of trench and forearc sediments. *Geological Society of America Bulletin*, 123 (3/4). 485-506.

John, T., Gussone, N., Podladchikov, Y.Y., Bebout, G.E., Dohmen, R., Halama, R., Klemd, R., Magna, T., and Seitz, H-M. (2012). Volcanic arcs fed by rapid pulsed fluid flow through subducting slabs. *Nature Geoscience*, 5. 489-492.

Kamb, W.B. (1959). Ice petrofabric observations from Blue Glacier, Washington in relation to theory and experiment. *Journal of Geophysical Research*, 64. 1891-1909.

Kirkpatrick, J.D., Edwards, J.H., Verdecchia, A., Kluesner, J.W., Harrington, R.M., and Silver, E.A. (2020). Subduction megathrust heterogeneity characterized from 3D seismic data. *Nature Geoscience*, 13. 369-374.

Kistler, R.W., Wooden, J.L., and Morton, D.M. (2003). Isotopes and Ages in the Northern Peninsular Ranges Batholith, Southern California. U.S. Geological Survey Open-File Report 03–489. 45 p.

Kohn, M.J. (2014). "Thermoba-Raman-try": Calibration of spectroscopic barometers and thermometers for mineral inclusions. *Earth and Planetary Science Letters*, 388. 187-196.

Kohn, M.J. (2020). A refined zirconium-in-rutile thermometer. *American Mineralogist*, 105. 963-971.

Korsakov, A.V., Kohn, M.J., and Perraki, M. (2020). Applications of Raman Spectroscopy in Metamorphic Petrology and Tectonics. *Elements*, 16. 105-110.

Kotowski, A.J. and Behr, W.M. (2019). Length scales and types of heterogeneities along the deep subduction interface: Insights from exhumed rocks on Syros Island, Greece. *Geosphere*, 15 (4). 1038-1065.

Krebs, M., Schertl, H.-P., Maresch, W.V., and Draper, G. (2011). Mass flow in serpentinite-hosted subduction channels: P-T-t path patterns of metamorphic blocks in the Rio San Juan mélange (Dominican Republic). *Journal of Asian Earth Sciences*, 42. 569-595.

Lakshtanov, D.L., Sinogeikin, S.V., and Bass, J.D. (2007). High-temperature phase transitions and elasticity of silica polymorphs. *Physics and Chemistry of Minerals*, 34 (1). 11-22. doi:10.1007/s00269-006-0113-y

Liao, Y., Wei, C., and Rehman, H.U. (2021). Titanium in calcium amphibole: Behavior and thermometry. *American Mineralogist*, 106. 180-191. https://doi.org/10.2138/am-2020-7409

Lucassen, F., Dulski, P., Abart, R., Franz, G., Rhede, D., Romer, R.L. (2010). Redistribution of HFSE elements during rutile replacement by titanite. *Contributions to Mineralogy and Petrology*, 160. 279-295. http://dx.doi.org/10.1007/s00410-009-0477-3

Ludwig, K.R. (2012). *User's Manual for Isoplot 3.75. A Geochronological Toolkit for Microsoft Excel*. Berkely Geochronology Center Special Publication, 5. 75 p.

Malatesta, C., Crispini, L., Federico, L., Capponi, G., and Scambelluri, M. (2012). The exhumation of high pressure ophiolites (Voltri Massif, Western Alps): Insights from structural and petrologic data on metagabbro bodies. *Tectonophysics*, 568-569. 102-103.

Massonne, H-J. and Li, B. (2022). Eclogite with unusual atoll garnet from the southern Armorican Massif, France: Pressure-temperature path and geodynamic implications. *Tectonophysics*, 823. 229183. https://doi.org/10.1016/j.tecto.2021.229183

Mattinson, J.M. (1986). Geochronology of high-pressure-low-temperature Franciscan metabasites: A new approach using the U-Pb system. *Geological Society of America Memoir 164*. 95-105.

Mazzucchelli, M.L., Burnley, P., Angel, R.J., Morganti, S., Domeneghetti, M.C., Nestola, F., Alvaro, M. (2018). Elastic geothermobarometry: Corrections for the geometry of the host-inclusion system. *Geology*, 46 (3). 231-234.

Mazzucchelli, M.L., Angel, R.J, and Alvaro, M. (2021). EntraPT: An online platform for elastic geothermobarometry. American Mineralogist, 106. 830-837. DOI: https://doi.org/10.2138/am-2021-7693CCBYNCND

Mulcahy, S.R., Starnes, J.K., Day, H.W., Coble, M.A., Vervoort, J.D. (2018). Early onset of Franciscan subduction. *Tectonics*, 37. 1194-1209.

Mungall, J.E. (2002). Roasting the mantle: Slab melting and the genesis of major Au and Au-rich Cu deposits. *Geology*, 30 (10). 915-918.

Murri, M., Mazzucchelli, M.L., Campomenosi, N., Korsakov, A.V., Prencipe, M., Mihailova, B.D., Scambelluri, M., Angel, R.J., and Alvaro, M. (2018). Raman elastic geobarometry for anisotropic mineral inclusions. *American Mineralogist*, 103 (11). 1869-1872.

Neuville, D.R., de Ligny, D., and Henderson, G.S. (2014). Advances in Raman Spectroscopy Applied to Earth and Material Sciences. *Reviews in Mineralogy and Geochemistry*, 78. 509-541.

O'Haver, T. (2023). ipf(arg1,arg2,arg3,arg4). (https://www.mathworks.com/matlabcentral/fileexchange/23452-ipf-arg1-arg2-arg3-arg4), MATLAB Central File Exchange. Retrieved January 17, 2023.

Pasteris, J.D. and Beyssac, O. (2020). Welcome to Raman Spectroscopy: Successes, Challenges, and Pitfalls. *Elements*, 16. 87-92.

Peacock, S.M. (2009). Thermal and metamorphic environment of subduction zone episodic tremor and slip. *Journal of Geophysical Research,* 114.

Penniston-Dorland, S.C., Sorensen, S.S., Ash, R.D., and Khadke, S.V. (2010). Lithium isotopes as a tracer of fluids in a subduction zone mélange: Franciscan Complex, CA. *Earth and Planetary Science Letters*, 292 (1-2). 181-190.

Penniston-Dorland, S.C., Gorman, J.K., Bebout, P.M., Piccoli, P.M., and Walker, R.J. (2014). Reaction rind formation in the Catalina Schist: Deciphering a history of mechanical mixing and metasomatic alteration. *Chemical Geology*, 384. 47-61.

Penniston-Dorland, S.C., Kohn, M.J., and Manning, C.E. (2015). The global range of subduction zone thermal structures from exhumed blueschists and eclogites: Rocks are hotter than models. *Earth and Planetary Science Letters*, 428. 243-254.

Penniston-Dorland, S.C., Kohn, M.J., and Piccoli, P.M. (2018). A mélange of subduction temperatures: Evidence from Zr-in-rutile thermometry for strengthening of the subduction interface. *Earth and Planetary Science Letters*, 482. 525-535.

Penniston-Dorland, S.C. and Harvey, K.M. (2023). Constraints on tectonic processes in subduction mélange: A review of insights from the Catalina Schist (CA, USA). *Geosystems and Geoenvironment*, in press. https://doi.org/10.1016/j.geogeo.2023.100190

Phillips, N.J., Motohashi, G., Ujiie, K., and Rowe, C.D. (2020). Evidence of localized failure along altered basaltic blocks in tectonic mélange at the updip limit of the seismogenic zone: Implications for the shallow slow earthquake source. *Geochemistry, Geophysics, Geosystems*, 21.

Philpotts, A.R. and Ague, J.J. (2022). *Principles of Igneous and Metamorphic Petrology*, 3rd ed. Cambridge University Press.

Platt, J.P. (1975). Metamorphic and deformational processes in the Franciscan Complex, California: Some insights from the Catalina Schist terrane. *Geological Society of America Bulletin*, 86 (10). 1337-1347.

Platt, J. (1976). *The petrology, structure, and geologic history of the Catalina Schist Terrain, Southern California*. University of California Publications in Geological Sciences, 112. p. 111.

Platt, J.P. (1993). Exhumation of high-pressure rocks: a review of concepts and processes. *Terra Nova*, 5. 119-133.

Raase, P. (1974). Al and Ti contents of hornblende, indicators of hornblende, indicators of pressure and temperature of regional metamorphism. *Contributions to Mineralogy and Petrology*, 45. 231-236.

Raven, M.J. and Dickson, J.A.D. (1989) Fir-tree zoning: An indicator of pulsed crystallization in calcite cement crystals. *Sedimentary Geology*, 65. 249-259.

Rehman, H.U., Iizuka, Y., Lee, H-Y., Chung, S-L., Duan, Z., Wei, C., Khan, T., Zafar, T., and Tamamoto, H. (2019). Zirconium in rutile thermometry of the Himalayan ultrahigh-pressure eclogites and their retrogressed counterparts, Kaghan Valley, Pakistan. *Lithos*, 344-345. 86-99.

Ridolfi, F., Zanetti, A., Renzulli, A., Perugini, D., Holtz, F., and Oberti, R. (2018). AMFORM, a new mass-based model for the calculation of the unit formula of amphiboles from electron microprobe analyses. *American Mineralogist*, 103. 1112-1125. DOI: http://doi.org/10.2138/am-2018-6385

Rogers, G. and Dragert, H. (2003). Episodic tremor and slip on the Cascadia subduction zone: The chatter of silent slip. *Science*, 300. 1942-1943.

Sambridge, M.S. and Compston, W. (1994). Mixture modeling of multi-component data sets with application to ion-probe zircon ages. Earth and Planetary Science Letters, 128 (3-4). 373-390. https://doi.org/10.1016/0012-821X(94)90157 -0

Schmidt, C. and Ziemann, M.A. (2000). In-situ Raman spectroscopy of quartz: A pressure sensor for hydrothermal diamond-anvil cell experiments at elevated temperatures. *American Mineralogist*, 85 (11-12). 1725-1734.

Schumacher, J.C. (2007). Metamorphic amphiboles: Composition and coexistence. Reviews in Mineralogy and Geochemistry, 67. 359-416.

Schwarzenbach, E.M., Zhong, X., Caddick, M.J., Schmalholz, S.M., Menneken, M., Hecht, L., and John, T. (2021). On exhumation velocities of high-pressure units based on insights from chemical zoning in garnet (Tianshan, NW China). *Earth and Planetary Science Letters*, 570. 117065. https://doi.org/10.1016/j.epsl.2021.117065

Seno, T. (2017). Subducted sediment thickness and M_w 9 earthquakes. Journal of Geophysical Research: Solid Earth, 122 (1). 470-491. https://doi.org/10.1002/2016JB013048

Sillitoe, R.H. (2010). Porphyry Copper Systems. *Economic Geology*, 105 (1). 3-41.

Sorensen, S.S. and Barton, M.D. (1987). Metasomatism and partial melting in a subduction complex: Catalina Schist, southern California. *Geology*, 15. 115-118.

Sorensen, S.S. (1988). Petrology of amphibolite-facies mafic and ultramafic rocks from the Catalina Schist, southern California: metasomatism and migmatization in a subduction zone metamorphic setting. *Journal of Metamorphic Geology*, 6. 405-435.

Sorensen, S.S. and Grossman, J.N. (1989). Enrichment of trace elements in garnet amphibolites from a paleo-subduction zone: Catalina Schist, southern California. *Geochimica et Cosmochimica Acta*, 53. 3155-3177.

Spear, F.S. (1993). *Metamorphic Phase Equilibria and Pressure-Temperature-Time Paths*. Mineralogical Society of America Monograph.

Stern, R.J. (2002). Subduction Zones. *Reviews of Geophysics*, 40 (4). 3-1 to 3-13.

Stevenson, D.J. (2003). Styles of mantle convection and their influence on planetary evolution. *Comptes Rendus Geoscience*, 335 (1). 99-111.

Syracuse, E.M., van Keken, P.E., and Abers, G.A. (2010). The global range of subduction zone thermal models. *Physics of the Earth and Planetary Interiors*, 183 (1-2). 73-90.

Szczepański, J., Zhong, X., Dąbrowski, M., Wang, H., and Golén, M. (2022). Combined phase diagram modelling and quartz-in-garnet barometry of HP metapelites from the Kamieniec Metamorphic Belt (NE Bohemian Massif). *Journal of Metamorphic Geology*, 40. 3-37. DOI: 10.1111/jmg.12608

Taetz, S., John, T., Bröcker, M., Spandler, C., and Stracke, A. (2018). Fast intraslab fluid-flow events linked to pulses of high pore fluid pressure at the subducted plate interface. *Earth and Planetary Science Letters*, 482. 33-43.

Tan, H., Gao, X., Wang, K., Gao, J., and He, J. (2022). Hidden roughness of subducting seafloor and implications for megathrust seismogenesis: Example from northern Manila trench. Geophysical Research Letters, 49. https://doi.org/10.1029/2022GL100146

Tewksbury-Christle, C.M., Behr, W.M., and Helper, M.A. (2021). Tracking deep sediment underplating in a fossil subduction margin: Implications for interface rheology and mass and volatile recycling. *Geochemisty, Geophysics, Geosystems*, 22. https://doi.org/10.1029/2020GC009463

Thomas, J.B. and Spear, F.S. (2018). Experimental study of quartz inclusions in garnet at pressures up to 3.0 GPa: Evaluating validity of the quartz-in-garnet inclusion elastic thermobarometer. *Contributions to Mineralogy and Petrology*, 173 (5). 42.

Tilley, H., Moore, G.F., Underwood, M.B., Hernández-Molina, F.J., Yamashita, M., Kodaira, S., and Nakanishi, A. (2021). Heterogeneous sediment input at the Nankai trough subduction zone: Implications for shallow slow earthquake localization. Geochemistry, Geophysics, Geosystems, 22 (10). https://doi.org/10.1029/2021GC009965

Tomkins, H.S., Powell, R., and Ellis, D.J. (2007). The pressure dependence of the zirconium-in-rutile thermometer. *Journal of Metamorphic Geology*, 25 (6). 703-713.

Tual, L., Möller, C., and Whitehouse, M.J. (2018). Tracking the prograde P-T path of Precambrian eclogite using Ti-in-quartz and Zr-in-rutile geothermobarometry. Contributions to Mineralogy and Petrology, 173 (56). https://doi.org/10.1007/s00410-018-1482-1

Ukar, E. (2012). Tectonic significance of low-temperature blueschist blocks in the Franciscan mélange at San Simeon, California. *Tectonophysics*, 568-569. 154-169.

Vermeesch, P. (2018). IsoplotR: A free and open toolbox for geochronology. *Geoscience Frontiers*, 9. 1479-1493. doi: 10.1016/j.gsf.2018.04.001

Whitney, D.L. and Evans, B.W. (2010). Abbreviations for names of rock-forming minerals. *American Mineralogist*, 95. 185-187.

Wolfe, O.M., Spear, F.S., and Harrison, T.M. (2021). Pronounced and rapid exhumation of the Connecticut Valley Trough revealed through quartz in garnet Raman barometry and diffusion modelling of garnet dissolution-reprecipitation reactions. *Journal of Metamorphic Geology,* 39. 1045-1069. DOI: 10.1111/jmg.12601

Zack, T., Moraes, R., and Kronz, A. (2004). Temperature dependence of Zr in rutile: empirical calibration of a rutile thermometer. *Contributions to Mineralogy and Petrology*, 148. 471-488.

Zack, T. and Kooijman, E. (2017). Petrology and Geochronology of Rutile. *Reviews in Mineralogy and Geochemistry*, 83. 443-467.

Zhong, X., Moulas, E., and Tajčmanová, L. (2020). Post-entrapment modification of residual inclusion pressure and its implications for Raman elastic thermobarometry. *Solid Earth*, 11. 223-240. https://doi.org/10.5194/se-11-223-2020

Zhou, H., Müller, A., Augland, L.E., Kristoffersen, M., and Erambert, M. (2022). Titanite links rare-element (meta-)pegmatite mineralization to Caledonian metamorphism. *Geochimica et Cosmochimica Acta*, 332. 285-306.